THESIS

MODELING OF OPTICAL WAVGUIDES WITH POROUS SILICA CLADDINGS AND THEIR USE IN LEAC SENSORS

Submitted by

Yusra Mahmoud Obeidat

Department of Electrical and Computer Engineering

In partial fulfillment of the requirements

For the Degree of Master of Science

Colorado State University

Fort Collins, Colorado

Fall 2014

Master's Committee:

Advisor: Kevin L. Lear

Sudeep Pasricha
Olivier Pinaud

Copyright by Yusra M.Obeidat 2014

All Rights Reserved

ABSTRACT

MODELING OF OPTICAL WAVGUIDES WITH POROUS SILICA CLADDINGS AND THEIR USE IN LEAC SENSORS

Integrated optical biosensors have many advantages such as low-cost, portability and the ability to detect multiple analytes on a single waveguide. They can be used in many important applications including biosensing applications.

Previous research work focused on the issues of design, modeling and measurement of the local evanescent array coupled (LEAC) biosensor. The sensors were made using conventional dielectrics such as SiO_2 and SiN_x.

The large increase in the complexity of the integrated circuits has increased the need for developing low-k dielectrics as new materials to cope with the integration challenges and improve operating speed. Furthermore, optical interconnects are required to be used to replace electrical interconnects in ICs to meet future goals. This increases the need for simultaneous manufacturing of electronics and optics on the same chip using a CMOS process.

The research conducted during my Master of Science studies has addressed two important goals. The first was to use models to calculate surface and volume scattering losses in optical waveguides, especially, ones with porous silica claddings. The second goal was to use the simulation results to demonstrate the possibility of using porous silica in designing optical waveguides and LEAC sensors.

By applying these models to porous silica optical waveguides described in previous publications, the agreement between their experimental results and the models results have been

proved. Thus, these models can be used in the future to calculate the scattering losses in optical waveguides including ones with porous silica cladding.

The main methods that are used to prepare porous silica and the models that are used to determine the effective index of porous silica have been discussed. A Matlab modesolver was used to simulate porous silica waveguides. Predictions for sensor sensitivity and waveguide loss as a function of waveguide dimension have been made using modesolver simulation results. The results demonstrate the ability to use porous silica in LEAC sensors in the future.

ACKNOWLEDGEMENTS

First and above all, I praise God, the almighty for providing me this opportunity and granting me the capability to proceed successfully.

I would like to express my special deep gratitude to Professor Kevin Lear, my research supervisor, for his patient guidance, enthusiastic encouragement and useful critiques of this research work.

I would like to thank my group members for their support by providing either valuable suggestions or technical assistance. My grateful thanks are also extended to my friends and colleagues at Colorado State University for their support.

Also, I would like to extend my thanks and appreciation to doctor Phil Marsh for his help to make my thesis better by his important and smart comments.

I would like to extend my thanks to my cousin Marwan and his wife Jamie for their help and encouragement through my study. Thanks to Dania and all my close friends, I greatly appreciate your spiritual supports. I will never forget the nice time that we spent together.

I also would like to express my appreciation to my sponsor who gave me the financial support to get the chance to pursue my MS at Colorado State University.

Finally, I can't finish without thanking my great family. I warmly thank and appreciate my parents for their prayers, material and spiritual support in all aspects of my life. I would like to thank all of my brothers, sisters, in-laws, nieces and nephews for their prayers, support and encouragement through my study. Thanks for having you all in my life.

TABLE OF CONTENTS

ABSTRACT....ii

ACKNOWLEDGEMENTS....iv

TABLE OF CONTENTS....v

Chapter 1 Introduction....1

1.1 Introduction....1

1.2 LEAC chip description....3

1.3 Motivation....6

1.4 Overview....7

References....9

Chapter 2 Background and present progress of optical waveguides....10

2.1 Optical waveguides structures....10

2.2 Optics principles of optical waveguides....11

2.2.1 Frensel's Equations....11

2.3 Optical waveguides modes....14

2.4 Optical waveguide losses....19

2.4.1 Loss coefficient in optical waveguides related to the complex refractive index....19

2.4.2 The main sources of loss in optical waveguides....20

2.4.3 Loss measurement in optical waveguides....22

2.4.4 Loss calculations in optical waveguides....25

2.4.5 Modal loss....27

2.5 Fabrication process....30

2.5.1 Cleaning 30

2.5.2 Pre-bake 30

2.5.3 Spin-coat 30

2.5.4 Soft bake 31

2.5.5 Alignment and exposure 31

2.5.6 Etching..33

2.5.7 Metallization..33

2.5.8 Lift-off..34

2.6 Review of previous work on LEAC sensors..34

2.7 Low-k dielectrics 41

2.7.1 What is low-k dielectric?..42

2.7.2 Why do we need low-k dielectrics for electrical interconnects?...46

2. 7.3 Why do we need low-k dielectrics in optical interconnects?...47

2.7.4 Preparation methods of porous silica..49

2.7.5 Effective medium models for the refractive index of porous material................................52

2.8 Optical waveguide modeling..53

2.8.1 Full-Vector Finite Difference Modesolver..53

References..55

Chapter 3: Modeling of scattering loss in optical waveguides...61

3.1 Scattering loss caused by pores (volume scattering) in porous silica....................................61

3.1.1 Examples of volume scattering loss calculations..65

3.2 Surface scattering loss model for optical waveguides..67

3.2.1 Examples of surface scattering loss calculations..70

References....73

Chapter 4: Modeling of LEAC sensor without low-k dielectrics....74

4.1 Photodetector coupling loss results....74

4.2 Modal solutions results....76

4.3 Comparisons of modeling results to Erickson's modeling results for LEAC sensors....77

4.5 Comparison between the results of sensitivities as a function of lower cladding, and core thicknesses....78

4.6 Scattering loss results....82

References....84

Chapter 5: Modeling of optical waveguides with porous silica claddings....85

5.1 Introduction....85

5.2 Optical waveguides using low-k dielectrics porous silica....86

5.2.1 Optical waveguides design using porous silica as lower cladding....88

References....98

Chapter 6: LEAC sensor design using porous silica as lower-cladding....101

6.1 Introduction....101

6.2 Can we use Jain et al.'s waveguide as a LEAC sensor?....102

6.3 Predictions of a LEAC sensor using porous silica....105

6.3.1 The first prediction assuming porosity of 40%....105

6.3.2 The second prediction assuming a porosity of 63%....108

6.3.3 Modal loss....111

6.3.4 Concluding remarks....112

References…..…………………………………………………………………………..117

Chapter 7: Conclusions and Future Work……………………………………….....……..118

7.1 Achievements………………………………………………………………………….118

7.1.1 Theoretical study of LEAC sensors ……………………………………..……………118

7.1.2 Measurement of optical losses in optical waveguide…..…………………………………….119

7.1.3 Preparation methods of porous silica…………….………………………………………119

7.1.4 Optical waveguide loss calculations………………………………..………………119

7.2 Conclusions ………………….……………………………………………………..119

7.3 Future work suggestions…………………………………………………………………120

APPENDICES...122-142

Appendix A: Fabrication Process Flow for porous silica waveguide of porous silica made by electrochemical etching...122-127

References..128

Appendix B: Matlab modesolver code used to solve for the waveguide leaky modes, absorption loss, surface scattering loss, and volume scattering loss..130-142

Chapter 1: Introduction

1.1 Introduction

The local evanescent array coupled "LEAC" sensor is an optoelectronic CMOS-compatible sensor used for sensing applications. Because of its ability to sense multiple pathogens simultaneously, it can be used in many applications such as point of care clinical, food safety, environmental monitoring and biosensing applications [2, 3, and 5].

The LEAC biosensor is a waveguide-based, label free, and non-resonant device with minimal temperature dependence [2, 5]. Furthermore, LEAC technology can utilize LEDs which offer lower cost and simplicity relative to laser diodes.

For the LEAC device to be used as a complete practical biosensor, the detector is divided into sections, each of which is activated by a different type of analyte-binding antibody. Each LEAC section has a detector buried under its lower cladding region to register the presence of its target analyte according to the specific antibody used on the LEAC section [4].

The performance of the device was improved for real-time measurement by adding on-chip reference region of known refractive index. Improvement of the fabrication process and optimization of the waveguide parameters to reduce the optical losses of the waveguide was considered to increase the performance of the device [5, 8].

The main operation principle of the LEAC device is sensing the modification in evanescent fields both above and below the waveguide due to the analyte binding on the upper cladding and measuring the guided optical mode modulation induced by the refractive index change of the waveguide's upper cladding. The local change in the evanescent field which indicates adsorbed species on the upper cladding of the waveguide can be detected by reading the change of the photocurrent of the photodetector array elements [1-5].

The LEAC chip has emerged as a device that can be used as a low-cost biosensor in biomedical applications. The compatibility with CMOS technology provides a low- cost manufacturing and integrated signal processing. Furthermore, the entire area of the multi-analyte LEAC system including the optical source, detectors array, integrated signal process, and telemetry electronics is less than 1 cm^2, which increases device portability and the ability to use it in different applications and different places. This will make the detection of the diseases in developing countries easier and less expensive [2-6].

The focus of my research has been to demonstrate the ability to use low-k dielectrics in designing optical waveguides and optimize the sensing performance of these waveguides to be able to be used in sensing applications.

During my thesis work, I obtained a good understanding of the LEAC chip and the main fabrication process. Matlab mode solver can be used to solve for the waveguide's leaky modes to understand the main parameters that affect the device performance. Also, I have used mathematical models of scattering and absorption losses to study the effect of waveguide parameters on its performance. The reason for using low-k dielectrics is to reduce the refractive index of the lower cladding which will increase the refractive index contrast and then the optical confinement. Thus this increases the ability to use optical waveguides in communication applications.

Finally, one of the most important parts of my research work was to use mathematical models to calculate surface scattering loss and volume scattering loss in optical waveguides, especially, porous silica waveguides.

1.2 LEAC chip description

The Local Evanescent Array Coupled chip is an optical waveguide that is used to transport light by the method of total internal reflection. The main advantages of optical waveguides compared with conventional optical instruments are minimizing the optical devices and the ability to integrate buried photodetectors which increases the portability of the device [5, 6].

In an optical waveguide, an optical material of high refractive index acts as a core surrounded by a material with lower refractive index as a cladding. The light is coupled into the core and propagates by multiple total internal reflections under certain conditions [6].

There are many structures for the optical waveguides, such as slab, ridge, or channel waveguides. In recent works, ridge waveguides are mostly used in many integrated biosensor structures [6].

A silicon wafer is used as a starting substrate to fabricate the LEAC chips. Integrated photodetector arrays are buried by metallization on silicon substrate and then a dielectric optical waveguide is formed between the metal contacts [8]. Most of the research works in optical waveguides used traditional semiconductor materials such as silicon nitride as a core and silicon oxide as a cladding, which ensure low cost and CMOS compatibility [6].In this research work the goal is to use low-k dielectrics in designing LEAC chips to ensure the ability to integrate photonics and electronics on the same chip.

Fig. 1.1 shows a cross section and SEM picture of the LEAC chip structure with buried photodetectors fabricated in a commercial facility [2].

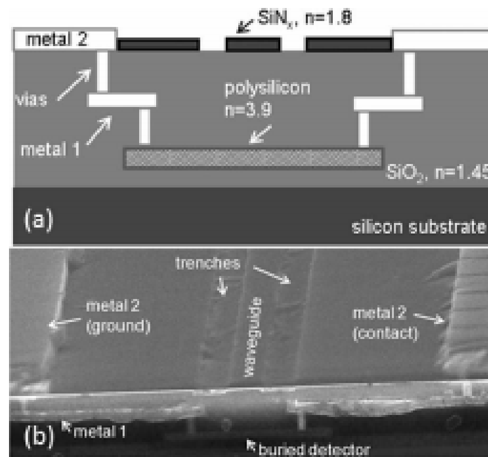

Figure 1.1: Cross section and SEM picture of the LEAC biosensor structure incorporating buried detectors. **Reproduced from [2]**

One of the main parts that are used for LEAC operation is the light source. The most commonly used light sources for waveguides are laser diodes and LEDs. A LED is a good choice for integrated optical system because it is just a simple PN junction diode with low-cost, high efficiency, and small physical volume. However, laser is a special form of LED. It is a P-N junction diode with a thin depletion layer where electrons and holes collide to create light photons, when the diode is forward biased. But, in laser the active part is made quite narrow, to concentrate the carriers. Also, in a laser diode an optical resonator cavity is needed to enable only light with selected frequency to pass the gain material multiple times, which makes the stimulated emission at selected frequency dominate. Lasers have a narrower spectrum and better light coherence than LEDs. However, since LEAC is a non-resonant device, it is enough to use LED as an optical source which lowers the system cost and simplifies the design [6].

The chip operates by detecting the changes in the optical properties that are caused by target binding into the upper cladding. The refractive index change leads to shifting the evanescent field up and away from the buried photodetectors. This will reduce the photodetector coupling

loss. While, the photodetector coupling loss is the amount of power loss from the waveguide propagating mode(s) into the bottom of the lower cladding (which contains the photodetectors).

Therefore, the reduction in photosetector coupling loss results in a decrease in the measured photocurrent in the underlying metal semiconductor metal photodetectors (MSM) [1-6, and 8].

Fig. 1.2 shows a 3-D structure of the LEAC chip with buried photodetector arrays and probes to measure the photocurrent coupled to the detectors. Light is weakly confined due to the nanoscale dimensions of the waveguide core and there is a strong interaction between the guided mode's evanescent tail and the structure's upper cladding [7].

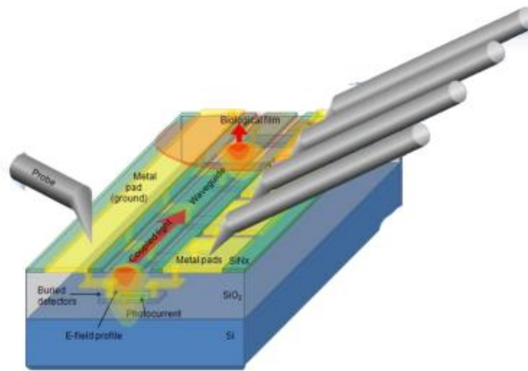

Figure 1.2: 3-D structure of the LEAC chip**. Reproduced from [7]**

LEAC provides multianalyte detection along a single waveguide, thus it can be used to improve the quality of many sensing applications. It is possible to make a low-cost portable biosensor chips with high detection sensitivity based on silicon and CMOS-compatible integrated optical waveguide biosensing technology. These sensors improve the speed and quality of analyte detection and they can be used in different biomedical areas in point-of care diagnosis, because they can make the detection of diseases easier and less expensive [5, 6, 7, 8].

1.3 Motivation

In recent years, the LEAC chip has been used as a lab-on chip diagnostic biosensor. Many research works have been done to employ a novel strategy for detecting different diseases by real time measurements using a portable, high speed, and low-cost label-free technology. This sensor has a high potential for biomedical applications where it provides a great advancement in diagnostic testing. This device helps to improve the quality of people's life, it makes the sensing of diseases faster and easier and then it reduces the threat to patient's lives [2, 5, 6, and 8].

Many research works have been done to improve the performance of the LEAC chip by trying to modify and optimize the parameters that affect its operation. Doing real time measurements with minimum losses using a low-cost, fast, and simple process becomes an important goal of designing LEAC biosensors.

The general purpose of my thesis work is to demonstrate the ability to use dielectrics with low dielectric constant k (permittivity) as lower cladding materials in optical waveguides, and study the ability to use them in LEAC sensors. A low-k dielectric optical waveguide has a high refractive index contrast between the core and the cladding which increases the ability to use them for high density on-chip optical waveguides to replace the current electrical interconnects. Using low-k dielectrics in designing optical waveguides improves the ability to use them as interconnects in communication systems.

Simulations using a mode solver programmed in MATLAB determined the electromagnetic EM field profiles and losses of leaky modes of optical waveguides including ones incorporating low-k dielectrics. Therefore, by modeling a waveguide, we can determine the main parameters that affect its operation and choose the dimensions that improve its sensing performance. Two mathematical models for calculating the scattering losses in optical waveguides have been used

as an important part of this research focus, and I used these models to modify the Matlab modesolver to simulate the surface scattering loss and volume scattering loss in optical waveguides.

1.4 Overview

The overall objective of this research work is to use mathematical models to calculate the scattering losses in optical waveguides, and to study the possibility of using low-k dielectrics in designing optical waveguides and LEAC sensors.

Chapter 2 details the background information about the structures, the main optics principles, and the main fabrication process steps of the LEAC chip. It includes a review of previous work in low loss LEAC sensors. It covers the main losses in optical waveguides and the methods that are used to measure the losses, and it explains a mathematical model of sidewall scattering loss. Furthermore, it goes through the main reasons for using low-k dielectrics in optical and electrical interconnects. Also, it includes the main methods that are used to prepare porous silica, and the models that are used to define the effective index of porous silica.

Chapter 3 discusses a scattering loss modeling in optical waveguides. It describes the model that can be used to calculate the volume scattering in porous silica. Different examples of volume scattering loss calculations have been included. Also, it describes the model that can be used to calculate surface scattering loss for optical waveguides. Different examples of surface scattering loss calculations have been included.

Chapter 4 includes simulation results of the LEAC sensors made by Erickson et al. [8]. Simulation results using Matlab modesolver are included. Table of comparison between the results is included.

Chapter 5 discusses the design of optical waveguides using porous silica. Matlab modesolver has been used to simulate porous silica waveguides made by different authors, and a comparison between the experimental and simulation results has been made.

Chapter 6 discusses the possibility to use porous silica in designing good LEAC sensors. We used the simulation to decide the ability to use porous silica waveguides as LEAC sensors by comparing these results to LEAC sensors made by other authors using normal dielectrics. In addition, the chapter includes predictions for the dimensions of porous silica waveguides that can be used in future to design porous silica LEAC sensors.

Conclusions and suggestions for future work are given in Chapter 7.

References

[1] Robert Pownall, Guangwei Yuan, Tom W. Chen, Phil Nikkel, and Kevin L. Lear, "Geometry Dependence of CMOS-Compatible, Polysilicon, Leaky-Mode Photodetectors, IEEE Photonics Technology Letters, APRIL 1, 2007.

[2] Rongjin Yan, Santano P. Mestas, Guangwei Yuan, Rashid Safaisini, and Kevin L. Lear, " Response of Local Evanescent Array-Coupled Biosensors to Organic Nanofilms", IEEE Journal of selected topics in quantum electronics , September/October 2009.

[3] G. Yuan, M.D. Stephens, D.S. Dandy, J.K. Gerding,A, Van Orden and K.L. Lear, “Local evanescent, array coupled (LEAC) biosensor response to low index adlayers", 2006 Optical Society of America.

[4] Guangwei Yuan, Matt Stephens, David S. Dandy, Ahmad N. AL-Omari , and Kevin L. Lear, "Implementation of buried detector arrays for waveguide sensors', 0-7803-9556-5/06/$20.00 © 2006 IEEE.

[5] Tim A. Erickson, , and Kevin L. Lear, "Optimization of the Local Evanescent Array-Coupled Optoelectronic Sensing Chip for Enhanced, Portable, Real-Time Sensing", IEEE Sensors Journal, MAY 2013.

[6] Rongjin Yan, "A CMOS compatible optical biosensing system based on local evanescent field shift mechanism", Ph.D. dissertation Dept. Electrical and Computer. Eng. , Colorado State University Fort Collins, Colorado Fall 2011.

[7] Andrew Armstrong ,John Blatt,Justin Grantham ,Dan Higley ,Kelli Luginbuhl ,Kelly Nienburg , " Lab-on-a-Chip Diagnostic Biosensor", ECE402 report, Dept. Electrical and Computer. Eng., Colorado State University Fort Collins, Colorado Spring Semester 2011.

[8] Timothy Erickson, “Design optimization and fabrication of an integrated optoelectronic sensing chip for applications in real-time biosensing and groundwater contaminant detection", Ph.D. dissertation, Dept. Electrical and Computer. Eng., Colorado State University Fort Collins, Colorado Summer 2014.

Chapter 2: Background and present progress of optical waveguides

2.1 Optical waveguides structures

A typical waveguide structure consists of a high refractive index dielectric material called the core, and a low-refractive index dielectric material called the cladding. Light coupled into the core will be trapped in the high index channel and propagate through multiple total internal reflections under certain conditions. The material types and thicknesses in a conventional waveguide are selected to confine more light inside the optical waveguide with less coupling losses [10, 11, and 12].

There are two basic types of optical waveguides; cylindrical and planar (slab) waveguides. A cylindrical waveguide such as the optical fiber has a two dimensional transverse optical confinement where the core is surrounded by the cladding in all directions and the index of refraction n(x, y) is a function of both x and y coordinates. However, a planar(slab) waveguide has an optical confinement in only one transverse direction, where the core is sandwiched between cladding layers in only one direction and the index profile n(x) is a function of only one direction, say x [10, 12] . **Fig. 2.1** shows an example of both cylindrical and slab waveguides.

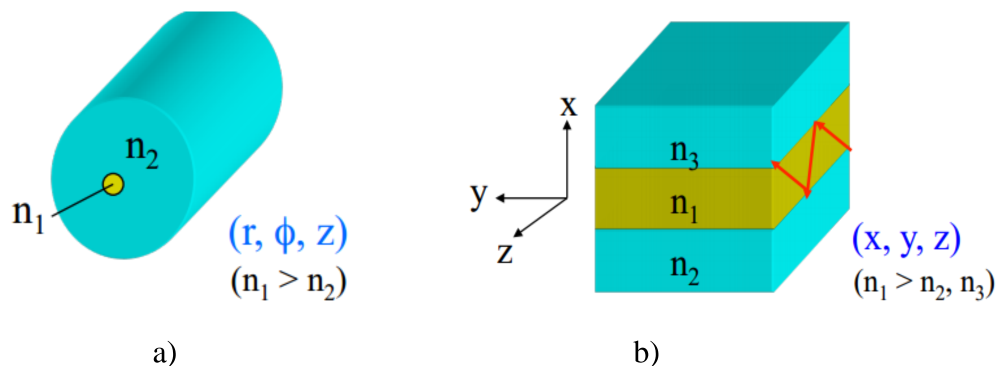

Figure 2.1: a) cylindrical optical fiber. b) Planar (slab) waveguide. **Reproduced from [12]**

Furthermore, one of the important properties of an optical waveguide is the index profile. The waveguide is called step index waveguide if the index profile has an abrupt change between the core and cladding, while it is called graded index waveguide if the index varies gradually [12]. **Fig. 2.2** shows the difference between the two index profiles.

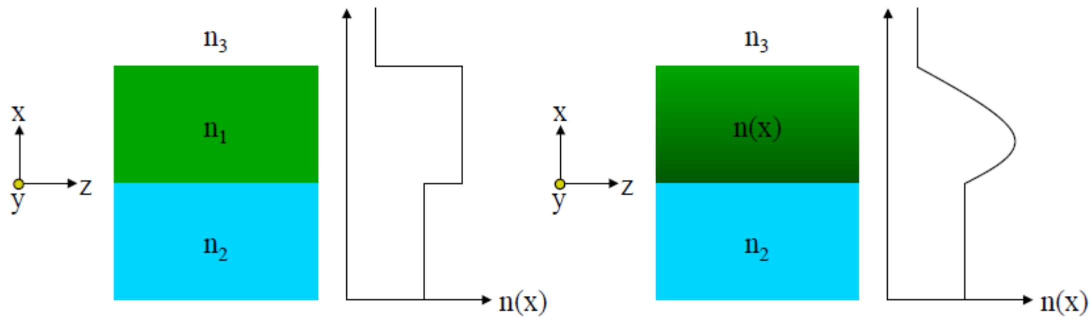

Figure 2.2: On the left hand side is a step index profile, while on the right hand side is a graded index profile. **Reproduced from [12]**

2.2 Optics principles of optical waveguides

Optical waveguides have been studied for many years and they have applications in many areas. They are useful in microwave and optical frequency ranges, but they can be constructed to carry waves over a wide portion of the electromagnetic spectrum [6, 11].

The light can be confined inside a waveguide by multiple total internal reflections. There are a number of specified modes with different phases at a given frequency for the power propagated in a waveguide [6, 10, 11, and 12].

2.2.1 Fresnel's equations

To understand optical waveguides, several terms related to the ray of light need to be clarified. An incident ray is a ray of light that strikes a surface with an angle between this ray and normal to the surface, is called the angle of incidence. The reflected ray is the ray that represents the light reflected by the surface. The angle between the surface normal and the reflected ray is known as the angle of reflection. The refracted ray or transmitted ray corresponding represents

the light that is transmitted through the surface. The angle between this ray and the normal is known as the angle of refraction, and it is given by Snell's Law [39].

It is important to provide a simple way to solve and understand the waveguide problems. These problems affect the reflection/transmission properties of the ray of light. Thus, we need to understand the relationship between amplitudes for reflection/transmission and the incident field amplitude at a dielectric interface.

Fresnel’s equations can be used to calculate reflection & transmission coefficients as well as the phase shifts for reflected and transmitted wave. The electric field perpendicular to the plane of incidence in an optical waveguide is called transverse electric (TE) mode, and the electric field parallel to the plane of incidence in an optical waveguide is called the transverse magnetic (TM) mode [6]. Assuming that, θ_1 is the angle of incidence, θ_2 is the angle of refraction, n_1 is the refractive index of the core, and n_2 is the refractive index of the cladding. The reflection coefficients r_{TE} and r_{TM} for different components, are described by the Fresnel's formulae as shown in the equations below [11].

For TE polarization:

$$r_{TE} = \frac{n_1 \cos\theta_1 - n_2 \cos\theta_2}{n_1 \cos\theta_1 + n_2 \cos\theta_2} \qquad \text{(Eq. 2.1)}$$

For TM polarization:

$$r_{TM} = \frac{n_2 \cos\theta_1 - n_1 \cos\theta_2}{n_2 \cos\theta_1 + n_1 \cos\theta_2} \qquad \text{(Eq. 2.2)}$$

Using Snell’s Law:

$$r_{TE} = \frac{n_1 \cos\theta_1 - \sqrt{n_2^2 - n_1^2 \sin^2\theta_1}}{n_1 \cos\theta_1 + \sqrt{n_2^2 - n_1^2 \sin^2\theta_1}} \qquad \text{(Eq. 2.3)}$$

And:

$$r_{TM} = \frac{n_2^{\,2}\cos\theta_1 - n_1\sqrt{n_2^{\,2} - n_1^{\,2}\sin^2\theta_1}}{n_2^{\,2}\cos\theta_1 + n_1\sqrt{n_2^{\,2} - n_1^{\,2}\sin^2\theta_1}} \qquad \text{(Eq. 2.4)}$$

θ_2 is derived from Snell's law:

$$n_1\sin\theta_1 = n_2\sin\theta_2 \qquad \text{(Eq. 2.5)}$$

The equations (2.1-2.4) are valid whenever θ_2 is a real angle. This is always true for external reflection, where $n_1<n_2$. But, when the light is incident in the material of higher refractive index ($n_1>n_2$), according to Snell's law, it is possible to choose an incidence angle θ_1 for which a real value of the angle of refraction θ_2 does not exist. This will occur for angles of incident $\theta_1>\theta_c$ where θ_c is the critical angle, $\theta_c = \sin^{-1}\frac{n_2}{n_1}$ (Eq. 2.6)

In fact, when the incidence angle is smaller than the critical angle, Fresnel's equations could be used. But, when the incident angle is larger than the critical angle, this will cause a total internal reflection (TIR). In this case all the power of the incident light is reflected, and then the amplitude of field reflectivity is unity [6]. Furthermore, we have to consider the phase shifts of the reflected waves as described in the following equations [11].

If θ_1 is greater than θ_c:

$r=\exp(j\phi)$ (Eq. 2.7)

Knowing that: $|r| = 1$

ϕ_{TE} and ϕ_{TM} are given by:

$$\phi_{TE} = 2\tan^{-1}\frac{\sqrt{\sin^2\theta_1 - \left(\frac{n_2}{n_1}\right)^2}}{\cos\theta_1} \qquad \text{(Eq. 2.8)}$$

and:

$$\phi_{TE} = 2\tan^{-1}\frac{\sqrt{\frac{n_1^{\;2}}{n_2^{\;2}}\sin^2\theta_1 - 1}}{\frac{n_2}{n_1}\cos\theta_1} \qquad \text{(Eq. 2.9)}$$

2.3 Optical waveguide modes:

Maxwell's equations are used to solve for an optical waveguide's modes. According to Maxwell's boundary conditions, the tangential component of an electric field must be continuous across the core-cladding interface, so part of the electric field which is called evanescent field is present on the outside of the waveguide. This evanescent field is used to detect the existence of any particle on top of the waveguide by measuring the change in the evanescent field in response to analyte binding [12].

In practice, waveguides are three-dimensional. But, the slab waveguide is considered as one of the simplest types among all the different waveguides structures. Thus, we can simplify it in 2-D model, where only x-z plane is considered. And this approximation can be applied on LEAC sensor waveguides. [6].

Assuming the simple slab waveguide shown in **Fig. 2.3**.To solve for an optical waveguide modes, we apply the Snell’s law to the air-waveguide core face boundary to find the maximum entrance angle θ_{0max}. Using θ_{0max}, the numerical aperture (NA) can be defined as following,

$$NA = n\sin\theta_{0max} = n_1\sin\left(\frac{\pi}{2} - \theta_{min}\right) = (n_1^{\,2} - n_2^{\,2})^{\frac{1}{2}} \qquad \text{(Eq. 2.10)}$$

Where θ_{min} is the critical angle, and n is the refractive index of the space outside the waveguide; hence in this case n=1.

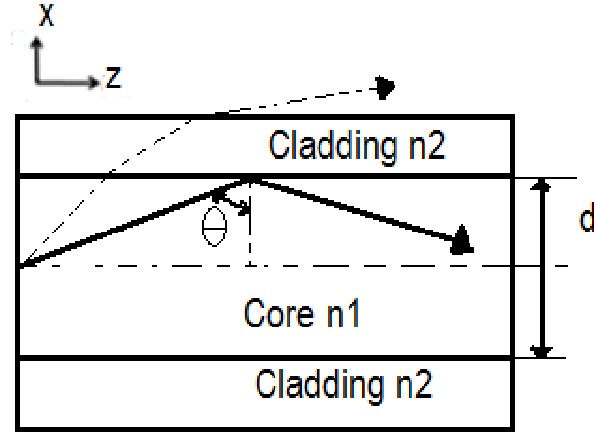

Figure 2.3: a) Light incident in a slab waveguide with angles $\theta > \theta_c$ are confined due to total internal reflection. **Reproduced from [6].**

The normalized frequency V in Eq. 2.11 is another important parameter that we need in solving a waveguide's modes. The mode number supported in the waveguide can be estimated using V number. This is a useful factor to design a single mode waveguide ($V<\frac{\pi}{2}$, for single mode slab waveguide), which is very important for LEAC biosensor [6].The reason for that is related to the requirements of leaky modes in optical waveguides sensors. Where only limited angles will propagate in the waveguide as guided "modes".

$$V=2\frac{\pi d}{\lambda}NA=2\frac{\pi}{\lambda}d\,(n_1^{\,2} - n_2^{\,2})^{\frac{1}{2}} \quad \text{(Eq. 2.11)}$$

Where d is the core thickness, n_1 is the core index, and n_2 is the cladding index.

We can describe the waveguide mode as a transverse field pattern. If we assume the propagation is in z-direction we consider constant amplitude and polarization profiles along the longitudinal z coordinate [12].

Assuming that we have an optical wave of angular frequency ω and free-space wavelength λ, the propagation constants in different regions of the waveguide can be defined as following,

$k_1 = n_1\omega/c$, $k_2 = n_2\omega/c$, where $n_1 > n_2$ and $k_1 > k_2$ (Eq. 2.12)

Generally, we consider the x-z plane as the plane of incidence in slab waveguides. In this case, the direction of net travel is in the z-direction, and the electric field vector lies entirely in the "xy" plane (i.e. E_z=0), which is perpendicular to the direction of net travel and this field is called transverse electric (TE). Moreover, if we assumed an infinite extent in the $\pm y$ direction, then E_x is also =0. **Fig. 2.4** shows a useful picture to understand the path of an optical ray in a waveguide.

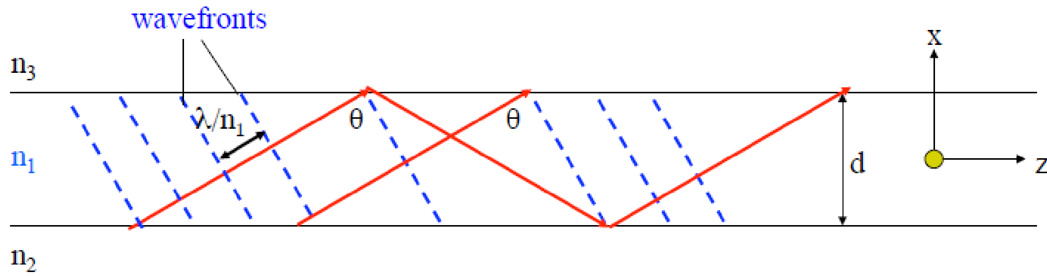

Figure 2.4: Intuitive ray and wavefront picture. **Reproduced from [12]**

Assuming $n_2 = n_3$ then $\theta_c = \sin^{-1}\frac{n_3}{n_1}$

As we demonstrated before, If $\theta > \theta_c$, the wave inside the core is totally reflected at both interfaces and is trapped by the core, resulting in guided modes.

Therefore, when the wave is reflected back and forth between the two interfaces, it interferes with itself, and a guided mode can exist only when a transverse resonance condition is satisfied.

In fact, when light completes a round trip in the x-direction, the total phase shift in the x-axis must be zero or a multiple of 2π to achieve self-consistency condition. Otherwise, if this condition is not satisfied this will lead into a destructive interference of the light waves, which leads to a diminishing of this mode [6].

In the core region as shown in **Fig. 2.5**, the x component of the wavevector represents the transverse component, $k_x = k_1 \cos\theta$ for a ray with an angle of incidence θ, while the z component represents the longitudinal component $\beta = k_1 \sin\theta$, and the k-vector triangle $k_1 = n_1\omega/c = (\beta^2 + k_x^2)^{\frac{1}{2}}$

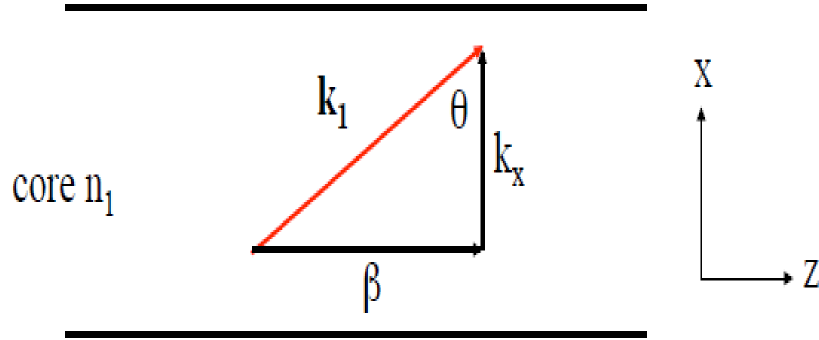

Figure 2.5: k-vector triangle. **Reproduced from [12]**

There are phase shifts ϕ_2 and ϕ_3 associated with the internal reflections in the lower and upper interfaces. Because ϕ_2 and ϕ_3 are functions of θ, the transverse resonance condition for constructive interference in a roundtrip transverse passage is [12]:

$$2k_1 d\cos\theta + \varphi_2(\theta) + \varphi_3(\theta) = 2m\pi \qquad \text{(Eq. 2.13)}$$

Where m is an integer = 0, 1, 2…

Since we can assume only integral values for m, only certain discrete values of θ can satisfy the transverse resonance condition. The transverse resonance condition results in discrete values of the propagation constant β_m for guided modes identified by the mode number m. Therefore, TE and TM waves have different solutions for the transverse resonance condition, resulting in different β_m and different mode characteristics for a given mode number m. So, for a given polarization, a solution of the transverse resonance condition yields a smaller value of θ and a correspondingly smaller value of β for a larger value of m. Therefore, $\beta_0 > \beta_1 > \beta_2 > \ldots$ [12]

The guided mode with m = 0 is called the fundamental mode and those with m ≠ 0 are higher-order modes.

By solving Maxwell's equations and applying the boundary conditions, and assuming a symmetric waveguide which has same upper and lower claddings refractive indices, we are able to write the E-field distributions in Eq. 2.14, A_m is the E-field amplitude [6]

$$E_m(x)=\begin{cases} A_m\cos(k_{x,m}d/2)\exp(-k_{xcladdingm}(x-d/2)) & -d/2\geq x \\ A_m\cos(k_{x,m}x) & -d/2\leq x\leq d/2 \\ A_m\cos(k_{x,m}d/2)\exp(k_{xcladdingm}(x+d/2)) & x\geq d/2 \end{cases} \qquad \text{(Eq.2.14)}$$

From the solution above and as shown in **Fig. 2.6**, we can realize that the exponential decay of the E-field in the cladding along x direction, and the propagation in the core along z direction

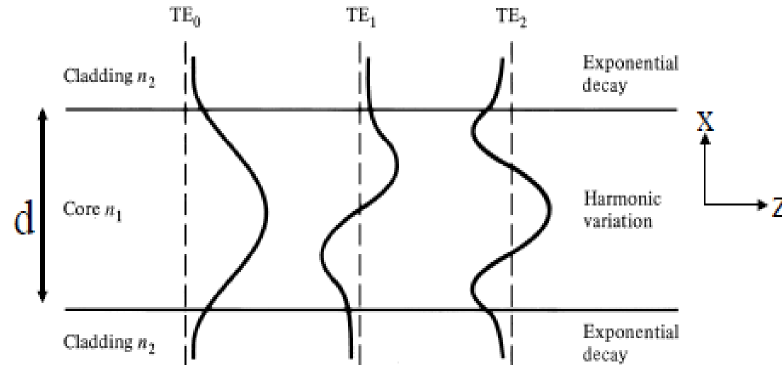

Figure 2.6: TE modes in a slab waveguide. **Reproduced from [12]**

All of the equations above are applied in the case of symmetric slab waveguide. However, for asymmetric slab waveguide the normalized frequency, V, propagation parameter, b, and asymmetry parameter, a, will be defined as following,

$$V=k_0d\,(n_1^{\,2}-n_2^{\,2})^{\frac{1}{2}}$$

$b=\frac{n_{eff}^{2}-n_{2}^{2}}{n_{1}^{2}-n_{2}^{2}}$, where n_{eff} is the effective index of the waveguide.

$a=\frac{n_{2}^{2}-n_{3}^{2}}{n_{1}^{2}-n_{2}^{2}}$

$Em= A_m\sin(k_{x,m}x)$ $\quad$ $-d/2< x<d/2$

Also, we will need to define decay constants, $\gamma_{u,}$ in upper cladding and γ_l in lower cladding as following,

$\gamma_u^2=\beta^2-k_0^2n_3^2$, $\gamma_l^2=\beta^2-k_0^2n_2^2$

The E-field decaying exponentially in the cladding is called the evanescent field. This field was the main reason for the possibility of using the optical waveguide as a biosensor. This field can be measured using near field scanning optical microscopy(NSOM), or using buried photodetectors on the lower cladding, which measure the change in the photocurrent in response to analyte binding on the upper cladding [6, 10, 11, 12].

2.4 Optical waveguide losses

2.4.1 Loss coefficient in optical waveguide related to the complex refractive index

It is important to know that the refractive indices of core, cladding or substrate are not necessarily real. In general the refractive index of dielectric materials is a complex number, and it can be defined as [11]:

$n=n_R+jn_I$ (Eq. 2.15)

The imaginary part of the refractive index will contribute a loss in optical waveguides. As shown in the following equations

We know from **Section 2.3** that the propagation constant can be defined as:

$k = nk_0$ (Eq. 2.16)

We have previously expressed a propagating field as:

$E = E_0 \exp(j(kz - \omega t))$ (Eq. 2.17)

Therefore if we introduce a complex refractive index to equations (2.15) and (2.16), we obtain:

$E = E_0 \exp(j(kz - \omega t) = E_0 \exp(j(nk_0 z - \omega t)) = E_0 \exp(j((n_R + jn_I) k_0 z - \omega t))$

$= E_0 \exp(j(n_R k_0 z - \omega t)) \exp(-n_I k_0 z))$ (Eq. 2.18)

Therefore there is a term $\exp(-k_0 n_I z)$. In the same way that the propagation constant in the z direction is re-designated β, this term is often re-designated $\exp(-\frac{1}{2}\alpha z)$. The term α is called the loss coefficient. The factor of $\frac{1}{2}$ is included in the definition above because, by convention, α is an intensity loss coefficient. Therefore we can write:

$I = I_0 \exp(-\alpha z)$ (Eq. 2.19)

Equation (2.19) describes how the intensity decays exponentially with propagation distance z, through a material.

2.4.2 The main sources of loss in optical waveguides

Losses in an optical waveguides originate from three sources: scattering, absorption and radiation. The main contribution of each of these effects is dependent upon the waveguide design and the quality of the material in which the waveguide is fabricated [11].

2.4.2. a Scattering loss

There are two main types of scattering in an optical waveguide, volume scattering and interface scattering. The imperfections in the bulk waveguide material, cause volume scattering and these include voids, contaminant atoms, or crystalline defects. While, the roughness at the interface between the core and the claddings of the waveguide is the main reason for interface scattering [26].

We usually assume a negligible volume scattering loss in normal dielectrics waveguide. But, it is really important to consider volume scattering in low-k dielectrics waveguides especially porous materials. Interface scattering should be considered in both low-k and normal dielectrics waveguides.

2.4.2. b Absorption loss

The absorption loss needs to be considered in case of semiconductor waveguide. The two main sources of absorption loss are, band edge absorption, and free carrier absorption.

Band edge absorption occurs when the energy of the incident photons is greater than the band gap of semiconductor material, then these photons is absorbed to excite electrons from the valence band to the conduction band, so this type of absorption is called inter-band absorption.

Therefore, if the light wavelength is longer than the absorption edge wavelength of the material, then the band edge absorption can be avoided [26]. Silicon is a good example to demonstrate the inter-band absorption. Graham T. Reed et al. [26] stated that silicon is used as a waveguide material for a wavelength longer than 1.1 um which is the approximate band edge wavelength of silicon. Since it absorbs very strongly for wavelengths shorter that 1.1μm, silicon is considered as a one of the most common materials that are used for photodetectors in the visible and at very short infrared wavelength range. However, as Graham T. Reed et al. [26] observed, “free carriers absorption may be significant in semiconductor waveguides. The concentration of free carriers will affect both the real and imaginary refractive indices”.

2.4.2. c Radiation loss

When a waveguide has a radiation loss that means there is a light leakage from the waveguide into the surrounding media. The surrounding media typically includes the upper or lower cladding, or for a rib waveguide, into the planar region adjacent to the guide [27]. The

main reasons that cause radiation loss include the unwanted perturbation in a waveguide such as a slightly damaged fabrication mask which will cause a light scattering from one mode into another. Thus, if the second mode is leaky this in turn results in some radiation loss.

Furthermore, some radiation loss of light occurs when there is a change in the angle of incidence at the wall of the waveguide which is caused if the waveguide has a curvature [26].

Since an integrated optical circuit is typically a few centimeters in length, is important to know what is the max propagation loss we can tolerate for an integrated optical waveguide. The widely accepted range for loss is of the order of 1 dB/cm. If the loss becomes much more than 1 dB/cm this will rapidly reduce the SNR for photodetectors. In addition, we should also consider that the additional losses such as the loss of coupling to or from the optical circuit, or losses within the circuit not associated with propagation loss, will make the operation of the sensor worse. To design a practical LEAC chip, we need to modify its parameters to get high SNR and high sensitivity optical waveguide. Optical losses are mainly caused by material properties and fabrication tolerances, which adversely affect sensor performance [26, 29, and 30].

2.4.3 Loss measurement in optical waveguides

Propagation loss is one of the most important parameters for evaluating the performance of optical waveguides. Traditional optical waveguides propagation losses measurement methods include waveguide direct cut-back [30], Fabry–Perot cavity measurement [26, 28], and scattered light collection [26, 29].

2.4.3. a The cut-back method

The cut-back method is one of the simplest methods that are used to measure an optical waveguide loss. A waveguide is cut to different lengths and each length is excited by one of the coupling methods such as end-fire coupling, the output power, and the input power to the

waveguide, in all cases are recorded [26]. For example, suppose we have a waveguide of length L_1 is excited by one of the coupling methods, and the output power from the waveguide, say P_1, and the input power to the waveguide, P_0 are recorded. The waveguide is then shortened to another length, L_2, and the measurement repeated to determine P_2. The propagation loss of the length of waveguide ($L_1 - L_2$) is therefore related to the difference in the output power from each measurement which can be expressed by [26],

$$\frac{P_1}{p_2} = \exp\left[-\alpha\left(L_1 - L_2\right)\right] \qquad \text{(Eq. 2.20)}$$

$$\alpha = \frac{1}{(L_1 - L_2)} \ln\left(P_2/P_1\right) \qquad \text{(Eq. 2.21)}$$

The cut-back method for measurements of propagation losses is based on a comparison of transmission through waveguides of different lengths and fitting the length dependence assuming identical coupling conditions and identical surface roughness. However, cut-back method has uncertain factors which can affect the measurement precision. For example, measuring propagation loss by comparing two optical powers before and after waveguide cutting has two uncertain factors. Firstly, the facet of the waveguide before and after cutting cannot keep the same conditions so the method is destructive; secondly, fiber coupling efficiency before and after cutting cannot keep constant [29].

2.4.3. b The Fabry-Perot method

The Fabry–Perot resonance method is advantageous for low-loss waveguides (< 1 dB/cm) [29]. In this method we consider the optical waveguide with polished end faces as a resonant cavity called a *Fabry–Perot cavity*, as the waves pass along the waveguide they undergo multiple reflections [26]. As Graham T. Reed et al. [26] observed, "Light propagates along the waveguide, and may be reflected at either facet, by an amount determined by the refractive index

of the waveguide material and the external media (usually air). However, any coating on the waveguide facet may change this reflectivity". Optical intensity transmitted through such a cavity, I_t, is related to the incident light intensity, I_0, by the well-known equation [11]:

$$\frac{I_t}{I_0} = \frac{(1-R)^2 e^{-\alpha L}}{(1-\mathrm{Re}^{-\alpha L})^2} + 4\mathrm{Re}^{-\alpha L} \sin^2(\varphi/2)) \qquad \text{(Eq. 2.22)}$$

Where R is the facet reflectivity, L is the waveguide length, α is the loss coefficient, and φ is the phase difference between successive waves in the cavity.

Equation 4.56 has a maximum value when φ = 0 (or multiples of 2π), and a minimum value when φ = π; that is [11]:

$$\frac{I_{max}}{I_0} = \frac{(1-R)^2 e^{-\alpha L}}{(1-\mathrm{Re}^{-\alpha L})^2} \qquad \text{(Eq. 2.23)}$$

$$\frac{I_{min}}{I_0} = \frac{(1-R)^2 e^{-\alpha L}}{(1+\mathrm{Re}^{-\alpha L})^2} \qquad \text{(Eq. 2.24)}$$

Therefore we can evaluate the ratio of the maximum intensity to minimum intensity as:

$$\xi = \frac{I_{max}}{I_{min}} = \frac{(1+\mathrm{Re}^{-\alpha L})^2}{(1-\mathrm{Re}^{-\alpha L})^2} \qquad \text{(Eq. 2.25)}$$

So we can find α by:

$$\alpha = \frac{-1}{L} \ln\left(\frac{1}{R} \frac{\sqrt{\xi}-1}{\sqrt{\xi}+1}\right) \qquad \text{(Eq. 2.26)}$$

Therefore if we know the reflectivity R, and if we can measure the ratio of the maximum intensity to minimum intensity ξ, the loss coefficient can be evaluated.

Although the Fabry–Perot cavity resonance method is considered to be a non-destructive method and can be free of the uncertain factors of the cut-back method, however, this method

requires long samples to obtain sufficient accuracy, but it is difficult to prepare them in photonic integrated circuits (PIC) fabrications. Also, it requires the two facets of the waveguide to be reflective, a constraint that sometimes cannot be met in some configurations [29].

2.4.3. c The measurement of scattered light

In fact, this method is to measure the scattered light from the surface of a waveguide, but it can also be used to determine the loss. This method is assuming that the amount of light scattered is proportional to the propagating light. Therefore, if scattered light is measured as a function of waveguide length, the rate of decay of scattered light will follow the rate of decay of light in the waveguide [26]. To collect the scattered light from the surface of a waveguide we can use optical fibers, and then they can be scanned along the surface. As a result, an image of the entire surface can be made, and the decay of scattered light determined accordingly. However, if the power propagating in the waveguide is high and correspondingly the waveguide loss is high, then the light is scattered significantly so we can collect it [26]. Thus, this method tends to be used when losses are high, but it is favorable to use other methods when waveguide has been optimized. As Graham T. Reed et al. [26] observed, "This technique requires homogeneity in the structure through the overall length of the waveguide and a good light scattering image on the vertical surface of the guiding structure so that the camera can efficiently capture it".

2.4.4 Loss calculations in optical waveguides

Since we will focus on surface and volume scattering losses modeling in chapter 3, in this section, we will talk about one of the main scattering losses in silicon on insulator (SOI) waveguides caused by the sidewall roughness. This scattering loss highly depends on the waveguide dimensions especially the waveguide width.

K.Lee et al. [33] used both experimental and theoretical approaches to predict the dependence of loss on waveguide dimensions and sidewall roughness. They measured the transmission loss of a Si/SiO_2 strip waveguide using the cut-back method, to demonstrate the relationship between the transmission losses of the dielectric silicon waveguide and its dimensions. Furthermore, they proved that a major source of loss comes from sidewall roughness. Also, they employed a theoretical model to predict the relationship between the transmission losses of the dielectric silicon waveguide and its width. This model accurately predicts that loss increases as waveguide width decreases.

Using an analytical relation between the scattering loss and the sidewall roughness, the sidewall roughness can be modeled and described by an exponential or Gaussian autocorrelation function as demonstrated by Payne and Lacey [34]. They stated that this approach relates the attenuation coefficient to the standard deviation σ and the autocorrelation length L_c of the sidewall roughness [33, 34]. Therefore, as demonstrated by Payne and Lacey[34] the sidewall roughness can be described by a real space function say f(z), so by measuring the deviation of f(z) from the linear mean of the sidewall we can obtain the standard deviation σ, and L_c is obtained from the autocorrelation function C(z) of f(z).

Assuming that the roughness can be described by an exponential or Gaussian autocorrelation function [34], the attenuation coefficient α can be expressed by

$$\alpha = \frac{\sigma^2}{\sqrt{2} k_0 w^4 n_1} \, gf \qquad \text{(Eq. 2.27)}$$

Where σ is the standard deviation of the roughness, k_0 is the free space wavevector, w is the half width of the waveguide, and n_1 is the index of the core. g and f are functions of various parameters defined by Payne and Lacey[34]. This equation can be used for both exponential and

Gaussian approximations; the only difference is the function "f" which has different definitions for different approximations. f is defined in [34] as $f_G(x,y)$ for Gaussian approximation, and as $f_e(x,y)$ for exponential approximation.

2.4.5 Modal loss

Within a dielectric waveguide, the loss is not uniform throughout the volume occupied by the optical modes of interest. In fact, the material loss is different in different regions of the waveguide and the lossy material may only occupy a few percent of the volume occupied by the optical modes. Therefore, we can define the modal loss as the net loss provided to an optical mode [40].

In designing a LEAC sensor it is worthwhile to know the modal loss. In fact, the modal loss is what we can measure by experiments. In low-k dielectrics LEAC sensors we assume that the contributions of the upper cladding and the core to modal loss are negligible compared with the loss in lower cladding, because of the assumption of having negligible volume scattering losses i.e. material losses in both core and upper cladding. Thus, having the material loss in a LEAC chip we can find the modal loss. The material loss represents the loss caused by the materials properties in all layers individually, core, lower and upper claddings and this represented by volume scattering in our case.

Assuming $\alpha_{material}$ is the material loss, α_s is a surface scattering loss, $\alpha_{absorption}$ is the photodetector coupling loss, and Γ, $\Gamma_{lowercladding}$, and $\Gamma_{uppercladding}$ are the confinement factors in core, lower and upper claddings respectively , and then the modal loss can be found using the following relation,

$$\text{Modal loss} = \alpha_s + \alpha_{absorption} + \alpha_{material_lower\ cladding} * \Gamma_{lowercladding} + \alpha_{material_core} * \Gamma + \alpha_{material_upper\ cladding} * \Gamma_{uppercladding} \quad \text{(Eq. 2.28)}$$

Therefore, to find the modal loss we need to find the percentage of power confined in each layer i.e. the confinement factor in each layer. In common, the confinement factor is used to represent the amount of power propagates inside the core. Or in other word it is the ratio of the power within the core to the total guided power of the waveguide. But, here I used the term confinement for all layers to represent the percentage of power in each layer.

To find the modal loss, I will neglect the last two terms in Eq. 2.28, assuming negligible material losses in the core and the upper cladding.

Hence, to find the confinement factor in lower cladding, we will have to find the confinement factor in the core. Assuming a slab waveguide defined in Sec. 2.3, the confinement factor of the core is defined by [10],

$$\Gamma = \frac{\int_{-d/2}^{d/2} E_y{}^2(x)dx}{\int_{-\infty}^{\infty} E_y{}^2(x)dx} \qquad \text{(Eq. 2.29)}$$

We can simplify Eq. 2.29 assuming that we are interested to work on the fundamental mode, and then the confinement factor for a symmetric waveguide can be defined by Eq. 2.30[38]

$$\Gamma = \frac{1+\dfrac{2\gamma d}{V^2}}{1+\dfrac{2}{\gamma d}} \qquad \text{(Eq. 2.30)}$$

Where $\gamma = k_0\sqrt{n_{eff}{}^2 - n_{lowercladd}{}^2}$

n_{eff} is the effective index of the waveguide, $n_{lowercladd}$ is the refractive index of the lower cladding

Knowing that $V = k_0 d\sqrt{n_{core}^{2} - n_{lowercladd}^{2}}$, then the confinement factor can be approximated by,

$$\Gamma \approx \frac{V^2}{V^2 + 2} \qquad \text{(Eq. 2.31)}$$

n_{core} is the index of the core

Assuming asymmetric waveguide we need to find the amount of confinement in lower cladding which is different from the confinement in upper cladding. The following is the general equation to find the lower cladding confinement,

$$\Gamma_{lowercladding} = \frac{\int_{-\infty}^{-d/2} E_y^{2}(x)dx}{\int_{-\infty}^{\infty} E_y^{2}(x)dx} \qquad \text{(Eq. 2.32)}$$

This equation can be simplified using the confinement equation above by,

$\Gamma_{lowercladding}$ =lower cladding confinement = $\dfrac{n_{lowercladd}}{n_{lowercladd} + n_{uppercladd}}(1-\Gamma)$ (Eq.2.33)

Finally, to find the modal loss we apply the following equation:

Modal loss= $\alpha_{material_lower\ cladding} * \Gamma_{lowercladding} + \alpha_s + \alpha_{absorption}$ (Eq.2.34)

2.5 Fabrication process

In this section, we describe the general steps that are used to fabricate any device. Successful chip fabrication requires careful attention to detail and a good understanding of each individual step in the entire process. Each step must be inspected with a microscope before moving onto the next step whenever possible. In fact, it is very important to understand every step in details to ensure a successful fabrication.

2.5.1 Cleaning

It is necessary to clean the silicon wafer before starting the fabrication process to remove any contamination. If we fail to properly clean the sample this will result in unwanted defects. In order to clean the sample, acetone is usually used as solvent to clean off any contamination where the sample is sprayed with acetone and then submerged in it. This treatment will remove common stains and particles. As complementary solvents ethanol is used to rinse off any residue left after the acetone treatment. After rinsing, compressed nitrogen is used to dry the sample [8, 13, and 14].

2. 5.2 Pre-bake

After cleaning the sample we have to minimize the amount of moisture on the sample to make the spinning on resist easier and faster. This will ensure good adhesion between the film and the resist. To achieve this, a dehydration bake on 100 ˚C hot plate is performed for around 6 minutes, which will help evaporating the moisture adsorbed on the film surface [8, 13].

2.5.3 Spin-coat

After cleaning and prebaking, photoresist is dripped onto the sample covering it. The sample is then spun for 40 s at 4000 rpm, distributing the resist evenly across the sample [8].

2.5.4 Soft bake

After achieving a uniform resist thickness, the sample is put through a soft-bake process. The purpose of soft bake is to alter the properties of the resist in such a way that it is ready for exposure. Most of the solvents in the resist are driven-off by baking the sample. The soft bake improves the adhesion to the film, improves the uniformity and solidifies it. It is usually performed on a hot-plate with a temperature of 100 ˚C for 60 s [8, 13].

2.5.5 Alignment and Exposure

After the soft-bake, mask alignment and exposure is performed with a contact aligner. Different masks can be used for the fabrication process, as an example, for the optical waveguide designed at CSU lab, the mask used to fabricate the chips was a 3 by 3 grid consisting of 9 unique designs, as pictured in **Fig. 2.7.** The bottom left sector of the mask contains the nine designs needed to create the buried detectors, the top left quadrant contains the mask designs for the metal layer, the bottom right quadrant of the mask design creates the waveguide, and finally, the upper right quadrant represents the via layer. This layer is the very last step in chip fabrication as it is the mask used to etch material down to the metal pads to expose them for probing [7, 8, and 13].

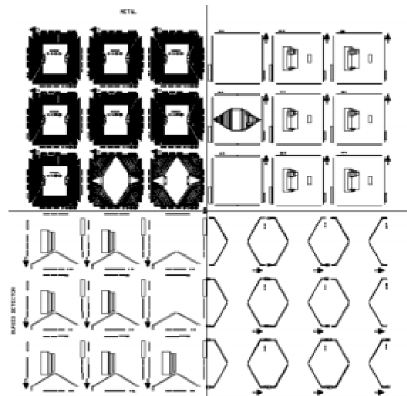

Figure 2.7: LEAC chip mask designs. **Reproduced from [7]**

In order to transfer these patterns onto a die, the die is first coated with photoresist as described in the previous sections. The die is then placed onto the vacuum chunk of the contact aligner and the relevant mask is cleaned and mounted into the system with the chrome layer down towards the die. To facilitate independent movement of the mask and die, there is a small gap between these at this point. Using the mask aligner controls and the microscope, the mask is aligned with the die [7, 8].

After alignment, the mask and the die are brought into contact with each other. The UV light is then engaged, exposing the photoresist. The duration of the exposure depends on the resist. The exposure time for positive photoresist is around 6.2 s, but for negative photoresist is 22 s [7, 8, and 13].

After exposing the photoresist, it is good to make post-baking at 150ºC before developing to help remove or reduce standing wave phenomena caused by destructive and constructive interference patterns of the incident light [8,13].

Now we can start the development. In the case of positive photoresist, the parts of the photoresist that have been exposed to UV light have been softened are soluble in the developer chemical and it takes 45 s to finish the development, but the negative photoresist behaves in an opposite manner, with the exposed parts hardening and becoming insoluble in the developer and it takes 85 s to finish the development [8, 13].

The develop chemistry is delivered by spinning the wafer very fast into the developer, which often contains sodium hydroxide NaOH. After removing the die from the developer, it is promptly dipped in de-ionized (DI) water for 20 s in order to stop the development and clean-off the developer. The resulting wafer is hard-baked at (120 -180) ºC, this step is required to get

further curing for the resist and solidify the remaining photoresist to make a more durable protecting layer and to withstand the etchant better [8,13,14].

2.5.6 Etching [8, 13, 14]

After developing and hard-baking the photoresist, the remaining photoresist pattern will protect the layer under it. There are two types of etching, wet etching and dry etching. Wet etching is an isotropic and is done by using wet chemical solution. Dry etching is an anisotropic etching and is done using plasma, it is very selective, but with low etch rate. In CSU clean room plasma etching is mostly used. An O_2 plasma treatment is used, prior to etching, to clean the wafer to remove any residual scum that can't be seen under the microscope, For nonselective etch processes, the etch rate must be first determined by noting the etch depth per time on a dummy sample run. Etch processes may also make use of an etch stop layer which has a much lower etch rate than the overlying target material. In this case, the etch depth is not such a strong function of etch time. Using the determined etch rate, fully etch or partially etch of the layer to a desired depth. After this step, clean the chip with acetone, methanol, and DI water to remove photoresist, and then dry using N_2 gas. Inspect under microscope and note any irregularities in the layer. The layer should look smooth or it will be excessively lossy.

2.5.7 Metallization [8, 13]

After etching a die, the die is coated with negative resist, exposed, developed, and hard baked. The die is mounted for electron beam physical vapor deposition (EBPVD) on a sample holder, later in the process, the end surfaces will be polished to facilitate coupling of light into the waveguide.

Polishing on a die with metal layer may cause bits of metal to break loose which in turn may disturb the polishing process and induce micro scratches .To avoid this problem, the edges of the

die is masked out with household aluminum foils, only leaving the essential parts of the metal structure (i.e. electrodes and contact pads).The sample is then inserted into the vacuum chamber of the EBPVD system and the metal is deposited.

2. 5.8 Lift-off [8, 13]

After the metal has been deposited, the die is removed from the EBPVD-system. Except for the edges which were masked out by aluminum foils, the entire die is covered by metal. When we remove the underlying photoresist, only the electrodes and contact pads will remain. In order to remove the negative photoresist, the die is first soaked in acetone for 15 min. Subsequently, it is sprayed with acetone from an airbrush, removing most of the resist.

In order to remove the photoresist in narrow spaces (such as the gap between electrodes), the die is placed in an acetone filter beaker. This beaker is then covered and placed into an ultrasonic bath for 5 minutes. In some cases it is necessary to increase the time in the ultrasonic bath. Any remaining photoresist should be removed using an acetone soaked brush or swab. However, this should be done carefully in order to avoid scratching the surface and waveguides excessively. After all of the resist and excess metal has been removed, the sample is cleaned and inspected for defects.

2.6 Review of previous work on LEAC sensors

The initial concept of a novel immunoassay LEAC biosensor was demonstrated in 2005 by Yaun *et al*. [3] at CSU. They described the need for novel optical biosensors that can detect multiple analytes for biological and environmental applications. The CSU group investigated the use of LEAC chip in detecting dried target films, such as proteins, DNA, and they developed the device to be used in virus detection [1-9].

Near-field scanning optical microscopy (NSOM) was used as an effective measurement tool to directly measure the change in the optical intensity due to the adlayers on the waveguide. The LEAC was made from SiNx core, SiO_2 lower cladding, and air as upper cladding. In Ref [17] NSOM was used to demonstrate the response of patterned C-reactive protein (CRP) immunoassay-complexes with immobilized anti-CRP antibody and multiple CRP concentration. The NSOM results showed that the intensity modulation ratio sensitivity on a waveguide's top surface arising from a 1 nm change in thickness of a 15 nm nanofilm is approximately 1.7%/nm

However, many research works have been done to develop portable LEAC sensor by placing buried detectors array in lower cladding. Guangwei Yuan et al. [18] demonstrated a compact planar dielectric waveguide with buried detector arrays. The detector array is placed in the lower cladding regions of the waveguide, each detector element opposites a region of a specific antibody type. Local changes in the evanescent fields, which indicate the presence of adsorbed species on the upper surface of the waveguide, can be sensed by detector array elements.

Fig. 2.8 shows the sensing mechanism of the LEAC sensor with buried detectors array, it shows the change in the local evanescent field due to bound analytes. Buried array of detectors along the length of the waveguide are shown. The detectors can sense the modification in the evanescent field due to local adlayers of bound analytes.

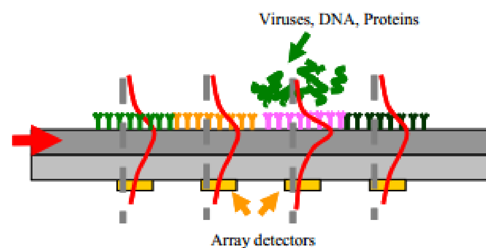

Figure 2.8: Bio-adlayers binding on a single-mode optical waveguide effectively increases the thickness of the core layer, thus decreasing the evanescent field tail absorbed by the underlying detector. The solid curves illustrate the waveguide mode profiles at different positions along the light propagation direction. **Reproduced from [3]**

The LEAC sensors with electronic readout circuits were developed and had been fabricated in a commercial 0.35 μm CMOS technology at the Avago technologies facility in Fort Collins, Colorado. The sensor structure was engineered with high sensitivity to local refractive index changes and adlayer thickness. Relatively large core to detector distances can provide very large normalized current modulation due to changes in surface film thickness, according to Eq. 2.35, the modulation ratio decays exponentially as a function of contact spacing [1, 5, 8, and 17].

$$\frac{\Delta I}{I} \approx \frac{\exp(-2\gamma_{film}s) - \exp(-2\gamma_0 s)}{\exp(-2\gamma_0 s)} = \exp(-2(\gamma_{film} - \gamma_0)s) - 1 \qquad \text{(Eq. 2.35)}$$

Where s is the distance below the waveguide

s: it represents the distance between the core and photodetectors, and it is equal to the lower cladding thickness

$\gamma_{0:}$ is the decay constant before film adsorption.

γ_{film}: is the decay constant after film adsorption .

For a very thin adlayers, the modulation ratio $\Delta I/I_0 \approx -2\,(\gamma_{film} - \gamma_0)\,s$, which makes the normalized response proportional to the detector distance from the core.

Fig. 2.9 demonstrates the operation mechanism of a LEAC sensor. Where nanoscale organic layers, such as those formed by the binding of target antigens or antibodies, increase the effective refractive index just above the silicon nitride waveguide core and hence shift the evanescent field profile away from the underlying buried detectors, reducing the associated photocurrent. An asymmetric waveguide structure amplifies the modulation of light intensity below the waveguide where the buried detector array is placed.

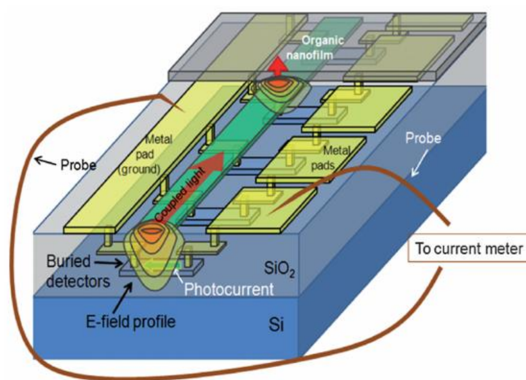

Figure 2.9: Schematic diagram of a LEAC biosensor CMOS chip where evanescent field distribution shifts up upon reaching the organic nanofilm, resulting in decreased photocurrent in detectors under the film. **Reproduced from [18]**

In his experiment Yan et al. [20] used both NSOM and integrated buried detectors to study the response to patterned organic nanofilms including immunocomplexes, photoresist, and adsorbed bovine albumin (BSA) layers. Using NSOM, the response of the LEAC sensor to CRP immunocomplexes was detected and 5% modulation ratio was measured for a 3 nm adlayer thickness change. To study the characteristics of the buried detectors array, both the thinned photoresist and a ~1-nm thick BSA nanofilm had been used and a very high sensitivity of 15%/nm was demonstrated for the BSA film.

The measured and simulation results confirmed the successful operating mechanism and the high intensity ratio that can be achieved using the buried detectors array with large separation from the core. Furthermore, Measurement established the low temperature dependence of the LEAC sensor.

Although the chip has successfully validated the LEAC sensing concept, multiple issues needed to be addressed in order to realize the full potential of the LEAC chip as a competitive sensing platform. The chip exhibited excessively high scattering losses of roughly 90 dB/cm, which resulted in reduced sensitivity and it inhibited multi-analyte detection as there was little

optical power left in the guided mode after passing through the first analyte region to probe more regions along the waveguide.

Furthermore, the chip exhibited low photocurrents in the range of 10-100 nA, which required amplification by a factor of up to 500 million (V/A), resulting in both increased amplifier noise which limit the SNR and sensitivity [8]. Furthermore, the chip could not perform real-time sensing and lacked fluidic compatibility.

Erickson et al [5]. Described the optimization of LEAC biosensors to enable real time measurements of refractive index change on a CMOS fabricated chip. He optimized the performance of the LEAC device by modifying the CMOS compatible fabrication scheme and fine-tuning waveguide parameters based on simulation results of a full-vector finite difference matlab modesolver. He demonstrated the use of reference region of known refractive index followed by sensing region to get real time measurements, and provided an analytical scattering model assist the design and understand the effects of fabrication on scattering loss.

A new integrated photodetector has been fabricated, which both eases fabrication and generates very low dark currents, producing a photocurrent to dark current ratio of greater than 50 in the sensing region.

As shown in **Fig.2.10**, the main principle of operation of the LEAC chip is the local evanescent field shift effect. If the upper cladding refractive index increases, the evanescent field shifts up and away from the photodetector, resulting in less photodetector coupling loss and a corresponding decrease in the measured photocurrent in the underlying photodetector.

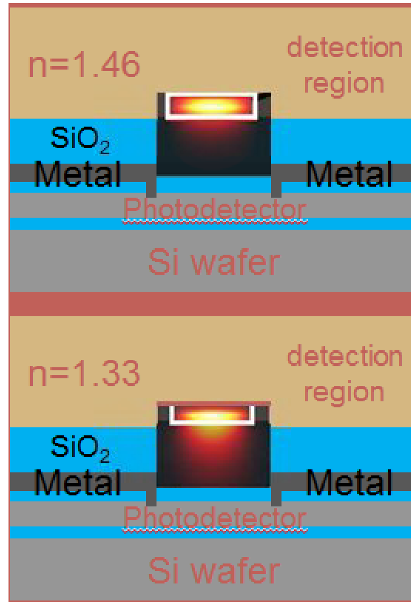

Figure 2.10: Cross sectional diagram of LEAC structure, which indicates field shifting in response to changes in upper cladding index. Note that for the higher index upper cladding (n = 1.46), the field is shifted up and away from the underlying photodetector, whereas there is much greater field overlap with the detector for the lower index (n = 1.33) upper cladding.

Erickson demonstrated the optimization of the device using a full-vector 2-D finite difference mode solver which solves the leaky modes of the LEAC waveguide and determines the coupling losses. The simulation results show the high dependence of the device sensitivity and the scattering loss on the lower cladding thickness and the waveguide core height. **Fig. 2.11** shows the photodetector coupling loss as a function of the oxide thickness t_{oxide}, ridge height H, and upper cladding index.

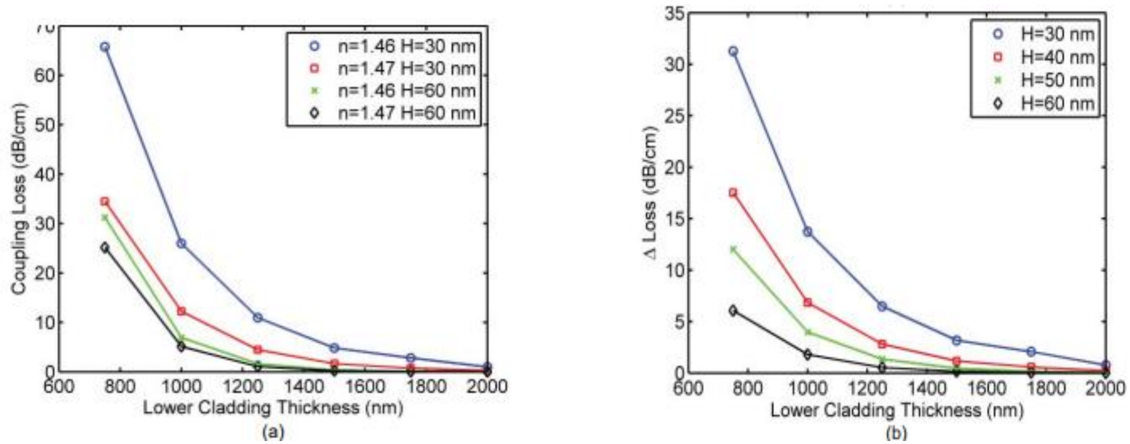

Figure 2.11: (a) Coupling loss for waveguides as a function of lower cladding thickness, core thickness H and upper cladding index n. (b) Difference in coupling loss for an upper cladding refractive index of 0.01 refractive index unit(RIU) as a function of lower cladding thickness and H. **Reproduced from [5]**

Fig. 2.11 shows that the photodetector coupling loss decreases as the upper cladding refractive index increases due to the evanescent field shift effect, and photodetector coupling loss approaches zero as lower cladding thickness increases.

In general, by reducing the core thickness and driving the waveguide closer to cut off the device sensitivity is maximized. Also, the sensitivity increases by increasing the lower cladding thickness. However, there is a design tradeoff, the photodetector coupling losses rapidly decrease by increasing the lower cladding thickness and this will reduced the measured photocurrent, and the signal will be overwhelmed by the photodetector noise.

Absorption loss was negligible, but scattering loss was the dominant in Erickson's waveguide. In general, sidewall scattering loss in ridge waveguides is inversely proportional to the fourth power of the largest guiding dimension, so to reduce it he increased the waveguide width to 7 um versus 2 um he used in prior work.

Using the optimized LEAC chip, Erickson et al. [8] could make a real time fluidic measurement with an integrated fluidic channel, with minimal resolvable change in refractive index sensitivities of 4.6×10^{-6} and 4.1×10^{-5}, respectively.

Fig. 2.12 shows a real-time refractive index sensing results performed by flowing oils into the fluidic chamber in the following order: sesame, blend, peanut, sesame. The photocurrent was measured on the second detector in the sensing region (#7) and normalized to the third detector in the reference region (#3). Oils were injected manually using a syringe in 20 s intervals and care was taken to strain relieve the tubes, in order to minimize coupling misalignment caused by fluid flow [8]. Where $I_{normalized}=I_{sensing}/I_{reference}$. (Eq. 2.36)

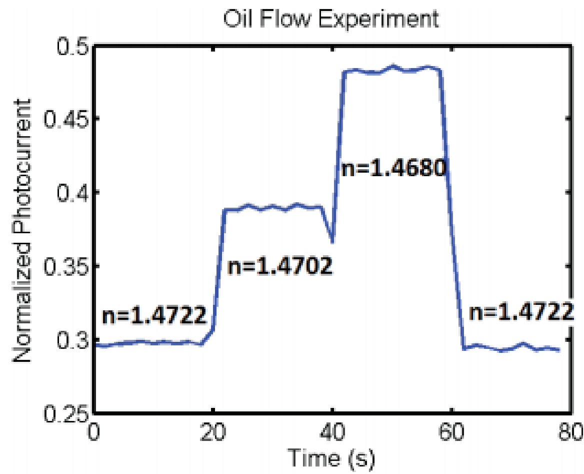

Figure 2.12: Real-time refractive index sensing. Three fluids of known refractive index were made to flow through the chamber in 20-s intervals to validate the real-time sensing capabilities of the chip. **Reproduced from [5]**

2.7 Low-k dielectrics

In communication systems, it is important to meet the increasing demands performance for high data rate and reduced signal attenuation. So, the microelectronics industry is required to deliver new technology solutions that will include new device architectures, with smaller dimensions, and new materials with low parasitic capacitance.

In recent years, low dielectric constant (low-k) material, has been developed to replace the conventional SiO_2 as the interlayer dielectric (ILD) in integrated circuits (ICs), and it can be used as an insulator between metal wires in IC interconnects. Low-k dielectrics play an important role in improving the speed of electrical and optical communication systems [24].

2.7.1 What is low-k dielectric?

A low-k dielectric is one kind of dielectric materials which has lower dielectric constant than silicon dioxide SiO_2. The implementation of low-k dielectric material is required to allow continued scaling of microelectronic devices and extending Moore's law. In ICs dielectric material is used for insulating the conducting parts from one another. As the number of components in ICs increases and they become very close together, the insulating dielectrics have thinned to the point where the charge build up and crosstalk affect the performance of the device. Replacing the high-k dielectric such as SiO_2 with a low-k dielectric of the same thickness reduces the parasitic capacitance, enabling faster operating speed [25].

The range of low-k dielectric materials which are used today includes either ultra low-k ($k<2.2-2.4$) or low-k ($2.4<k<3.5$). There are two main deposition methods that are used to deposit low-k dielectric materials, the first method is SOD (spin-on-dielectrics), and the second method is CVD (chemical vapor deposition) or plasma enhanced CVD (PECVD). The main factors that affect the final properties of these materials are the deposition method and post deposition treatment steps, such as anneals, or chemical treatments [25, 41].

2.7.1.1 Spin-on low-k Dielectric materials (SOD)

The SODs mainly include polymers or organically modified SiO_2 (OSGs, or organosilicate glasses). Many organic or inorganic low-k films are created by spin-on process, such as Hydrogen silsesquioxane (HSQ), Methylsilsesquioxane (MSQ) and SiLK^{TM} resin from Dow

Chemical etc. as an example, IBM designers use typical spin-on dielectric SiLK^{TM} from Dow Chemical for their 0.13 micron process.[25, 41]

One of the most important extensions in using SOD is the increase of the material's porosity. Where the porosity represents the ratio of free space (or air) to that of the solid dielectric. In fact, the range of the materials k-value is $k \geq 1$, and air has the lowest k-value. Since air gaps have low breakdown voltage, low strength and low thermal conductivity, we can't use them as low-k dielectrics. Therefore, one of the most important ways to produce low-k material is depositing one with a reduced density, i.e. increased porosity. Hence, there are many companies produce low-k dielectrics by adding porosity to dielectric materials. In addition, the low-k SODs have well-controlled molecular properties with k values ranging from 2.0-2.6. Xerogels and aerogels are considered as one classification of porous materials made by SOD. Aerogels are highly porous solids formed by replacement of a liquid in a gel with a gas. On the other hand, xerogels are formed from a gel by drying it with unhindered shrinkage. These nanoporous silica material typically has a dielectric constant value between 1.0 and 3.0, and that depends on the porosity of the material [25, 41].

2.7.1.2 CVD low-k materials

Silica-based low-k films are formed by CVD, where the dielectric constant of these materials is reduced by doping SiO_2 films with carbon C or fluorine F etc. Moreover, the main factors that determine the porosity of these materials are reactor dimensions, the deposition temperature, and the pressure [25, 41].

The recent candidates of CVD low-k materials which are made by different foundries include Black Diamond™ and Black Diamond II™ (Applied Materials), CORAL™

(Novellus), and Flowfill™ and Orion™ (Trikon). These amorphous materials are commonly described as SiCOH, based on a primary silicate (SiOx) structure with organic species (CxHy) that can either be bonded with the silicate or trapped within the silicate structure[1,2].

Adding porosity to low-k dielectrics is one of the good methods that are used to control and reduce the k-value for these materials. However, porous materials may cause problems in integration and manufacturability due to their mechanical strength. Thus, we need to control the porosity and pores size to improve the materials adhesion and integration. For example.as pores become smaller, the mechanical strength of the layer increases [25, 41]. As Stephen Beaudoin et al.[41] observed in their low-k dielectrics update, "To create porous dielectric films, a sacrificial species can be chemically bonded to the dielectric matrix and later decomposed to form nanometer-scale voids in the low-k. Alternatively, by judicious choice of precursor and processing conditions, it is possible to deposit dielectric materials that have significant internal porosity at the nanoscale. The pores in low-k SODs are typically as large as 20 nm while those in PECVD or CVD materials are closer to 10 nm".

2.7.1.3 Table 2.1: An update on low-k dielectrics

Low-k dielectric	k(dielectric constant)	n (refractive index)	Method of deposition	Foundries	Ref
Fluorine-doped SiO_2	2.4-2.8	1.46485@ 365 nm 1.46009@ 404.6 nm 1.4573 @435.8nm 1.44282@ 894.35 nm F=2% [5]	HDPCVD (high density plasma chemical vapor deposition) to produce fluorinated silica glass	Taiwan Semiconductor Co , Ltd , Hsinchu , Applied Materials Taiwan	41 ,45,46
Carbon-doped SiO_2	2.8-3.5	Less than 2	By doping SiO_2 with carbon by SOG or CVD	Novellus Inc. Trikon Technology Ltd, Institute of Microelectronics, Singapore 117685 Institute of Materials Research & Engineering, Singapore 117602	41,6,7
Porous SiO_2 (Aerogels/Xerogels)	1.1-2.5	1.17±0.08 @650 nm	Creating voids or pores using various methods such as electrochemical etching.	IBM DOW chemical Honeywell Texas instruments	41,60,43
Porous carbon-doped SiO_2	Less than 2	1.39-1.42	By UV curing, floating methyl groups in carbon-doped SiO_2.	IBM Dow chemical	41,45, 46
Spin-on organic polymeric such as: BCB, polyamides./ fluorinated polyamides	2.6-2.8/ 2.5-2.9	BCB:1.552 @ 600 nm ,1.537@ 1310 nm,1.535 @1650 nm [3]	Spin-on	IBM Dow chemical	41,60,42, 43
Si based polymeric such as :HSQ ,MSQ. where HSQ is hydrogen silsesquioxane, an interconnected network of $(H\text{-}SiO_{3/2})_n$ units. MSQ is methyl silsesquioxane, an interconnected network of $(CH_3\text{-}SiO_{3/2})_n$ units.	2-3.3	1.37	Spin-on	IBM Dow chemical National Taiwan University.	41 , 60,43
Black-diamond (SiOCH)	2.2-3.5	1.46 @ 633 nm 1.5 @ 248 nm 1.59 @ 193 nm	PECVD	TSMC Applied Materials Inc. Texas instrument	41,43
Diamond like carbon(DLC) / fluorinated	2.7-3.4 / 2.4-2.8		PECVD	Applied Materials Inc. Texas instrument	41 , 60
PTFE (Teflon)	1.9	**AF1300** :1.432 @157 nm 1.38 @172.2 nm 1.364 @ 185.1 nm 1.329 @ 248 nm	Spin-on		60,43,48
Porous MSQ/porous HSQ	1.8-2.2/1.7-2.2	Porous HSQ: 1.388-1.369 Porous MSQ@630 nm : porosity | Index 0.398 | 1.627 0.496 | 1.516	Spin-on	IBM Dow chemical	25,43,46
Porous SiLK	1.5-2	Porosity @633 nm 10% | 1.588±.006 20% | 1.570±.004	Spin-on	IBM ,Dow chemical Veeco Instruments	25,43, 49

2. 7.2 Why do we need low-k dielectrics for electrical interconnects?

The complexity of the integrated circuits has increased from small scale integration (SSI) to medium scale integration (MSI) to large scale integration (LSI) to very large scale integration (VLSI), and finally to the present ultra large scale integration (ULSI). According to Moore's law, there is an exponential growth in the number of transistors per integrated circuit (doubling of transistors every couple of years) and in his prediction this trend would continue. So to achieve Moore's law and to have so many components on same chip, the dimensions of each device have to be decreased [25]. Therefore, this will increase the wire density and the number of metal levels on same chip. As a result, this will lead to an increase in the signal delay, the metal line cross-talk capacitance, and metal resistance [24, 25].

Fig. 2.13 shows the dependence of signal delay on device size. It was shown that below a certain distance of the interconnecting lines, the signal delay is dominated by RC delay of the interconnect. Clearly, below certain device size, the RC delay becomes the limitation factor of the device operating speed [25].

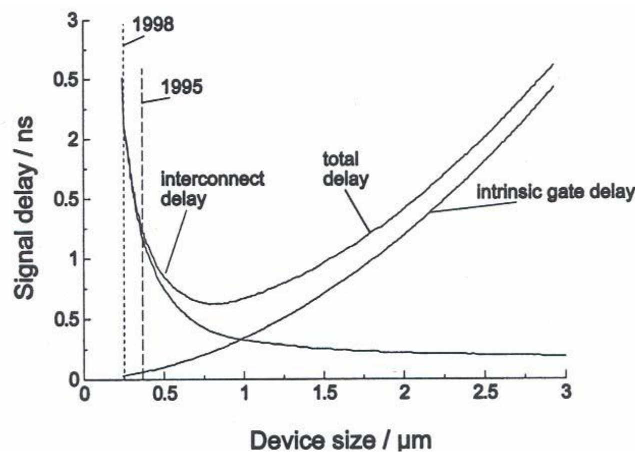

Figure 2.13: Dependence of signal delay on device size. **Reproduced from [25]**

RC delay can be calculated using the following equation [25]:

$\tau = RC = 2\rho k \varepsilon_0 [4L^2/S^2 + L^2/t^2]$ (Eq. 2.37)

Where τ —signal delay time

R—the resistance of metal

C—the parasitic capacitance

ρ —the specific resistance of the metal

k—the dielectric constant (the permittivity) of the dielectric.

ε_0—the dielectric constant of vacuum

L—the length of the metal

S —the distance between two metal lines

t—the thickness of dielectric

From Eq. 2.37, to decrease the RC delay we can reduce metal resistivity (ρ), reduce the length of the metal, increase the distance between two metal lines, increase the thickness of dielectric, and reduce the dielectric constant (ε) of the ILD [25].

Therefore, using low-k materials as ILD will reduce the parasitic capacitance and so it will decrease RC delay, and improve the operating speed of ICs.

In summary, It is very important to decrease signal delay and cross-talk in interconnects within integrated circuits as device dimensions decrease. And this motivates the need for lower resistivity metals and lower dielectric constant insulating films in electrical connections to meet future goals.

2. 7.3 Why do we need low-k dielectrics in optical interconnects?

In fact, using electrical interconnects in ICs doesn't meet the future goals such as an increasing signal bandwidth demand. . The main advantages of optical interconnects compared with electrical interconnects are lower signal attenuation, lower dispersion, and lower crosstalk leading to superior bandwidth-distance products. Another significant advantage of the optical

links is the immunity of the signal's transmission to electromagnetic interference, which makes them very well suited to mobile systems [23, 24, and 25].

However, Optical interconnects have higher costs than electrical interconnects. As a result, the next generation of optical components needs to be low cost and compatible with high volume manufacturing. So, to achieve this requirement we need to increase the integration on optical devices [23, 24].

The main important components for simultaneous manufacturing of electronics and optics function on the same chip using CMOS process are optical waveguides. This implementation will increase the number of components integrated on the same chip and fulfils Moore's law. So this means that the size will keep decreasing, and so increasing the interconnect parasitic capacitance [23, 24].

Although, using low k-dielectrics in designing optical waveguides may increase the scattering losses, but, to integrate so many components on the same chip, optical waveguide designs with thin claddings and small bending radii are desired. A thin cladding would allow small inter-waveguide spacing for a given amount of cross-talk. Such waveguide designs imply fabrication of waveguides with a high refractive index contrast between the core and the cladding. These high refractive index contrast systems could be used for high density on-chip optical waveguides to replace the current electrical interconnects

Low-dielectrics can be used as low-refractive index cladding materials in optical waveguides [25]. Optical waveguides with low-k dielectrics cladding have high refractive index contrast, which might be a good point to increase the optical confinement inside the waveguide. We can improve the optical properties of low-k dielectrics to get highly transparent materials and increase the chance of using it as a lower cladding for a low-loss optical waveguide. However,

using low-k dielectrics in designing optical waveguides might increase both volume and surface scattering loss. In chapter 5, we will discuss the use of low-k dielectrics in designing optical waveguides in more details.

2.7.4 Preparation methods of porous silica

Porous silica is one of the most important low-k dielectrics that are widely used in optical and electrical applications. The focus of this research work was on using porous silica as lower cladding in optical waveguides. Therefore, in this section we will include the main methods that are used to prepare porous silica.

2.7.4.1 Electrochemical anodizing method

Since the first studies of porous silicon in 1950s, the main process that has been used to obtain nano-crystalline porous silicon NPS is the electrochemical dissolution of silicon wafers based on hydrofluoric HF solution. As Ma.Concepción Arenas et al. [56] observed, "This process consists of applying an anodic current to the silicon wafer in an HF electrolyte contained in a Teflon cell, which is composed of a silicon working electrode and a Pt counter electrode. The dissolution of silicon requires holes supplied from its valence band at its surface; thus, for n-type silicon, light is necessary to photogenerate holes in contrast to p-type silicon. A constant current density can adjust the porosity, thickness, uniformity and reproducibility of samples. Ethanol is added to the HF electrolyte to counteract the hydrophobic character of silicon and facilitate the infiltration of HF inside the pores. In addition, ethanol helps to remove the hydrogen bubbles generated during pore formation on the silicon surface ".

Hoseinzadeh et al. [55] describes the preparation of multilayer planar waveguide structures by electrochemically anodizing p-type silicon with 0.98 - 1.1 Ω-cm resistivity in an electrolyte mixture composed of 40 % hydrofluoric acid and ethanol (1:1). Current densities were varied between 25 to 40 mA/cm^2 and anodization time between 10 to 20 minutes. Then, thermal oxidation of the structures was performed in a furnace in order to extend guiding region into the visible range. In the process, firstly samples were oxidized at 300 °C for 1 hour in dry O_2 to stabilize the porous material against the heat treatment at higher temperatures, then oxidation at 1000 °C for 25 minutes was performed in wet O_2, and finally the samples were oxidized at 1100 °C for 1 hour in dry O_2 to make oxidized multilayer planar PS waveguides (OPSWG). Table 2.2 shows the refractive index and porosity of porous and oxidized porous silicon (OPS) layers. The table results show that the porosity and refractive index of porous silicon decrease after oxidation.

Table 2.2: Refractive index of porous layers before (n) and after (n´) oxidation. P and P´ are porosities before and after oxidation, respectively.

J (mA/cm^2)	t (min)	P (%)	n	P´ (%)	n´
25	10	45	2.5	17.5	1.38
30	10	59	1.99	38.5	1.28
35	10	73	1.46	59.5	1.18
40	10	80	1.35	70	1.13
25	20	65	1.79	47.5	1.23
30	20	74	1.5	61	1.17
35	20	75	1.48	62.5	1.16
40	20	82	1.3	73	1.12

2.7.4.2 Ambient drying method

The ambient drying technique was developed by Nitta et al. [52]. The porosity was changed by varying the existence of silyation (surface modification), the aging time, or the initial water/saline ratio. Silyation is a pre-drying surface modification; it helps in eliminating band moisture in these films and makes them hydrophobic. Sols containing a relatively non-volatile solvent (ethylene glycol) were spun in an open, ambient environment. The final porosity of the films was controlled using the initial TEOS/glycol ratio. The thickness, the porosity, and the dielectric constant of the ambient dried silica xerogel films were affected by the glycol content of the film, the drying temperature, the spin speed and the spin time. Thicker films are desired to get accurate characteristic of mechanical properties by nano-indentation. This process is cheap, simple and fast. Faster gelling and thicker films (1.4-2.6) um of 40% porosity for a spin speed of (2000) rpm can be achieved by using ethylene glycol. Porous silica prepared by the ambient drying process and deposited using a spin coating procedure can be considered as a very good low-k dielectric because of their high thermal stability and their ability to be rendered hydrophobic. **Fig. 2.14** shows high resolution SEM fracture images of a xerogel film that is 78% porous. The film is composed of a collection of bonded particles that are largely spherical in shape. Analyzing the SEM pictures shows that the average pore size is in a range between 10 and 20 nm and that the average particle size is also about 20 nm.

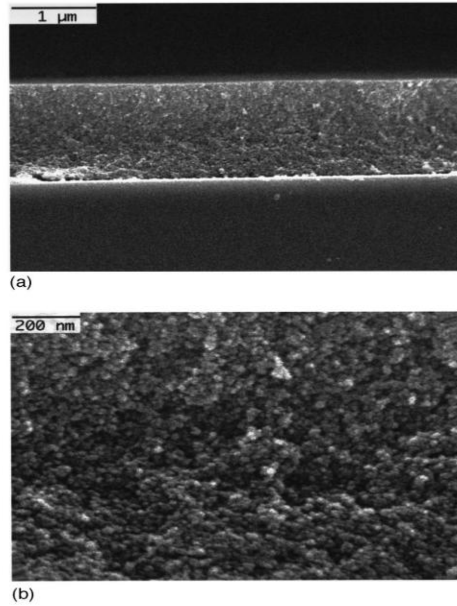

Figure 2.14: Cross-sectional, fracture SEMs of 78% porous xerogel film ;(a) Magnification: 25 000x; (b) magnification: 100 000x. **Reproduced from [52]**

2.7.5 Effective medium models for the refractive index of porous material

Effective medium theory describes the effective refractive index of a porous material as a function of the refractive index of the host medium $n_h=n_{Silica}$ in our case, and that of the embedded material with $n_{emb}=n_{pore}=1$ for vacuum. Furthermore, the porosity P as well as the topology of the porous structure affects n_{avg}. I use average refractive index n_{avg} to define the effective refractive index of porous material to avoid confusion with the effective refractive index of the waveguide.

The three most frequently used effective medium models are the Bruggeman approximation [57], the Looyenga formula [58], and the Maxwell Garnett mixing rule [59].

The Bruggeman approximation is defined as in the following equation:

$P\frac{n_{pore}^2 - n_{avg}^2}{n_{pore}^2 + 2n_{avg}^2} + (1 - P)\frac{n_h^2 - n_{avg}^2}{n_h^2 + 2n_{avg}^2} = 0$, this model is adequate for irregularly shaped particles and low porosities.

The Looyenga model:

$n_{avg}^{2/3} = (1-P)\, n_h^{\frac{2}{3}} + P n_{pore}^{\frac{2}{3}}$, this model is suitable for high and low porosities.

The Maxwell Garnett formula:

$\frac{n_{pore}^2 - n_{avg}^2}{2n_{pore}^2 + n_{avg}^2} + (1 - P)\, \frac{n_h^2 - n_{avg}^2}{n_h^2 + 2n_{avg}^2} = 0$, this is used for high porosities

Finally, the simple linear interpolation

$n_{avg} = (1-P)\, n_h + P n_{pore}$ should be mentioned.

For porosities $P<30\%$ and a wavelength between 300 and 1500 nm, this linear calculation deviates only 3% from the Bruggeman formula and 10% from the Looyenga model, whereas the deviation from the Maxwell Garnett model is 74%. Thus, when restricting to porosities below 30%, the simple interpolation might be used instead of the more complicated Bruggeman or Looyenga expressions. The reason for the linear approximation was described by Gehr et al.[61] , when the porosity is very small that means the pores occupy small fraction from the whole volume. Therefore, based on the assumptions that the porous material has two mediums the electric field within each constituent is uniform and that the nonlinearity makes only a small contribution to the refractive index, and they include similar description for effective dielectric constant depending on the porosity.

Assuming that Looyenge model can be used for all types of porosities I used it to define n_{avg} of porous silica waveguide.

2.8 Optical waveguides modeling

2.8.2 Full-Vector Finite Difference Modesolver

An optical waveguide modesolver is one of the most important tools that are used in designing optical circuits. It was first described by Fallahkhair et al. [54] and it was considered

as the main simulation tool for modeling optical waveguides. It calculates modal solutions to Maxwell’s equations in a very short time. Furthermore, it is not only used for simulating infinite planar waveguides, but it also enables simulation of ridge waveguides.

The full-vector finite difference modesolver can be considered as an accurate tool for modeling the LEAC chip and was used to optimize waveguide dimensions for all upper cladding sensing environments. This in turn, allows waveguide dimensions to be chosen. Using a modesolver we can do a round of simulations for different dimensions to decide the best optimization of the waveguide's dimensions that we can use to support a single mode for the waveguide and allow a sufficient amount of optical power to reach the sensing region. Using a mode solver we can decide the thickness of the lower cladding, the waveguide width and the core thickness that can be used to design a low-loss optical waveguide. For example, from the simulation results of the modesolver we can see that the coupling loss decreases exponentially by increasing the cladding thickness.

Furthermore, experimental results have been found to be in excellent agreement with modesolver predictions in many research works. In my work I added two models to calculate scattering loss to the modesolver code. The goal to use those two features was to calculate both surface and volume scattering loss in optical waveguides. Those two features can be applied on both normal dielectric and low-k dielectric waveguides. However, In case of normal dielectric waveguides we assume zero porosity i.e. zero volume scattering loss. More discussion about surface scattering and volume scattering models will be shown in Chapter 3.

References

[1] Robert Pownall, Guangwei Yuan, Tom W. Chen, Phil Nikkel, and Kevin L.Lear, Member, " Geometry Dependence of CMOS-Compatible, Polysilicon, Leaky-Mode Photodetectors", IEEE Photonics technology Letters, APRIL 1, 2007.

[2] Yan, Rongjin, Santano P. Mestas, Guangwei Yuan, Rashid Safaisini, and Kevin L. Lear, "Response of local evanescent array-coupled biosensors to organic nanofilms." Selected Topics in Quantum Electronics, IEEE Journal of 15, no. 5 (2009): 1469-1477.

[3] G. Yuan, M.D. Stephens, D.S. Dandy, J.K. Gerding,A, Van Orden and K.L. Lear, " Local evanescent, array coupled (LEAC) biosensor response to low index adlayers", 2006 Optical Society of America.

[4] Guangwei Yuan, Matt Stephens, David S. Dandy, Ahmad N. AL-Omari , and Kevin L. Lear, "Implementation of buried detector arrays for waveguide sensors" , 0-7803-9556-5/06/$20.00 © 2006 IEEE, Fort Collins, CO 80523 USA.

[5] T. Erickson and K. Lear, "Optimization of the Local Evanescent Array-Coupled Optoelectronic Sensing Chip for Enhanced, Portable, Real-Time Sensing," Sensors Journal, IEEE , vol.13, no.5, pp.1905,1913, May 2013.

[6] Rongjin Yan, "A CMOS compatible optical biosensing system based on local evanescent field shift mechanism", Ph.D. dissertation Dept. Electrical and Computer. Eng. , Colorado State University Fort Collins, Colorado Fall 2011.

[7] Andrew Armstrong ,John Blatt,Justin Grantham ,Dan Higley ,Kelli Luginbuhl ,Kelly Nienburg , " Lab-on-a-Chip Diagnostic Biosensor", ECE402 report, Dept. Electrical and Computer. Eng. , Colorado State University Fort Collins, Colorado Spring Semester 2011 .

[8] Timothy Erickson, "Design optimization and fabrication of an integrated optoelectronic sensing chip for applications in real-time biosensing and groundwater contaminant detection", Ph.D. dissertation, Dept. Electrical and Computer. Eng., Colorado State University Fort Collins, Colorado Summer 2014.

[9] Yan, Rongjin, et al. "Detection of virus-like nanoparticles via scattering using a chip-scale optical biosensor." Applied Physics Letters 101.16 (2012): 161111-161111

[10] Prof. Graham T. Reed,G. Mashanovich, M. Milosevic, and F. Gardes , "Silicon Photonics Waveguides" , Lecture, University of Surrey, Guildford, UK ,(Silicon Photonics –PhD course prepared within FP7-224312 Helios project).

[11] Jia-Ming Liu, " Photonic Devices", Chapter 3, Cambridge, New York, Melbourne, Madrid, Cape Town, Singapore, São Paulo, 2005, pp. 119-163

[12] Jia-Ming Liu, “Photonic Devices,” Chapter 2, Cambridge, New York, Melbourne, Madrid, Cape Town, Singapore, São Paulo, 2005, pp. 73-117 .

[13] Jon Øyvind Kjellman, Master of Science in Electronics, Supervisor: Jostein Grepstad, IET, “Fabrication and characterization of optical waveguide components in epitaxial (Pb,La)(Zr,Ti)O3 thin films", MS.Thesis , Norwegian University of Science and Technology Department of Electronics and Telecommunications, June 2009 ,

[14] Sorab K.Ghandhi,"Etching and Cleaning," in VLSI fabrication principles, Silicon and Gallium Arsenide ", 2nd ed, Troy, New York, Chapter 9, pp.475

[15] G. Yuan; K. Lear, M. Stephens, and D. Dandy, “Initial demonstration of a local, evanescent, array coupled biosensor concept,” *Sensors*, 2005 IEEE, Oct. 30 2005-Nov. 3 2005.

[16] G. Yuan, M.D. Stephens, D.S. Dandy, J.K. Gerding,A, Van Orden and K.L. Lear, " Local evanescent, array coupled (LEAC) biosensor response to low index adlayers",2006 Optical Society of America.

[17] R. Yan, G. Yuan, M. Stephens, X. He, C. Henry, D. Dandy and K. Lear, “Evanescent field response to immunoassay layer thickness on planar waveguides,” *Appl. Phys. Letters*, 2008, 93, 101110.

[18] Guangwei Yuan, Matt Stephens, David S. Dandy, Ahmad N. AL-Omari , and Kevin L. Lear,
"Implementation of buried detector arrays for waveguide sensors', 0-7803-9556-5/06/$20.00 © 2006 IEEE

[19] R. Yan, S.P. Mestas, G. Yuan, R. Safaisini, D.S. Dandy, and K.L. Lear, “Label-free silicon photonic biosensor system with integrated detector array,” Lab on a Chip, vol. 9, 2009, pp. 2163-2168.

[20] Rongjin Yan, Student Member, IEEE, Santano P. Mestas, Student Member, IEEE, Guangwei Yuan, Rashid Safaisini, Student Member, IEEE, and Kevin L. Lear, Member, IEEE, " Response of Local Evanescent Array-Coupled Biosensors to Organic Nanofilms", IEEE Journal of selected topics in quantum electronics , September/October 2009.

[21] R. Yan, N. Lynn, L. Kingry, Z. Yi, R. Slayden, D. Dandy, and K. Lear, “Waveguide biosensor with integrated detector array for tuberculosis sensing,” Appl. Phys. Letters, 2011, 98, 013702.

[22] Yan, Rongjin, et al. "Detection of virus-like nanoparticles via scattering using a chip-scale optical biosensor." Applied Physics Letters 101.16 (2012): 161111-161111

[23]Christophe Kopp, Stephane Bernabe, Badhise Ben Bakir, Jean-Marc Fedeli, Regis Orobtchouk, ´Franz Schrank, Henri Porte, Lars Zimmermann, and Tolga Tekin, " Silicon

Photonic Circuits: On-CMOS Integration, Fiber Optical Coupling, and Packaging", IEEE Journal of selected topics in quantum electronics , May/June 2011.

[24] A. Jain , S. Rogojevic, S. Ponoth , N. Agarwal , I. Matthew , W.N. Gill , P. Persans , M.Tomozawa , J.L. Plawsky , E. Simonyi ,"Porous silica materials as low-k dielectrics for electronic and optical interconnects", Elsevier Science, Thin Solid Films 398 – 399 (2001) 513–522

[25] Xie Jielin, "Study of TMCTS Based PECVD Carbon-Doped Low Dielectric Constant Material", MS thesis, department of physics, national university of Singapore, 2004.

[26] Graham T. Reed, Andrew P. Knights , "Silicon-on-Insulator (SOI) Photonics" In Silicon Photonics (An Introduction), 2004 John Wiley & Sons, Ltd ISBN: 0-470-87034-6, ch.4,sec.4.6.1, pp.(71-77)

[27] Ming-Chang Lee, lecture, "waveguide loss", in a class of Integrated Photonic Devices.

[28] Pieter Dumon, Wim Bogaerts, Vincent Wiaux, Johan Wouters, Stephan Beckx, Joris Van Campenhout, Dirk Taillaert, Bert Luyssaert, Peter Bienstman, Dries Van Thourhout, and Roel Baets, " Low-Loss SOI Photonic Wires and Ring Resonators Fabricated With Deep UV Lithography", IEEE Photonics Technology Letters, Vol. 16, NO. 5, May 2004

[29] Shaowu Chen, Qingfeng Yan, Qingyang Xu, Zhongchao Fan, Jingwei Liu, "Optical waveguide propagation loss measurement using multiple reflections method", State Key Laboratory on Integrated Optoelectronics, Institute of Semiconductors, Chinese Academy of Sciences,No. Jia 35, Qinghua East Road, Beijing 100083, China, 15 June 2005.

[30] Yurii A. Vlasov and Sharee J. McNab, "Losses in single-mode silicon-on-insulator strip waveguides and bends", IBM T.J. Watson Research Center, Yorktown Heights, NY 10536 yvlasov@us.ibm.com

[31] Thanh-Nam Nguyen, Kevin Lengle, Monique Thual, Philippe Rochard,Mathilde Gay, Laurent Bramerie, Stefania Malaguti, Gaetano Bellanca, Sy Dat Le, Thierry Chartier, " A non-destructive method to measure coupling and propagation losses in optical guided structures", Vol. 29, No. 12 / December 2012 / J. Opt. Soc. Am. B. © 2012 Optical Society of America. OCIS codes: 060.2310, 130.2790, 120.3940.

[32] Kazuo Kasaya, Yuzo Yoshikuni, Hiroyuki Ishii, IEEE Photon. Technol. Lett. 8 (2) (1996) 251.

[33] Kevin K. Lee, Desmond R. Lim, Hsin-Chiao Luan, Anuradha Agarwal, James Foresi, and Lionel C. Kimerling, " Effect of size and roughness on light transmission in a Si/SiO2 waveguide: Experiments and model", Applied physics letters 77, 1617 (2000); DOI: 10.1063/1.1308532

[34] F. P. PAYNE, J. P. R. LACEY," A theoretical analysis of scattering loss from

planar optical waveguides", Cambridge University Engineering Department, Trumpington Street, Cambridge CB2 1PZ, UK , 26 November 1993.

[35] D. Marcuse, Bell Syst. Tech. J. 48, 3187 ~1969!.

[36] http://optiwave.com/products/component-design/optifdtd/optical-fdtd/

[37] Frédéric Grillot, Laurent Vivien, Suzanne Laval, and Eric Cassan, "Propagation Loss in Single-Mode Ultrasmall Square Silicon-on-Insulator Optical Waveguides", Journal of Light Wave Technology, vol. 24, NO. 2, February 2006

[38] Rajeev J. Ram, "Waveguide Confinement", lecture, Massachusetts Institute of Technology, Electrical Engineering, Semiconductor Optoelectronics, March 2002

[39] http://en.wikipedia.org/wiki/Ray_(optics)

[40] G. Lerondel, R. Romestain, F. Madeore, F. Muller, "Thin Solid Films", Appendix 3, 276 (1996) 80.

[41] Stephen Beaudoin, Shaun Graham, Ravi Jaiswal, Caitlin Kilroy, Brum Soo Kim, Gautam Kumar, and Shanna Smith , "An Update on Low-k Dielectrics", The Electrochemical Society Interface, Summer 2005.

[42] http://www.foothill-instruments.com/AP01.htm

[43] Rebeca C. Diaz, "Low-*k* Dielectrics: Materials and Process Technology" , EE 518, Penn State ,Instructor: Dr. J. Ruzyllo April 13, 2006. (http://wenku.baidu.com/view/bcf547ee172ded630b1cb63d.html)

[44] J. W. Fleming and D. L. Wood," Refractive index dispersion and related properties in fluorine doped silica", Applied optics / Vol. 22, No. 19 / 1 October 1983.

[45] Licheng M. Han, Ji-Sheng Pan, Shou-Mian Chen, N. Balasubramanian, Jianou Shi,Ling Soon Wong,and P. D. Foo," Characterization of Carbon-Doped SiO2 Low k Thin Films : Preparation by Plasma-Enhanced Chemical Vapor Deposition from Tetramethylsilane" , Journal. Electrochem. Soc. 2001volume 148, issue 7, F148-F153, [DOI: 10.1149/1.1375797]

[46] Alex Lim Ying Kiat , "Carbon Doped Silicon Dioxide Low k Dielectric Material", M.S.thesis University of Sains Malaysia, 2004 . URL: http://eprints.usm.my/id/eprint/3087.

[47] Chang-Chung Yang and Wen-Chang Chen, "The structures and properties of silsesquioxane (HSQ) films produced by thermal curing **, J**. Mater. Chem.**,** 2002, 12, 1138-1141, [DOI**:**10.1039/B107697N], First published online 22 Feb 2002 .

[48] Min K. Yang ,Roger H. French ,DuPont Co. Central Research ,Experimental Station ,Wilmington, Delaware 19880-0400,Edward W. Tokarsky ,DuPont Fluoropolymer Solutions ,Chestnut Run Plaza ,Wilmington, Delaware 19880-0713 , "Optical properties of Teflon® AF amorphous fluoropolymers" ,c 2008 Society of Photo-optical instrumentation Engineers. [DOI: 10.1117/1.2965541].

[49] C.E. Mohler, E.G. Landes, G.F. Meyers, BJ. Kern, K.B. Ouellette, S. Magonov, "Porosity Characterization of porous SiLK Dielectric Films", 2003, CP683, Characterization and Metrology for VLSI Technology: 2003 International Conference.

[50] Hu Yi-Fan ,FU Dan-Rong, Zhang Ying ,Zhang Fan ,Tang Ting ," Dielectric Performance of Porous Methyl Silsesquioxane /Triacety1-β-cyclodextrin Thin Films", e-Journal , Issue 10 (October 2007) , Received 21 May 2007.

[51] D. Konjhodzic, S. Schröter, and F. Marlow ,"Ultra-low refractive index mesoporous substrates for waveguide structures Received 15 March 2007, revised 23 May 2007, accepted 15 June 2007, Published online 30 October 2007 , phys. stat. sol. (a) 204, No. 11, 3676–3688 (2007) / DOI 10.1002/pssa.200776405.

[52] S. V. Nitta, V. Pisupatti, A. Jain, P. C. Wayner Jr., W. N. Gill, and J. L. Plawsky, "Surface modified spin-on xerogel films as interlayer dielectrics", Journal of Vacuum Science & Technology B 17, 205 (1999); doi: 10.1116/1.590541, Published by the AVS: Science & Technology of Materials, Interfaces, and Processing.

[53] S. V. Nitta, A. Jain, P. C. Wayner, Jr., W. N. Gill, and J. L. Plawsky, " Effect of sol rheology on the uniformity of spin-on silica xerogel films", Journal of applied physics, Isermann Department of Chemical Engineering, Rensselaer Polytechnic Institute, Troy, New York 12180, 1999.

[54] A. Fallahkhair, K. Li and T. Murphy, "Vector finite difference modesolver for anisotropic dielectric waveguides," *J. Lightwave Technol.*, 2008, 26, 1423-1431.

[55] I. Hoseinzadeh, R. S. Dariani . "Measurement of optical loss in oxidized multilayer planar porous silicon waveguides ", Optoelectronics and advanced materials-rapid communications vol.1, No. 9, September 2007, p. 471 - 476, Department of Physics, Alzahra University, Tehran, 19938, Iran

[56] Ma.Concepción Arenas, Marina Vega, Omar Martínez and Oscar H. Salinas. " Nanocrystalline Porous Silicon: Structural,Optical, Electrical and Photovoltaic Properties".

[57] D. A. G. Bruggeman, Ann. Phys. **24**, 636 (1935).

[58] H. Looyenga, Physica _Amsterdam_ **31**, 401 (1965).

[59] J. C. M. Garnett, Philos. Trans. R. Soc. London, Ser. A **203**, 385 (1904).

[60] Parastesh Pirasteh, Joël Charrier, Yannick Dumeige, Séverine Haesaert, and Pierre Joubert, "Optical loss study of porous silicon and oxidized porous silicon planar waveguides", Journal of Applied Physics **101**, 083110 (2007); DOI: 10.1063/1.2718886

[61] Russell J. Gehr, George L. Fischer, Robert W. Boyd, "Nonlinear-optical response of porous-glass-based
composite materials", J. Opt. Soc. Am. B/Vol. 14, No. 9/September 1997

Chapter 3: Modeling of scattering loss in optical waveguides

3.1 Scattering loss caused by pores (volume scattering) in porous silica

As we discussed in previous chapters, Low-k dielectric material implementation is one of the main ways that are used to allow continued scaling of microelectronic devices and fulfill Moore's law. Accordingly, if we replace the silicon dioxide with a low-k dielectric of the same thickness, this will reduce the parasitic capacitance and improve the operating speed. Also, low-k dielectric can be used as a low-refractive index material in optical waveguides which increases the refractive index contrast and thus improves the waveguide confinement.

There are different ways to implement low-k dielectrics such as adding porosity by creating large voids or pores in silicon dioxide. As we know these voids can have a dielectric constant of nearly one, thus the dielectric constant of a porous material can be reduced to values lower than two by increasing the porosity of the film.

However, using these materials in optical waveguides may raise the concern about volume scattering loss. Volume scattering is considered as a material loss and it is caused when an incident light ray encounters the scattering particles such as pores or voids. In this section we will discuss a mathematical model that can be used to calculate the volume scattering loss in porous materials such as porous silica.

Light scattering theory can be categorized in terms of two theoretical models. Both models are applied depending on the sizes of particles. One is the Rayleigh scattering theory which is applicable to small, dielectric (non-absorbing), spherical or cylindrical particles [1, 6]. The second is Mie scattering theory [7], that includes the general spherical scattering solution (absorbing or non-absorbing) without a particular limit on particle size. Mie theory can be used for describing most spherical particles scattering systems including Rayleigh scattering.

However, if Rayleigh scattering is applicable it is generally preferred because of the complexity of Mie theory.

We can define the particle size parameter as,

$$p= \frac{2\pi r}{\lambda}$$

Where r is the radius of the particle and λ is the wavelength of the incident light. When $p > 1$, the small particle approximation is not valid. Mie theory [2] should be used in this case.

Rongjin Yan stated in his dissertation [6] that Mie theory can be used for calculating the electric and magnetic fields inside and outside a spherical or cylindrical object and is generally used to calculate how much light is scattered, i.e., the total optical cross section.

However, the criteria for Rayleigh scattering is applied when the particle is much smaller than the wavelength of light ($p<1$), and then the total scattering cross section of the particle is defined by [6],

$$\sigma_{scat} = \frac{2\lambda^2}{3\pi} \, p^6 \left(\frac{n^2-1}{n^2+2}\right)^2 \qquad \text{(Eq. 3.1)}$$

Where $p= \frac{\pi R}{\lambda}$ and $R= 2r$, i.e., R is the diameter of the particle.

As shown in Eq.3.2, the scattering cross section depends on the particle size p, and the wavelength of light λ. using the formula of p as a function of R and λ, we can get

$$\sigma_{scat}= \frac{2\lambda^2}{3\pi} \left(\frac{\pi R}{\lambda}\right)^6 \left(\frac{n^2-1}{n^2+2}\right)^2 = \frac{2\pi^5 R^6}{3\lambda^4} \left(\frac{n^2-1}{n^2+2}\right)^2 \qquad \text{(Eq.3.2)},$$

Where n is the refractive index of the particle. For porous materials in general we can use the models in chapter 2 to define n.

Porosity represents a volume fraction of pores in a porous material over the total volume, it takes values from (0-1), or as we usually define it in a percentage between 0 and 100%.

Once we find the scattering cross section we can calculate the light scattering loss. I used the same model which was used to calculate scattering loss in porous Alumina in Ref. [9], where, we can define the volume scattering loss by,

$$\alpha_{vscat} = \frac{\sigma_{scat}}{volume} * P \qquad \text{(Eq.3.3)}$$

Where α_{vscat} is volume scattering loss in cm^{-1} , σ_{scat} is the scattering cross section in cm^2 , and volume is the volume of pore in cm^3.

In fact, pores in porous material might have spherical or cylindrical shapes. As a result, we will need to have different definitions for the pore volume.

Therefore, to find the volume scattering loss for spherical pores we will use the same equation above (Eq. 3.3), but the volume in this case is a sphere volume.

The volume of spherical pore can be defined as,

The volume of spherical pore= $\frac{4}{3}\pi\,(R/2)^3$, and then the volume scattering loss can be defined as,

$$\alpha_{vscat}\,(\text{dB/cm}) = 17.36 * \pi^4 \, \frac{R^3}{\lambda^4} \left(\frac{n^2 - 1}{n^2 + 2} \right)^2 * P \qquad \text{(Eq.3.4)}$$

(Eq.3.4) assumes R and λ in cm; I converted from cm^{-1} to dB/cm by multiplying by 4.34.

However, to find the volume scattering loss for cylindrical pores we will use (Eq. 3.3), but the volume in this case is a cylinder volume.

The volume of cylindrical pore can be defined as,

The volume of cylindrical pore=poreheight*π* $(R/2)^2$, then by using the (Eq. 3.4) we get,

α_{vscat} (dB/cm) =2.866* π^4 R^4 *P / (poreheight* λ^4)   (Eq.3.5)

Where R and λ are in cm

Refs. [9 and 11] stated that height of pore is << the porous layer thickness and it is in the range of 100 nm in our case.

As shown in the equations above, the scattering loss depends on the size and the density of pores and the wavelength of light. Scattering loss rapidly decreases with increasing the wavelength of light. And it rapidly increases with increasing the pore diameter.

To study the effect of the pore diameter and the wavelength of light on volume scattering, it is worthwhile to have a fast way to calculate the volume scattering for different wavelengths or different sizes. By adding the equations above to the modesolver Matlab code, we can easily find the volume scattering for any waveguide.

However, to make the code general for low-k dielectric waveguides or normal waveguides, we used a case statement with two cases. One case is to assume zero volume scattering in normal dielectrics waveguides. And the other case is to apply the equations above to calculate volume scattering in porous silica waveguides. As shown in the following part of the Matlab code,

```
% number: represents case number
mynum=input('Enter a number:');
switch mynum
    case -3 % volume scattering loss for normal dielectrics waveguide=0
        volumescatteringloss=0;

    case -2 % volume scattering loss for porous silica waveguide

figure(5)
number1 = input('Enter a number:');
switch number1

    case 1

volumescatteringloss=P*172*1000*3.14^4*((nporouseff^2-
1)/(nporouseff^2+2))^2*R^3./lambda1.^4;
fprintf(1,'volume scattering = %7.5f dB/cm\n',volumescatteringloss);
plot(lambda1,volumescatteringloss);
    case 2
```

```
        porehight=0.1;

        volumescatteringloss=P*2.866*10000*3.14^4*R^4./
(lambda1.^4*porehight);
        plot(lambda1,volumescatteringloss);

end
end
```

3.1.1 Examples of volume scattering loss calculations

To study the effect of the wavelength of light on volume scattering loss I simulated a waveguide for different values of wavelength as shown in **Fig. 3.1**. The plot shows the volume scattering loss as a function of wavelength, when the diameter of pore R=12.5 nm, P=40%, $n_{lowercladding}$=1.26, and $n_{uppercladding}$=1 assuming spherical pores.

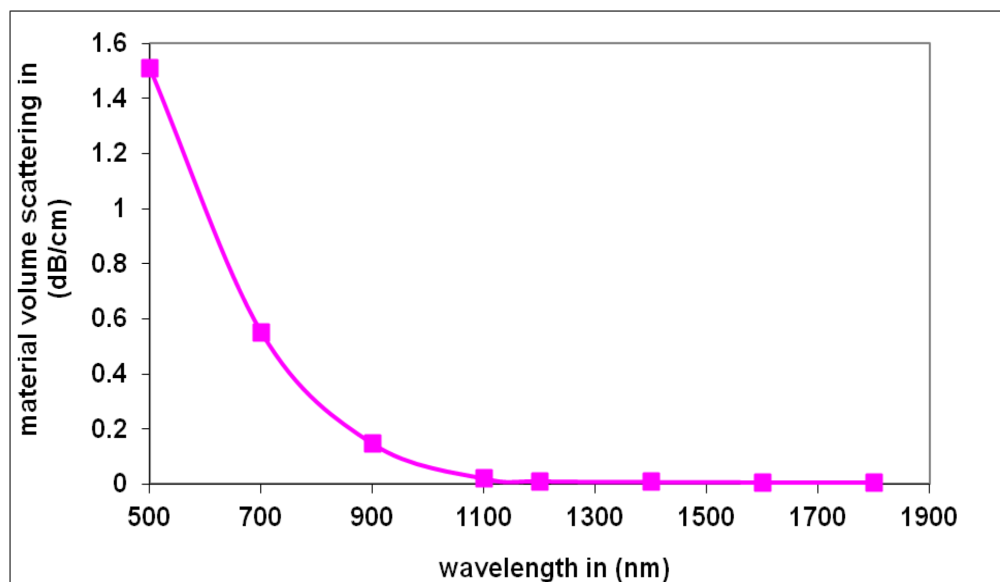

Figure 3.1: Volume scattering loss as a function of wavelength

To study the effect of the diameter of pore on volume scattering, I simulated a waveguide for different sizes of pore as shown in **Fig. 3.2**. The plot shows the volume scattering loss as a function of R for λ= (650, 830, 1300, and 1550) nm, upper cladding index=1, lower cladding index=1.26, and P=40%, assuming spherical pores. The volume scattering loss increases rapidly by increasing the pore size.

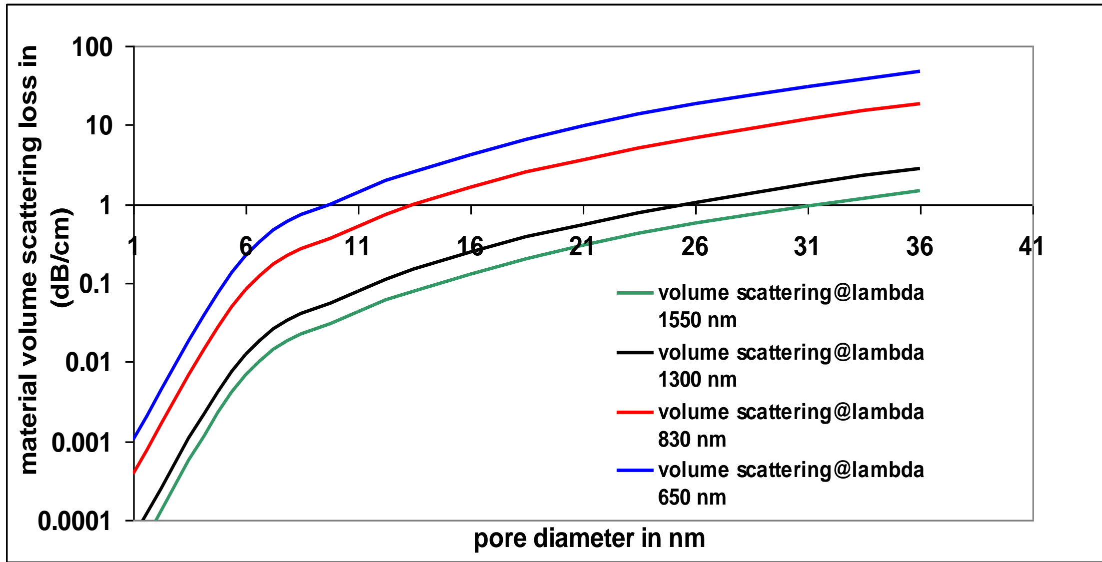

Figure 3.2: Volume scattering loss as a function of pore size

Fig. 3.3 shows the material volume scattering loss as a function of wavelength, when R=17.5 nm, P=40%, and $n_{uppercladding}$=1, and $n_{lowercladdingt}$=1.45, porehight=100 nm, assuming cylindrical pores.

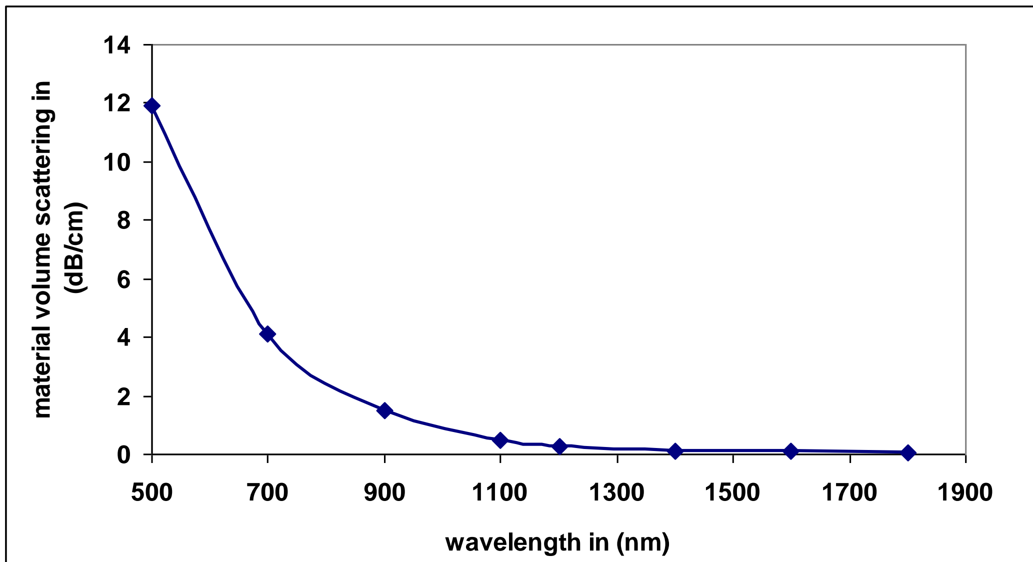

Figure 3.3: Volume scattering loss as a function of wavelength

3.2 Surface scattering loss model for optical waveguides

Surface scattering loss depends on the root mean square (rms) deviation of the planarity at guiding layer interfaces (σ). Interface scattering has been modeled by many authors, but a reasonably accurate and attractively simple model was produced by Tien **Eq. 3.6** [2 and 5].

$$\alpha_s = \frac{\cos^3\theta_1}{2\sin\theta_1}\left(\frac{4\pi n_1(\sigma_u^{\ 2}+\sigma_l^{\ 2})^{\frac{1}{2}}}{\lambda_0}\right)^2\left(\frac{1}{d+\frac{1}{k_{xu}}+\frac{1}{k_{xl}}}\right) \qquad \text{(Eq. 3.6)}$$

Where σ_u is the r.m.s. roughness for the interface between the core and upper cladding (upper waveguide interface), σ_l is the r.m.s. roughness for interface between the core and lower cladding (the lower waveguide interface), k_{xu} is the perpendicular x-directed decay constant in the upper cladding, k_{xl} is the perpendicular y-directed decay constant in the lower cladding, and h is the waveguide thickness.

We can find the decay constants using (Eq. 3.7)

$$k_{xi}^{\ 2} = \beta^2 - k_0^{\ 2} n_i^{\ 2} \qquad \text{(Eq. 3.7)}$$

Using Tien's model, we assume that the roughness (σ) is the same for both the upper cladding and core layer due to plasma etching and core and lower cladding layer interfaces [2]. I modified this model and improved the Matlab mode solver to help me to simulate the scattering loss due to surface roughness for optical waveguide.

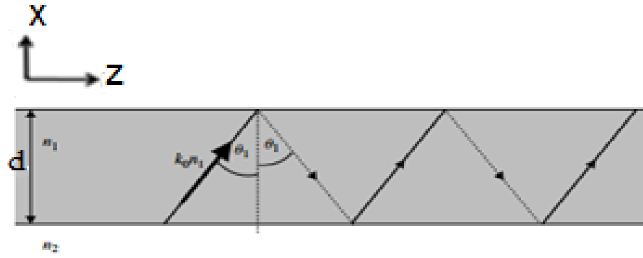

Figure 3.4: Propagation in a planar waveguide. **Reproduced from [2]**

Assuming the simplest planar optical waveguide in **Fig.3.4**, and using the relationship between propagation constants in the x, z, and propagation directions as shown in **Fig.3.5**. To find equations for $\sin\theta_1$ and $\cos\theta_1$, we can use Fig. 3.5

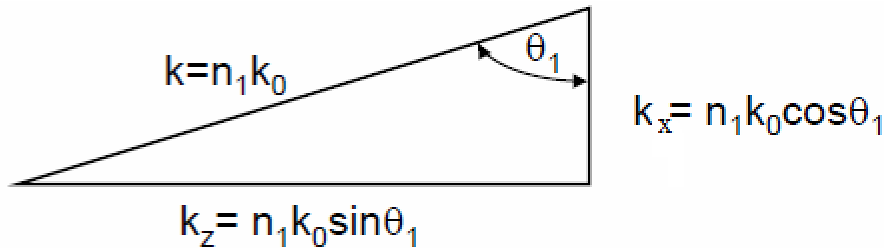

Figure 3.5: The relationship between propagation constants in the *y*, *z* and wavenormal directions. **Reproduced from [2]**

Knowing that **k** is the wavevector (propagation constant), it is related to wavelength, λ, by:

$\mathbf{k}=\dfrac{2\pi}{\lambda}$

In free space k = k_0, and k= nk_0, $\lambda = \lambda_0$, hence in free space $k_0=\dfrac{2\pi}{\lambda_0}$

From **Fig.3.5** above $\sin\theta_1=\dfrac{n_1k_0}{n_1k_0}\sin\theta_1$, where $n_1\sin\theta_1= n_{eff}$, then $\sin\theta_1=\dfrac{n_{eff}}{n_1}$, and

$\cos\theta_1=\dfrac{n_1k_0}{n_1k_0}\cos\theta_1$, where $n_1k_0\cos\theta_1=\dfrac{sqrt((n_1k_0)^2-(n_{eff}k_0)^2)}{n_1k_0}$ =sqrt (1-$\left(\dfrac{n_{eff}}{n_1}\right)^2$)

So $\beta = n_{eff} k_0$

The decay constant in the upper cladding is k_{xu}= sqrt(β^2 -$(k_0 n_3)^2$)

The decay constant in the lower cladding is k_{xl}= sqrt(β^2 -$(k_0 n_2)^2$)

To simplify the equation and use it in Matlab mode solver I assumed the following relations:

$k_{xuinv}=1/k_{xu}$

$k_{xlinv}=1/k_{xl}$

decay factor=$1/(d+k_{xuinv}+k_{xlinv})$

sigma factor=$(4*3.14*n_1*\text{sqrt}(\sigma_u^2+\sigma_l^2)/\lambda)^2$

Using the formulae above and substituting in Tien's model we can get:

$$\alpha_s(\text{dB/cm}) = 2.17*(4*3.14*n_1*\text{sqrt}(\sigma_u^2+\sigma_l^2)/\lambda)^2*1/(d+k_{xuinv}+k_{xlinv})*(1-(\frac{n_{eff}}{n_1})^2)^{1.5}/(\frac{n_{eff}}{n_1})$$

(Eq.3.8)

Pirasteh et al. [4] used this model for a roughness range of (1-50) nm. The results were in a good agreement with his experimental results of measuring scattering loss. Also, T. Reed et al. [2] stated that this model can be applied whenever the ratio $(\sigma/\lambda) < 1$.

The model shows that the scattering loss highly depends on the amount of roughness, where scattering loss has a parabolic relation with the r.m.s roughness. And this model can be applied for both normal dielectrics and low-k dielectrics waveguides. Tien et al.[2] assumed that $\sigma_u = \sigma_l$, but in case of using porous silica in lower cladding σ_u is $<< \sigma_l$.

Finally, this model can be added to the Matlab modesolver code to make the scattering loss calculations easier. As shown in the following part of Matlab code,

```
kxu=sqrt(beta^2-k0^2*n3^2);
kxl=sqrt(beta^2-k0^2*nporouseff^2);
kxuinv=1/kxu;
kxlinv=1/kxl;
decayfact=1/(d+kxuinv+kxlinv);
```

```
%segmafact=(4*3.14*n2*sqrt(segu^2+segl^2)/lambda)^2 but we assumed segu=segl;
sigmafact=(4*3.14*n2.*sqrt(2.*sigu.^2)./lambda).^2;% this one is to plot
surface scattering as a function of sigma
sigmafact1=(4*3.14*n2*sqrt(2*sigl^2)/lambda)^2;% this one is to find surface
scattering @ fixed lambda and fixed sigma
%sth is sin(propagaion angle)
sth=neff/n2;
surfacescatteringloss=0.5*4.3*10000.*sigmafact*decayfact*(1-sth^2)^1.5/sth;%
this one is to plot surface scattering as a function of sigma
surfacescatteringloss1=0.5*4.3*10000*sigmafact1*decayfact*(1-sth^2)^1.5/sth;
```

3.2.1 Examples of surface scattering loss calculations

I used this model to calculate the surface scattering losses for the waveguides made by Jain et al. [8]. To study the effect of wavelength and r.m.s roughness on surface scattering loss, I simulated the waveguides for different values of sigma at different wavelength values. **Fig. 3.6** represents the calculated surface scattering loss results for an oxide-xerogel waveguide with air as upper cladding, core index=1.45, lower cladding index=1.263(P=40%), lower cladding thickness=1.3 µm and core thickness=2 µm. The plot represents the surface scattering loss as a function of wavelength for different values of sigma.

As shown in **Fig. 3.6** the surface scattering loss decreases by increasing the wavelength, but at the same time it increases by increasing sigma. Also, we should take in consideration the effect of both the thickness and the refractive index of the core. **Eq. 3.8** shows that the surface scattering loss increases by increasing the core index and decreases by increasing the core thickness. **Fig. 3.7** shows the scattering loss results of polymer-xerogel waveguide, with air as upper cladding, the index of the lower cladding=1.263 assuming a porous silica with a porosity of 40% , the index of Alkoxysilane core=1.51, and the core thickness is 0.94 µm.

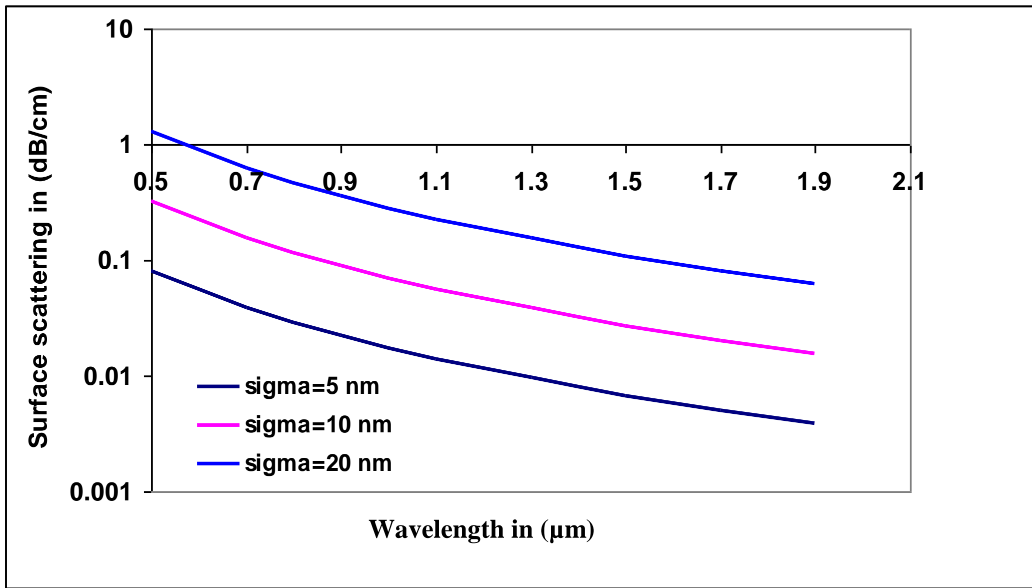

Figure 3.6: Calculated surface scattering losses as a function of the wavelength for different values of σ (rms) for oxide-xerogel waveguide of porosity= 40%(y-axis is in log-scale)

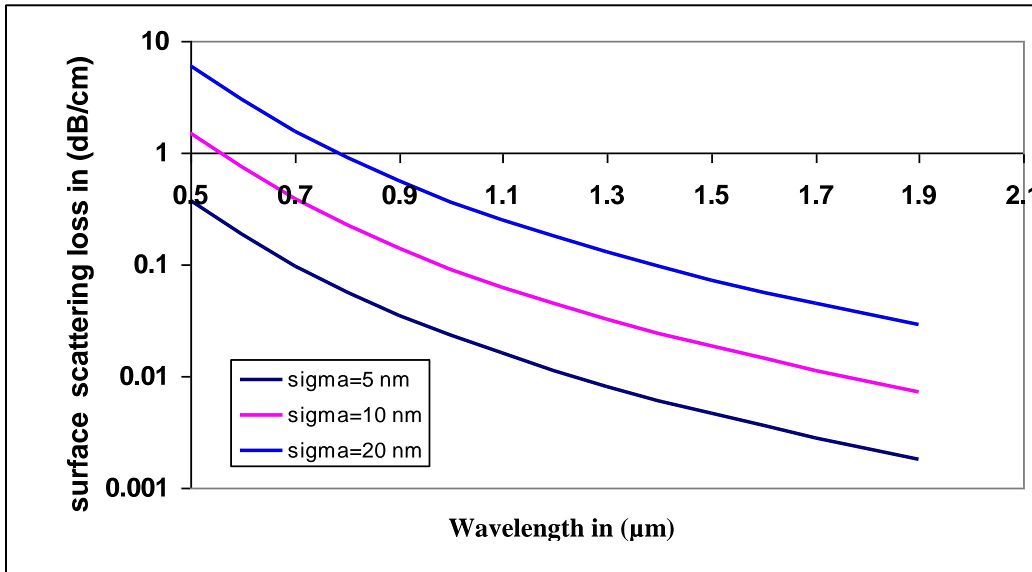

Figure 3.7: Surface scattering loss as a function of wavelength for different values of sigma(y-axis is in log-scale)

To show the effect of r.m.s roughness on surface scattering, I have simulated the surface scattering loss as a function of $(\sigma/\lambda)^2$ at λ=650 nm. **Fig. 3.8** shows a linear relation between the surface scattering loss and $(\sigma/\lambda)^2$. This linear relation is expected as we see in (Eq. 3.7).

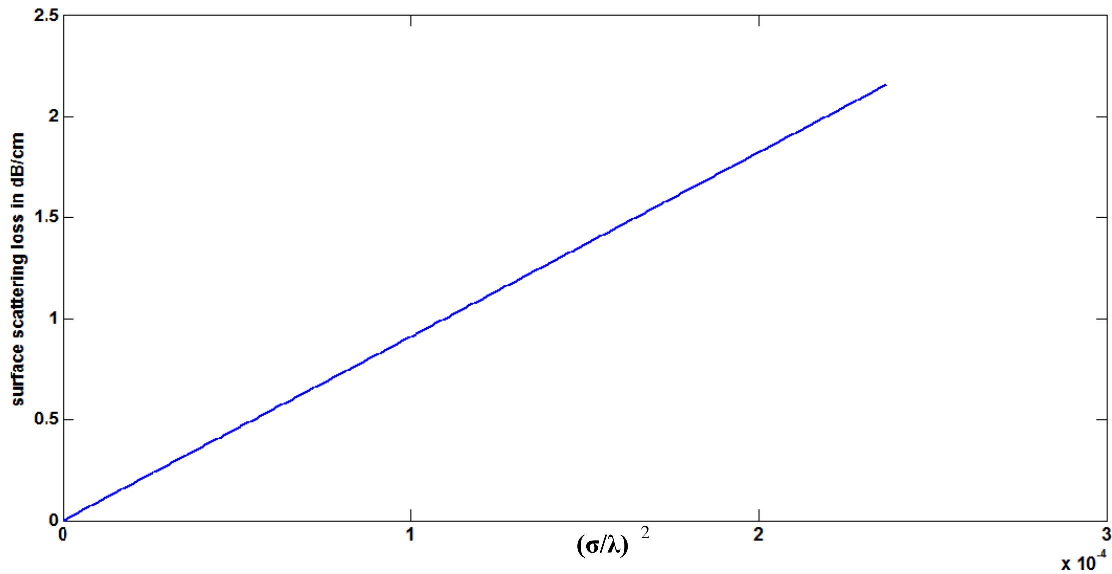

Figure 3.8: Surface scattering loss vs. $(\sigma/\lambda)^2$

References

[1] R.G.Hunsperger, "Losses in Optical Waveguides," in Integrated Optics (Theory and Technology), 4th ed. Newark,DE 19716, USA. July 1995, ch.5, sec.5.1, pp.74-77.

[2] Graham T. Reed, Andrew P. Knights , "Silicon-on-Insulator (SOI) Photonics" In Silicon Photonics (An Introduction), 2004 John Wiley & Sons, Ltd ISBN: 0-470-87034-6, ch.4,sec.4.6.1, pp.77

[3] I. Hoseinzadeh, R. S. Dariani . “Measurement of optical loss in oxidized multilayer planar porous silicon waveguides ", Optoelectronics and advanced materials-rapid communications vol.1, No. 9, September 2007, p. 471 - 476, Department of Physics, Alzahra University, Tehran, 19938, Iran

[4] Parastesh Pirasteh, Joël Charrier, Yannick Dumeige, Séverine Haesaert, and Pierre Joubert, "Optical loss study of porous silicon and oxidized porous silicon planar waveguides", Journal of Applied Physics **101**, 083110 (2007); DOI: 10.1063/1.2718886

[5] Prof. Graham T. Reed,G. Mashanovich, M. Milosevic, and F. Gardes , "Silicon Photonics Waveguides" , Lecture, University of Surrey, Guildford, UK ,(Silicon Photonics –PhD course prepared within FP7-224312 Helios project).

[6] Rongjin Yan, "A CMOS compatible optical biosensing system based on local evanescent field shift mechanism", Ph.D. dissertation Dept. Electrical and Computer. Eng. , Colorado State University Fort Collins, Colorado Fall 2011.

[7] Warren J. Wiscombe, “Mie scattering calculations: advances in technique and fast, vector-speed computer codes”, National Technical Information Service, U.S. Dept. of Commerce, 1979

[8] A. Jain , S. Rogojevic, S. Ponoth , N. Agarwal , I. Matthew , W.N. Gill , P. Persans , M.Tomozawa , J.L. Plawsky , E. Simonyi ,"Porous silica materials as low-k dielectrics for electronic and optical interconnects", Elsevier Science, Thin Solid Films 398 – 399 (2001) 513–522

[9] Rolf Apetz and Michel P. B. van Bruggen, "Transparent Alumina: A Light Scattering Model", Department of Inorganic Materials and Processing, Philips Research Eindhoven, The Netherlands

[10] Rajeev J. Ram, "Waveguide Confinement ", Lecture, Massachusetts Institute of Technology Semiconductor Optoelectronics, Electrical Engineering, (Semiconductor Optoelectronics).

[11] Kevin K. Lee, Desmond R. Lim, Hsin-Chiao Luan, Anuradha Agarwal, James Foresi, and Lionel C. Kimerling, " Effect of size and roughness on light transmission in a Si/SiO2 waveguide: Experiments and model", Department of Materials Science and Engineering, Massachusetts Institute of Technology, 77 Massachusetts Avenue, Cambridge, Massachusetts 02139, July 2000.

Chapter 4: Modeling of LEAC sensor without low-k dielectrics

4.1 Photodetector coupling loss results

I simulated the LEAC chip designed by Erickson et al. [1] at different values of core thickness and upper cladding index, and for the same range of lower cladding thickness using Matlab modesolver. **Fig. 4.1** shows my simulation results for Erickson's waveguide with n_{core}=1.8, and $n_{lower\text{-}cladding}$=1.46 in **Ref. [1].** The figure shows different coupling losses for different values of core thickness and as a result of different analyte types on upper cladding. My Result is in a good agreement with Erickson's simulation result shown in **Fig. 4.2.**

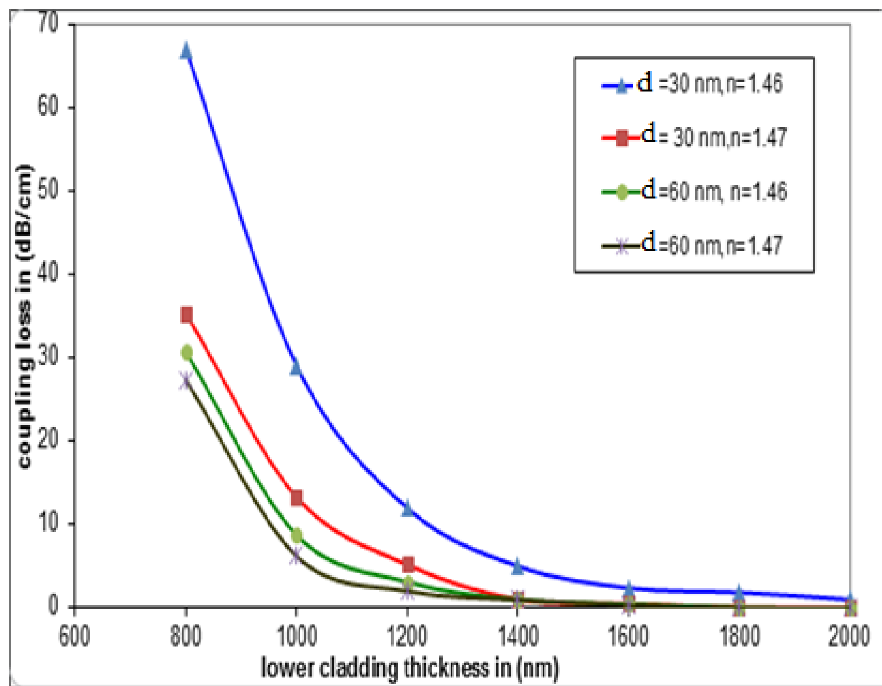

Figure 4.1: Coupling loss as a function of lower cladding thickness

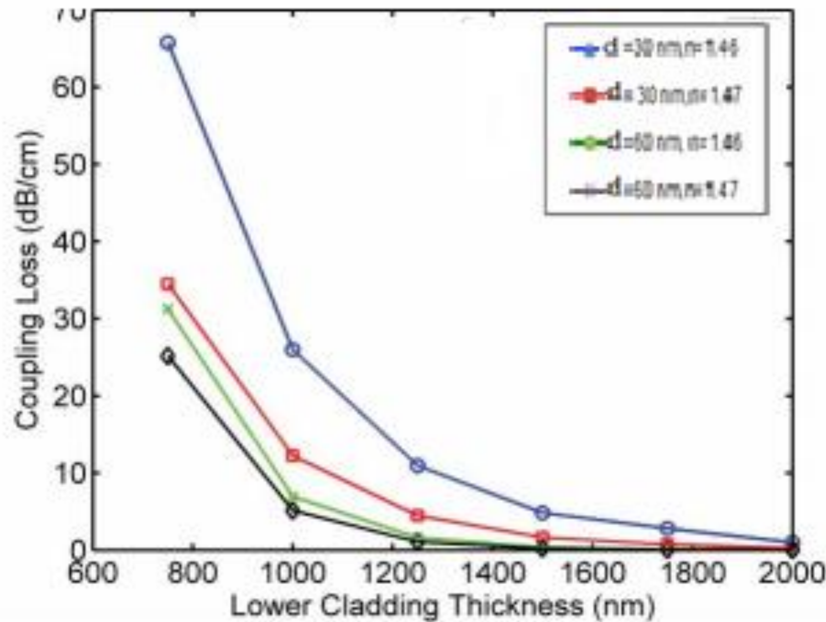

Figure 4.2: (a) Coupling loss for waveguides as a function of lower cladding thickness. **Reproduced from [1]**

As shown in **Figs. (4.1 And 4.2)**, the photodetector coupling loss decreases exponentially by increasing the lower cladding thickness. Also, the coupling loss decreases by increasing the core thickness and the refractive index of the upper cladding.

To make the comparison easier, I used the exact same range of lower cladding thickness. Both **Figs. (4.1 And 4.2)** show that the maximum values of coupling loss occur when d=30 nm and n=1.46. However, both Figs also show that the minimum values of coupling loss occur when d=60 nm and n=1.47. Also, the range of coupling loss at different values of lower cladding thickness in both Figures is approximately the same, but I guess the reason for having a little difference is due to having a different initial guess for n_{eff} in the modesolver.

4.2 Modal solutions results

I used Matlab modesolver to create modal solutions for LEAC chips designed by Erickson et al. [2] for oil sensing, BTEX sensing, and biosensing as shown in **Fig. 4.3**, the lateral lines indicate the position of the upper cladding, lower cladding, and silicon, respectively. The thin core is not visible in the image, but is located just above the line separating the upper and lower cladding regions. A description of each waveguide in **Figs. (4.3,4.4)** is provided in Table 4.1

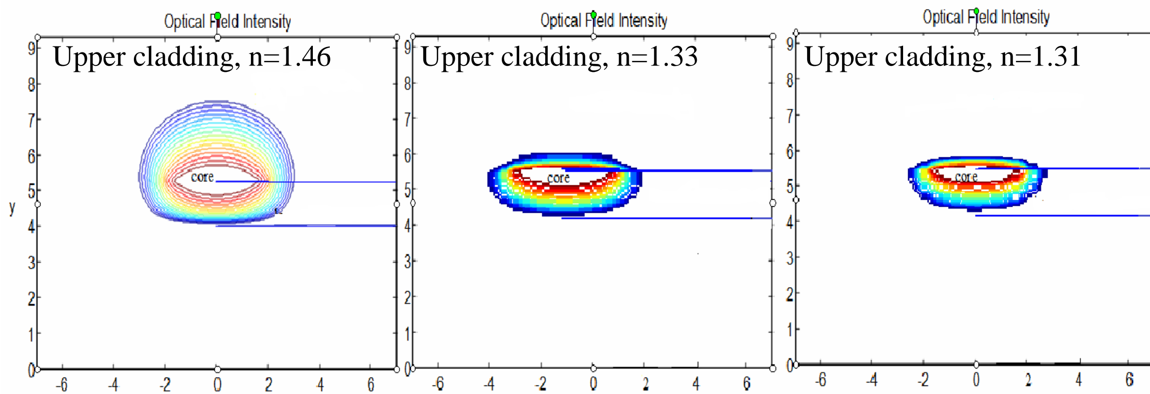

Figure 4.3: Modesolver simulation results for fundamental TE Mode of LEAC waveguides used for sensing in different upper cladding environments.

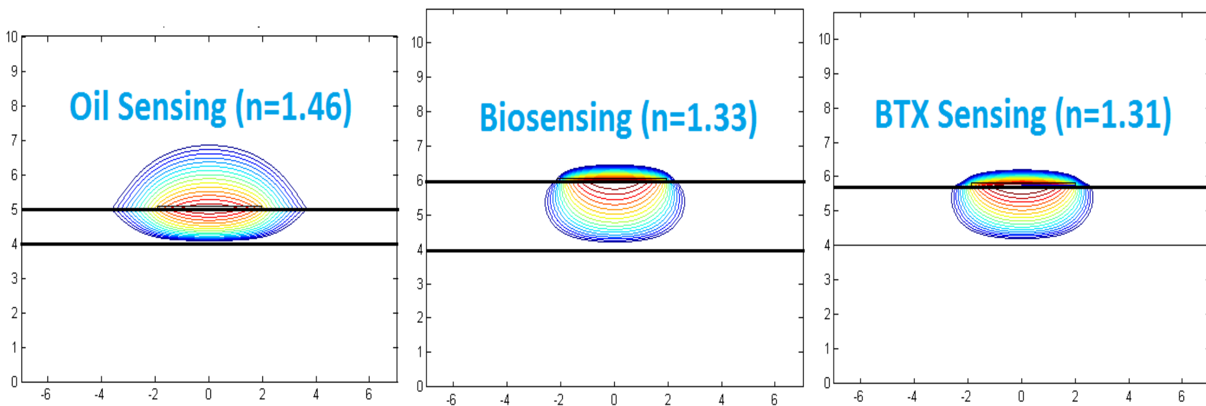

Figure 4.4: Modesolver simulation results for fundamental TE Mode of LEAC waveguides used for sensing in different upper cladding environments. **Reproduced from [2]**

The results in **Figs. (4.3 and 4.4)** show that the fraction of the field present in the upper cladding sensing region when the upper cladding has a refractive index of 1.46 is found to be much higher than the fraction of field when the upper cladding has refractive indices of 1.33 and 1.31, These results are consistent with the evanescent field shift effect. As we discussed before, when the refractive index of upper cladding increases by analyte binding this will shift the evanescent field up and reduce the amount of photodetector coupling.

4.3 Comparisons of modeling results to Erickson's modeling results for LEAC sensors

In fact to design a good LEAC sensor, the device should have high sensitivity and the photodetectors array should have high signal to noise ratio (SNR). The SNR of photodetectors is proportional to the photodetectors coupling loss. So, we have to optimize the waveguide's parameters until we get high values of sensitivity and coupling loss. However, as we stated before, there is a tradeoff between the device sensitivity and the photodetector coupling loss. For example, the sensitivity increases linearly by increasing the lower cladding thickness, but at the same time the photodetector coupling loss decreases exponentially by increasing the lower cladding thickness. To understand the dependence of sensitivity and coupling loss on the lower cladding thickness, I simulated the waveguides designed by Erickson et al.[2], using the same values, that he used.

Table 4.1 shows the comparison between the results. The table shows the results of sensitivities and coupling losses for different waveguides with different dimensions and different indices.

Table 4.1: Waveguides Used for Experiments in [2]

Upper cladding		Oil (n=1.46)	Water (n=1.33)	Teflon (n=1.31)
Waveguide width (um)		4	4	4
Lower cladding index		1.46	1.46	1.46
Lower cladding material		PECVD Oxide	Thermal Oxide	Thermal Oxide
Core material		Si Nitride	Metal Oxide	Si Nitride
Core thickness(nm)		30	37.5	70
Core index		1.8	2.05	1.8
Oxide lower cladding thickness(nm)		1250	1900	1700
Photodetector coupling (dB/cm)	Erickson's results	13	8	16
	My results	18.5	10	11.43741
% Optical Power in Upper Cladding	Erickson's results	48.6	15.2	9.8
	My results	47.802	42.5	37.822
Sensitivity (%/RIU)	Erickson's results	8880	2590	1720
	My results	8734.19	2621	1804
Effective Index (N_eff)	Erickson's results	1.461	1.4663	1.464
	My results	1.464054	1.466174	1.468984

4.4 Sensitivity as a function of lower cladding, and core thicknesses.

To find the sensitivity of the device, dM/dn which is given in units of %/refractive index unit (RIU), I used the ratio of the device modulation to the refractive index unit. The modulation ratio as we defined in chapter 2 is the fractional change in photodetector coupling from its initial value

before the analyte binding to its final value after the analyte binding, and we described that before using (Eq. 2.34). **Fig. 4.5** represents Erickson's results for coupling loss and sensitivity as a function of lower cladding thickness. To compare I simulated the same waveguide with the same dimensions and indices as shown in **Fig. 4.6.**

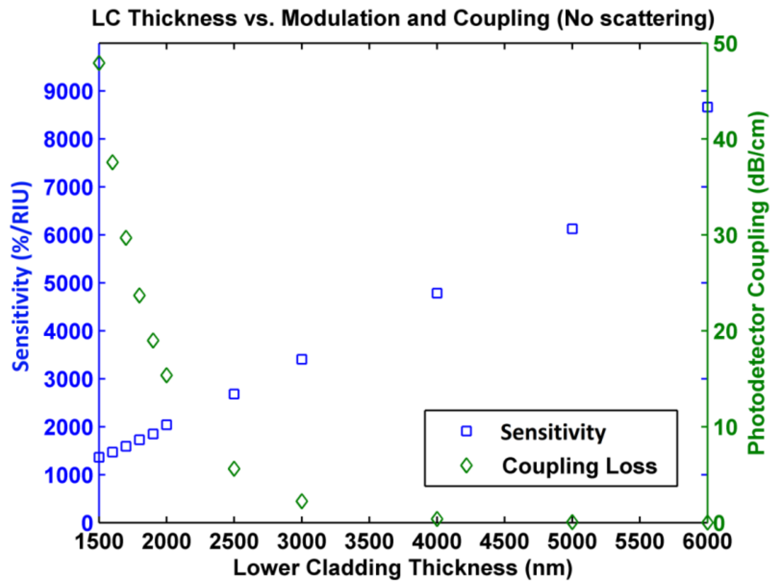

Figure 4.5: Plot of sensitivity and photodetector coupling for d=37.5 nm metal oxide core biosensing waveguide covered in Teflon Af. **Reproduced from [2]**

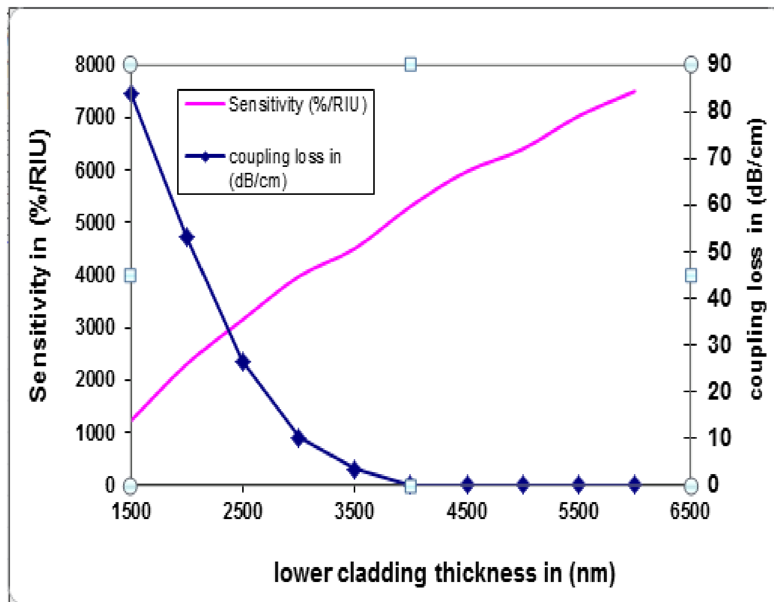

Figure 4.6: Plot of sensitivity and photodetector coupling for d=37.5 nm metal oxide core biosensing waveguide covered in Teflon Af.

Fig. 4.5 shows that the sensitivity increases linearly by increasing the lower cladding thickness. But, at the same time the coupling loss decreases exponentially by increasing the lower cladding thickness. Thus, this will affect the detected evanescent optical power, and will decrease its magnitude exponentially.

In comparison with **Fig. 4.5**, **Fig. 4.6** doesn't show exact linear relation between the sensitivity and the lower cladding thickness, but both Figures agree that the sensitivity increases by increasing the lower cladding thickness. Also, both figures show an exponentially decrease of coupling loss as a function of lower cladding thickness. But, the values are not exactly the same. I predict the reason for this difference between the results although we both used the same simulator, is due to using different guess for the effective index in modesolver. Also, I used lambda=650 nm in my simulation, but I was not sure what was the wavelength the Erickson et al. [2] used in his simulations.

Furthermore, by calculating the sensitivity for different values of core thickness, we can see that the sensitivity varies by changing the core thickness. But, we will notice that the relation to core thickness depends on the lower cladding thickness. To clarify, I use **Fig. 4.7** from Erickson's dissertation [2] to show the effect of core thickness on sensitivity. The figure shows that for smaller values of lower cladding thickness the sensitivity increases by increasing the core thickness. But, for higher values of lower cladding thickness, the sensitivity decreases by increasing the core thickness.

Also, I simulated the sensitivity for (60, 65, 70, 75) nm core thicknesses as shown in **Fig. 4.8** **t**o compare with Erickson's results.

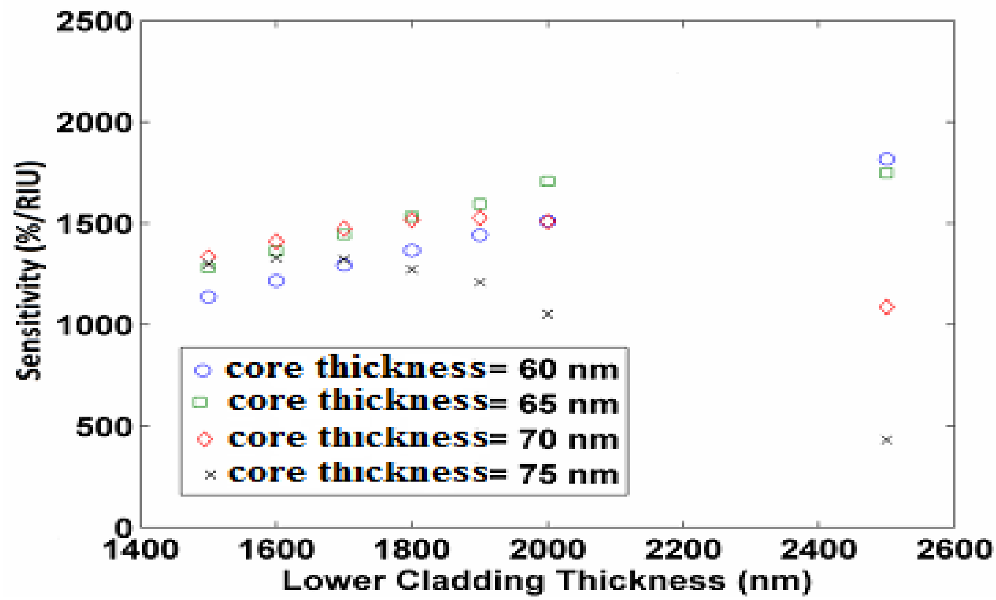

Figure 4.7: Effect of lower cladding thickness on optimal core thickness. **Reproduced from [2]**

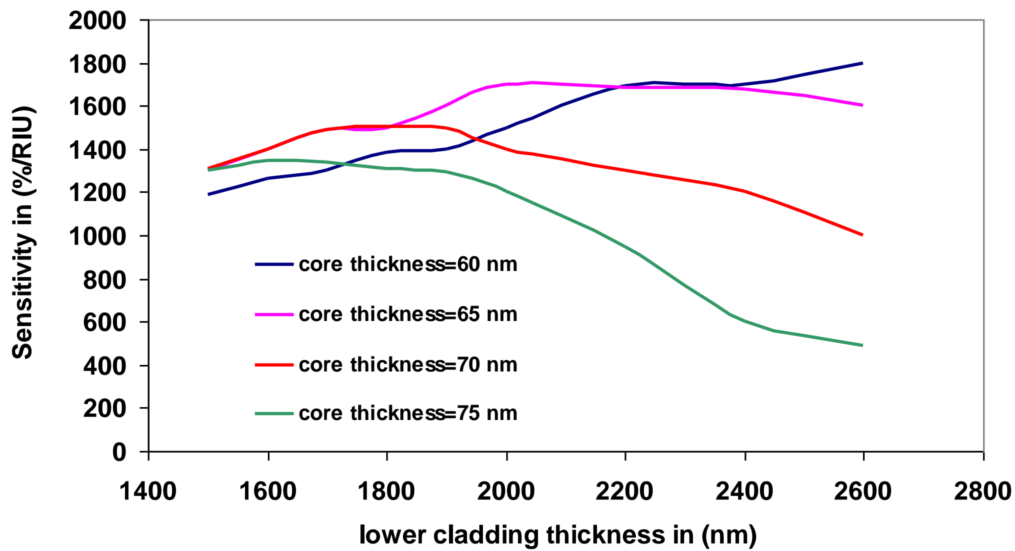

Figure 4.8: Effect of core thickness and lower cladding thickness on sensitivity

If I compare the results of sensitivity when the lower cladding thickness is 1500 nm, both figures show that the sensitivity increases by increasing the core thickness at the specified lower cladding thickness. However, if I will compare the results when the lower cladding thickness is 2600 nm, both figures show that the sensitivity decreases by increasing the core thickness at the specified lower cladding thickness. As Erickson observed in his dissertation [2], “Interestingly, modesolver results indicate that optimal sensitivity is not necessarily achieved when the waveguide core height is designed to be at cutoff. The optimum core thickness depends on the lower cladding thickness. For increasing lower cladding values, the waveguide should be designed to be at cutoff. However, for thinner lower cladding values, the waveguide should be designed to be slightly above cutoff”

4.5 Scattering loss results

The following short table shows the surface scattering loss for Erickson's waveguides using Tien's model. The values of scattering were calculated assuming the r.m.s roughness= 2 nm. This value of roughness was taken from Ref. [2].

As shown in Table 2.2 below, the upper bound of the scattering loss of Tien's model is 25.3 dB/cm is consistent with the upper bound loss estimate of Erickson et al. which was 20 dB/cm for a 7 um width waveguide.

Also, The lower bound of the scattering loss of Tien's model is 15.3525 dB/cm is consistent with the lower bound loss estimate of Erickson et al. which was 15 dB/cm for a 7 um width waveguide. These results indicate that Tien's model can be considered as a good estimate for the surface scattering loss of an optical waveguide.

Table 2.2: Surface scattering loss results

Upper cladding	Oil (n=1.46)	Water (n=1.33)	Teflon (n=1.31)
Waveguide width (um)	4	4	4
Lower cladding index	1.46	1.46	1.46
Lower cladding material	PECVD Oxide	Thermal Oxide	Thermal Oxide
Core material	Si Nitride	Metal Oxide	Si Nitride
Core thickness(nm)	30	37.5	70
Core index	1.8	2.05	1.8
Oxide lower cladding thickness(nm)	1250	1900	1700
Surface scattering loss in (dB/cm)using my model assuming r.m.s roughness=2 nm	15.35425	25.3	23.9

References

[1] T. Erickson and K. Lear, "Optimization of the Local Evanescent Array-Coupled Optoelectronic Sensing Chip for Enhanced, Portable, Real-Time Sensing," Sensors Journal, IEEE , vol.13, no.5, pp.1905,1913, May 2013.

[2] Timothy Erickson, "Design optimization and fabrication of an integrated optoelectronic sensing chip for applications in real-time biosensing and groundwater contaminant detection", Ph.D. dissertation, Dept. Electrical and Computer. Eng., Colorado State University Fort Collins, Colorado Summer 2014.

Chapter 5: Modeling of optical waveguides with porous silica claddings

5.1 Introduction

Designing optical waveguides is one of the ways that helped to improve the simultaneous manufacturing of electronics and optics which function on the same chip using a CMOS process. Highly confined optical waveguides are needed to transmit optical data in silicon photonic circuits. Using optical waveguides compared with electrical interconnects for transmitting data exhibits several demonstrated advantages, such as higher-data rate, lower signal attenuation, lower dispersion, and lower crosstalk [2].

In order to integrate so many components on one chip, the dimensions of each device need to be decreased, so, the RC-time delay will increase and this will reduce the operating speed. Therefore, one of the methods that we can use is reducing the parasitic capacitance by reducing the dielectric constant of the material used in interconnects [2, 4].

The prior research on LEAC chip used conventional silicon-dioxide dielectrics for optical waveguide cladding. However, this will reduce the ability to integrate many components on same chip, and will reduce the data rate compared to low-k dielectrics. Therefore, to enable electronics and optics to be fabricated on the same optoelectronic circuit chip, new technologies and new materials need to be developed to cope with the integration challenges.

In recent years, low-k dielectric material has been developed to replace conventional dielectric material such as SiO_2 as the interlayer dielectric (ILD) in Integrated Circuits (ICs). Using low-k dielectric material increases the ability to integrate large number of components on the same silicon wafer and satisfies Moore's law. The reason for developing low-k dielectric

material is to reduce the RC-time delay and improve the operating speed of the ICs [2].

Therefore, since low-k dielectrics have low refractive index, this also describes the need for using low-k dielectric material in designing high confinement optical waveguides used as interconnects to transmit data in silicon photonics.

5.2 Optical waveguide using low-k dielectrics porous silica

Low-k dielectrics are considered as the best choice to cope with the integration challenges and reduce the RC signal delay for performance improvement of the next generation ICs. Porous materials are one example of low-k dielectrics that can be used. Controlled porosity is the most practical way of reducing the dielectric constant of a material below 2 [12].

Fabrication of waveguides of high refractive index contrast between the core and the cladding helps to reduce the need for large bending radii and thick cladding. Thus, having a waveguide of thin cladding and small bending radius increases the ability to integrate so many components on the same chip with low crosstalk [12].

An optical waveguide of high refractive index contrast consists of a high refractive index material used as core such as TiO_2 or Ta_2O_5, and a porous material such as porous silica as low-refractive index lower cladding. Porous silica can be described as interconnected clusters of SiO_2. Assuming that we are working in the visible light range, the clusters are considered optically transparent, because the typical cluster size is 20 nm which is an order of magnitude or smaller than the wavelength of visible light [12].

The relation of the refractive index n of porous silica as a function of the volume fraction porosity p assuming low porosity can be described as: $n = 1.458-0.458P$ [12]. The refractive index that can be obtained for such a material is in the range of (1.1-1.34) which makes it a good choice to reduce the integration problems [12].

The properties of porous silica materials such as the simple preparation method, the controllable refractive index and thickness, and the ability to make it hydrophobic make it one promising material that can be used as low-refractive index lower cladding in optical waveguides. Optical waveguides of negligible absorption and scattering loss can be achieved using porous silica as lower cladding. Furthermore, the process of making porous silica is compatible with CMOS technology, which makes the integration of this interconnect strategy with microprocessors easier [12, 14].

However, it is important to study the effect of porosity on the mechanical and interfacial stability when using porous materials in optical or metallic interconnects. The porosity has a large impact on the adhesion of porous material to different neighboring layers, and on their mechanical properties such as: modulus, hardness, and toughness. In addition it has a large effect on their electrical and chemical interaction [12].

Furthermore, there is an interaction between porous materials and the adjacent layers to which they are attached. This interaction affects the performance of these structures. Therefore, as we are interested in designing optical waveguides using porous materials as lower claddings, we need to study the scattering properties of porous materials. Clearly, the existence of pores in porous materials will cause volume scattering and this scattering depends on the porosity and the size of pores. In addition, we need to consider the losses caused at the interface between the porous materials and the layers above and below them. The reason for that is, the surface of a porous material is not smooth and I predict it has large roughness and that result in non-negligible surface scattering loss

5.2.1 Optical waveguide design using porous silica as lower cladding

In this section I will discuss two designs of optical waveguides made by two different authors. The waveguides were made using porous silica as a lower cladding. I will include the experimental results of the optical waveguides and compare it with the simulation results using the Mat lab modesolver.

5.2.1.1 The optical waveguide made by Jain et al. [12]

Jain et al. [12] fabricated an asymmetric planar optical waveguide of high refractive index contrast using air as upper cladding and porous silica as lower cladding. Hydrophobic porous silica films of high thermal stability and of thickness>1 um were prepared using the ethylene glycol co-solvent for being used as a lower cladding of the optical waveguide.

Two types of high refractive index materials were used for the core of the waveguide. The first one is inorganic material of an approximately 1 um SiO_2 prepared by plasma enhancement chemical vapor deposition (PECVD) using SiH_4 and N_2O plasma.

The second one is a 2 um polymer film prepared by a spinning on Alkoxysiloxane epoxy at spinning speed of 6000 rpm for 100 s followed by a 20-min bake at 100˚C to remove the solvent. The solvent removal step causes evaporation-induced instability which results in pinhole formation. Performing the UV curing step before the solvent removal step prevents the pinhole’s formation. Thus, we can form a uniform continuous polymer film on the xerogel, and then finally annealing was done at 150˚C. Finally, polymer–xerogel waveguides with a refractive index contrast of 0.34 maximum were fabricated using an alkoxysiloxane polymer (n=1.51).

5.2.1.1. a Optical waveguide loss measurement results

Table 5.1 lists the various waveguide structures that were fabricated using a 40% porous xerogel as the lower cladding. **Fig. 5.1** shows the planar oxide-xerogel waveguide loss measured results. The results show that the oxide deposited at higher substrate temperatures gave lower absorption loss waveguides. The Figure doesn't show the results of polymer-xerogel waveguide, but Jain et al. [12] mentioned that the losses of polymer–xerogel waveguides were less than 0.5 dB/cm and this represents only absorption loss.

Table 5.1: Parameters for planar waveguides on xerogel. **Reproduced from [12]**

Core material	Core thickness (μm)	Δn	No of modes predicted/ observed
Oxide @ 150°C	0.94	0.19	2/1
Oxide @ 175°C	0.78	0.18	2/1
Oxide @ 200°C	0.94	0.19	2/1
Oxide @ 225°C	0.88	0.18	2/1
Oxide @ 250°C	0.94	0.18	2/1
Oxide @ 300°C	0.94	0.19	2/1
Alkoxysilane	2	0.23	5/3

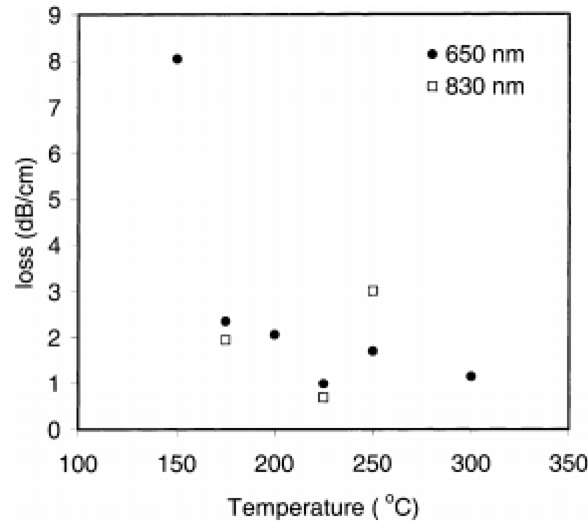

Figure 5.1: Modal loss for oxide / 40% porous xerogel planar waveguides at 650 and 830 nm. **Reproduced from [12]**

As demonstrated by Jain et al. [12], the adhesion of the oxide to the xerogel is stronger at lower deposition temperatures. This describes the negligible scattering at the air–oxide or oxide–xerogel interfaces at lower temperatures. However, the absorption loss is dominant at lower temperatures because the deposition at low- temperatures is known to lead to more unsaturated Si sites and more Si–OH sites, so the oxide films had higher absorptions.

Furthermore, Jain et al. [12] developed a polymer xerogel waveguide system. In the purely inorganic waveguides the losses were dominated by absorption losses in the oxide core and were dependent on the deposition temperature of the oxide. The oxide films deposited above 200˚C had acceptable losses for use as optical interconnect materials.

If proper attention is given to the method of preparation, silica xerogel can be considered as a good optical waveguide cladding material for on-chip optical interconnects due to the negligible absorption and scattering losses, controllable refractive index (n) and thickness, and CMOS-compatible processing.

5.2.1.1.b The simulation results of the optical waveguides

In Jain et al. [12] scattering at the air–oxide or oxide–xerogel is negligible assuming several factors. These factors include: the control of the preparation method of porous silica to improve the mechanical properties of porous silica, getting higher values of hardness and modulus using ethylene glycol as solvent, and using low deposition temperatures which makes the adhesion of the oxide to the xerogel stronger. Therefore, absorption loss at lower temperatures is considered the dominant source of loss in xerogel-oxide and xerogel-polymer optical waveguides in Jain et al. [12]

The results in this section were simulated using Matlab modesolver and a good agreement between measurement and simulation results could be achieved.

The modesolver simulation result for fundamental TE Mode of xerogel-polymer (n=1.51) optical waveguide of air as upper cladding, 1.2 um thick porous silica of 40% porosity and 20 nm pore diameter as lower cladding, and 2 um core thickness and of 4 um width at 650 nm wavelength is shown in **Fig. 5.2**, The modal loss is 0.213 dB/cm

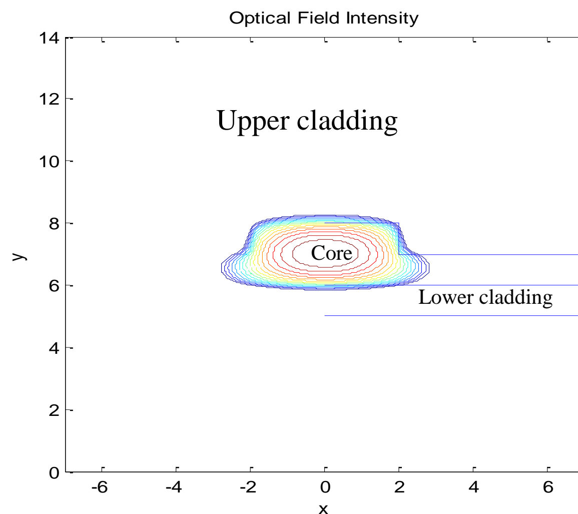

Figure 5.2: Rib xerogel-polymer waveguide

The modesolver simulation result for fundamental TE Mode of xerogel-oxide optical waveguide with 1.3 um thickness of lower cladding, 0.94 um core thickness, and of 4 um width at 650 nm wavelength is shown in **Fig.5.3**, the modal loss is 2.065 dB/cm.

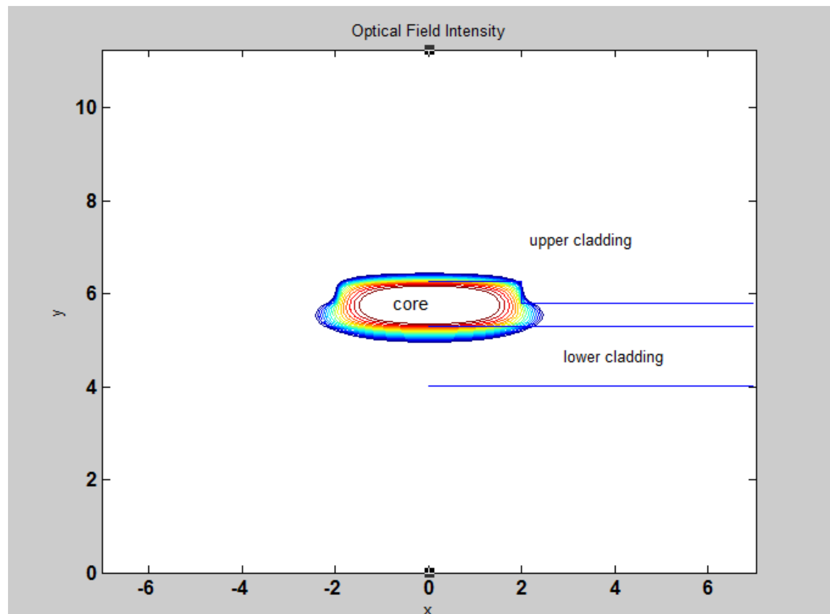

Figure 5.3: Xerogel-oxide rib waveguide

To be able to compare the simulation results with the measured results, it is worthwhile to find the total modal loss and compare the results with **Fig. 5.1**. Hence; **Fig. 5.4** shows the simulated modal loss as a function of wavelength. The value of simulated modal loss at λ= 650 nm is 2.06529 dB/cm and this result is in a good agreement with the measured modal loss of~2.3 dB/cm. Also, the figure shows that the simulated result of the total modal loss at λ= 830 nm is 1.6 dB/cm which is close to the measured modal loss of ~1.9 dB/cm

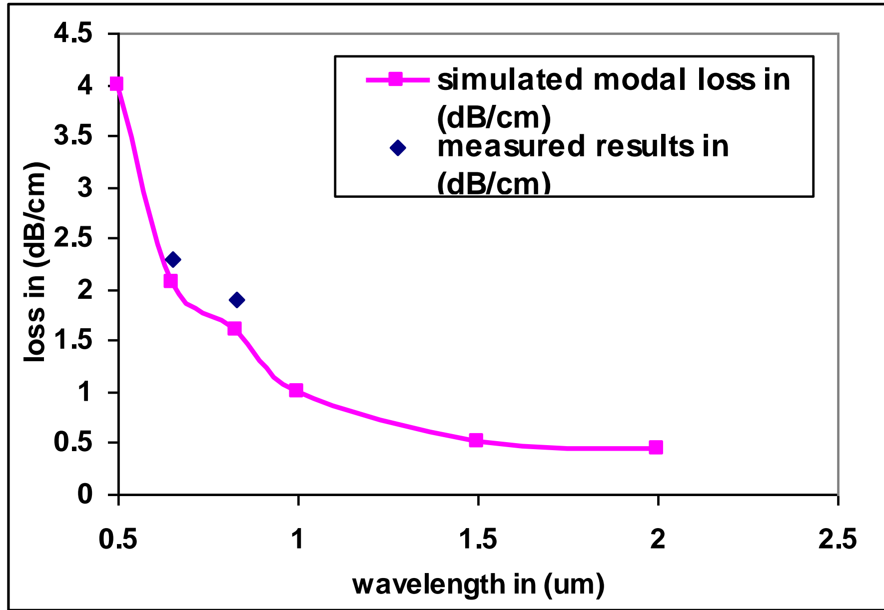

Figure 5.4: measured modal loss by Jain et al.[12] and simulated modal loss by my models as a function of wavelength

5.2.1.2 Optical waveguide made by Pirasteh et al.

Pirasteh et al. [25] demonstrated the design of both planar porous silicon waveguide (PSW) and oxidized porous silicon waveguide(OPSW)which are composed of a porous silicon guiding layer of a low porosity (high refractive index) surrounded by porous silicon cladding layer(s) with a higher porosity (low refractive index). As Pirasteh et al. [25] observed, "Porous silicon layers were obtained by electrochemical anodization of heavily *p*-type doped silicon wafers (5 mΩ cm). The electrolyte solution was HF (50%):H_2O: ethanol (2:1:2) at room temperature. To achieve multilayer planar optical waveguides, layers of different porosities (and thus different refractive indices) were formed by abruptly changing the anodization current. The (1-5) µm thickness of each of the guiding and cladding layers was controlled by the anodization time. The guiding (upper) layer and the cladding (lower) layer were formed by successively applying current densities of 50 and 80 mA/cm^2 in order to obtain porosities of about 60% and 65%,

respectively. This process was followed by a brief plasma etching in order to remove the superficial parasitic film. Then, the prepared structures were oxidized at 900 °C for 60 min in wet O_2 after a preoxidation step at 300 °C for 1 h".

5.2.1.2. a Optical waveguide loss measurement results

To understand the models that are used to calculate optical losses in a porous silica waveguide which we described in chapter 3, it is worthwhile to understand the measurement schemes of optical losses and compare the experimental results with the results obtained from the mathematical models.

Pirasteh et al. [25] measured the optical losses in OPSW by studying the scattered light from the surface of the waveguide. Laser light was single-mode fiber-coupled into the waveguide. The intensity of the scattered light was recorded with a digital camera placed above the sample.

Fig. 5.5 and its inset show, respectively, a typical 2D intensity distribution of the visualized light and its longitudinal variation. The last curve was obtained by integrating the data along each sampling transverse line. The light intensity decreased exponentially with the *z*-propagation distance as shown.

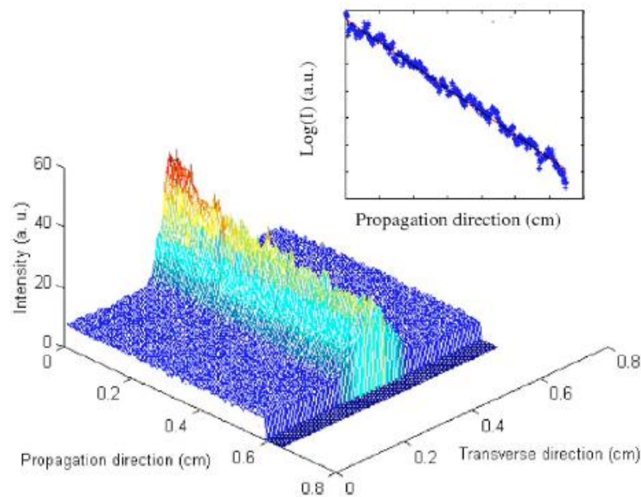

Figure 5.5: Two-dimensional light intensity for OPSW; inset: logarithmic of light intensity (i) propagating in the OPSW as a function of the propagation distance at 633 nm. **Reproduced from [25]**

One of the main advantages of the loss measurement experimental setup of optical waveguide is to observe the light propagation within the waveguide. In fact, the intensity of scattered light from the surface of the sample, recorded by the camera, is proportional to the intensity of guided light.

Fig. 5.6 represents a typical picture of light propagation in an OPSW at 633 nm. As we can see, the beam diverges and splits into several rays. Light behaved in this manner for both PSW and OPSW.

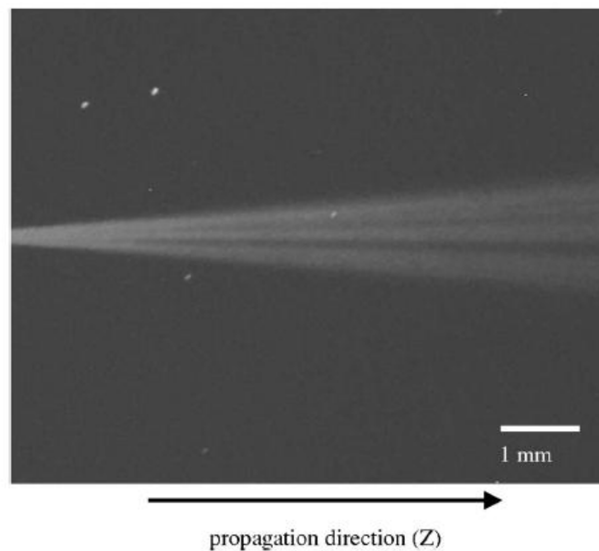

Figure 5.6: Top view picture of scattered light along the waveguide from OPSW at 633 nm: broadening of the beam. **Reproduced from [25]**

Pirasteh et al. [25] measured the total losses of porous silica waveguide as a function of the wavelength for OPSW. The measured values are shown in **Table 5.2.** Losses were about 0.6 dB/cm at λ=1550 nm. Obviously, losses decreased as the wavelength increased. However, there was a slight increase in losses between 980 and 1550 nm.

Table 5.2: Measured values of optical losses as a function of the wavelength OPSW [4].

Wavelength (nm)	loss of OPSW in (dB/cm)
46	2.4±0.5
633	1.8±0.5
980	0.5±0.3
1550	0.6±0.3

5.2.1.2.b The simulation results of the optical waveguides

I used matlab modesolver to simulate a waveguide with air as an upper cladding, OPS as a lower cladding and silica as a core with indices of 1, 1.263 and 1.45 respectively. The thicknesses of the lower cladding and the core are 3 um and 1 um in respectively using the ranges in Pirasteh et al. [25]. The modesolver simulation result for fundamental TE Mode of the waveguide lambda=1550 nm is shown in **Fig. 5.7**

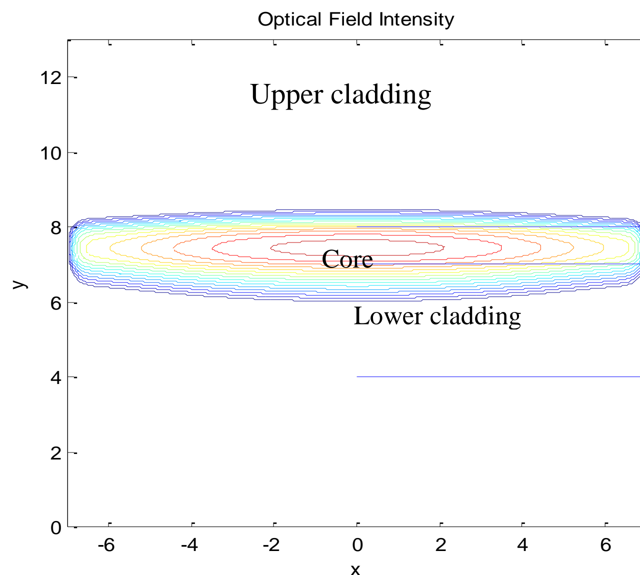

Figure 5.7: Modesolver simulation results for fundamental TE Mode of a planar OPS waveguide

In addition, Using the surface scattering model described in chapter 3, I simulated the same waveguide at λ=650 nm and the surface scattering loss was 0.158 dB/cm while the volume scattering loss was ~4 dB/cm. The results were in a good agreement with his results at λ= 650 nm with surface scattering and volume scattering losses of 0.25 dB/cm and 3 dB/cm respectively.

To compare with the measured results in Table 5.2, I simulated the waveguide modal loss as a function of wavelength, and I used σ=24 nm, R=16 nm. Porosity=30%, and I plotted both measured and simulated results together as shown in **Fig. 5.8**

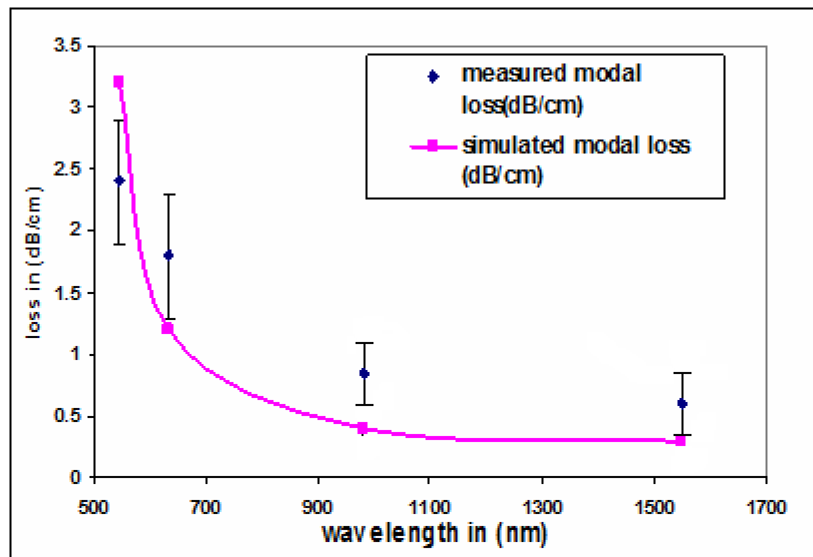

Figure 5.8: Simulated and measure modal lossas a function of wavelength

If we compare the measured results with the simulated modal loss as shown in **Fig. 5.8**, we will find good agreement between the results, for example at λ=1550, Fig. 5.8 shows a modal loss of~0.3 dB/cm which is half of the measured of 0.6 dB/cm as shown in Table 5.4. But, Pirasteh et al. [25] didn't specify the meaning of tolerances that he included in his table. So if we considered these numbers as bit error rates to represent the max and min values of the measured loss, the simulated results agree with the measured results.

References

[1] Stephen Beaudoin, Shaun Graham, Ravi Jaiswal, Caitlin Kilroy, Brum Soo Kim, Gautam Kumar, and Shanna Smith , "An Update on Low-k Dielectrics", The Electrochemical Society Interface, Summer 2005.

[2] Xie Jielin, "Study of TMCTS Based PECVD Carbon-Doped Low Dielectric Constant Material", MS thesis, department of physics, national university of Singapore, 2004.

[3] http://www.foothill-instruments.com/AP01.htm

[4] Rebeca C. Diaz, "Low-*k* Dielectrics: Materials and Process Technology", EE 518, Penn State, Instructor: Dr. J. Ruzyllo April 13, 2006. (http://wenku.baidu.com/view/bcf547ee172ded630b1cb63d.html)

[5] J. W. Fleming and D. L. Wood," Refractive index dispersion and related properties in fluorine doped silica", Applied optics / Vol. 22, No. 19 / 1 October 1983.

[6] Licheng M. Han, Ji-Sheng Pan, Shou-Mian Chen, N. Balasubramanian, Jianou Shi,Ling Soon Wong,and P. D. Foo," Characterization of Carbon-Doped SiO2 Low k Thin Films : Preparation by Plasma-Enhanced Chemical Vapor Deposition from Tetramethylsilane" , Journal. Electrochem. Soc. 2001volume 148, issue 7, F148-F153, [DOI: 10.1149/1.1375797]

[7] Alex Lim Ying Kiat , "Carbon Doped Silicon Dioxide Low k Dielectric Material ", M.S.thesis University of Sains Malaysia, 2004 . URL: http://eprints.usm.my/id/eprint/3087.

[8] Chang-Chung Yang and Wen-Chang Chen, "The structures and properties of silsesquioxane (HSQ) films produced by thermal curing **, J**. Mater. Chem.**,** 2002, 12, 1138-1141, [DOI**:** 10.1039/B107697N], First published online 22 Feb 2002.

[9] Min K. Yang ,Roger H. French ,DuPont Co. Central Research ,Experimental Station ,Wilmington, Delaware 19880-0400,Edward W. Tokarsky ,DuPont Fluoropolymer Solutions ,Chestnut Run Plaza ,Wilmington, Delaware 19880-0713 , "Optical properties of Teflon® AF amorphous fluoropolymers" ,c 2008 Society of Photo-optical instrumentation Engineers. [DOI: 10.1117/1.2965541].

[10] C.E. Mohler, E.G. Landes, G.F. Meyers, BJ. Kern, K.B. Ouellette, S. Magonov, "Porosity Characterization of porous SiLK Dielectric Films", 2003, CP683, Characterization and Metrology for VLSI Technology: 2003 International Conference.

[11] Hu Yi-Fan ,FU Dan-Rong, Zhang Ying ,Zhang Fan ,Tang Ting ," Dielectric Performance of Porous Methyl Silsesquioxane /Triacety1-β-cyclodextrin Thin Films", e-Journal , Issue 10 (October 2007) , Received 21 May 2007.

[12] A. Jain , S. Rogojevic, S. Ponoth , N. Agarwal , I. Matthew , W.N. Gill , P. Persans , M.Tomozawa , J.L. Plawsky , E. Simonyi ,"Porous silica materials as low-k dielectrics for electronic and optical interconnects", Elsevier Science, Thin Solid Films 398 – 399 (2001) 513–522

[13] Christophe Kopp, Stephane Bernab ´ e, Badhise Ben Bakir, Jean-Marc Fedeli, Regis Orobtchouk, ´Franz Schrank, Henri Porte, Lars Zimmermann, and Tolga Tekin," Silicon Photonic Circuits: On-CMOS Integration,Fiber Optical Coupling, and Packaging", IEEE Journal of selected topics in quantum electronics , MAY/JUNE 2011.

[14] D. Konjhodzic, S. Schröter, and F. Marlow ,"Ultra-low refractive index mesoporous substrates for waveguide structures Received 15 March 2007, revised 23 May 2007, accepted 15 June 2007, Published online 30 October 2007 , phys. stat. sol. (a) 204, No. 11, 3676–3688 (2007) / DOI 10.1002/pssa.200776405.

[15] Stephen Beaudoin, Shaun Graham, Ravi Jaiswal, Caitlin Kilroy, Brum Soo Kim, Gautam Kumar, and Shanna Smith, "An Update on Low-k Dielectrics", The Electrochemical Interface, Summer 2005.

[16]Tim A. Erickson, , and Kevin L. Lear, "Optimization of the Local Evanescent Array-Coupled Optoelectronic Sensing Chip for Enhanced, Portable, Real-Time Sensing", IEEE Sensors Journal, MAY 2013.

[17] S. V. Nitta, V. Pisupatti, A. Jain, P. C. Wayner Jr., W. N. Gill, and J. L. Plawsky, "Surface modified spin-on xerogel films as interlayer dielectrics", Journal of Vacuum Science & Technology B 17, 205 (1999); doi: 10.1116/1.590541, Published by the AVS: Science & Technology of Materials, Interfaces, and Processing.

[18] S. V. Nitta, A. Jain, P. C. Wayner, Jr., W. N. Gill, and J. L. Plawsky, " Effect of sol rheology on the uniformity of spin-on silica xerogel films", Journal of applied physics, Isermann Department of Chemical Engineering, Rensselaer Polytechnic Institute, Troy, New York 12180, 1999.

[19] A. Fallahkhair, K. Li and T. Murphy, "Vector finite difference modesolver for anisotropic dielectric waveguides," *J. Lightwave Technol*., 2008, 26, 1423-1431.

[20] I. Hoseinzadeh, R. S. Dariani . "Measurement of optical loss in oxidized multilayer planar porous silicon waveguides ", Optoelectronics and advanced materials-rapid communications vol.1, No. 9, September 2007, p. 471 - 476, Department of Physics, Alzahra University, Tehran, 19938, Iran

[21] Ma.Concepción Arenas, Marina Vega, Omar Martínez and Oscar H. Salinas. " Nanocrystalline Porous Silicon: Structural,Optical, Electrical and Photovoltaic Properties".

[22] D. A. G. Bruggeman, Ann. Phys. **24**, 636 (1935).

[23] H. Looyenga, Physica _Amsterdam_ **31**, 401 (1965).

[24] J. C. M. Garnett, Philos. Trans. R. Soc. London, Ser. A **203**, 385 (1904).

[25] Parastesh Pirasteh, Joël Charrier, Yannick Dumeige, Séverine Haesaert, and Pierre Joubert, "Optical loss study of porous silicon and oxidized porous silicon planar waveguides", Journal of Applied Physics **101**, 083110 (2007); DOI: 10.1063/1.2718886

Chapter 6: LEAC sensor design using porous silica as lower-cladding

6.1 Introduction

One of the main goals of my research work is to study the properties of porous silica optical waveguides and demonstrate the ability to use them in biosensing applications.

To understand the sensing mechanisms, it is important to clarify several biosensor terms. Sensitivity is one of the important parameters that are required to understand the biosensor's performance. It can be defined as the change in the value of the output signal produced by the transducer in response to the change of refractive index due to analyte binding [4].

Another key parameter to characterize the performance of the sensor is the noise level. The most common noise for most label-free optical biosensors is caused by noise fluctuations, that results in, changing the refractive index due to noise level, and this will change the measured signal[4].

Limit of detection (LOD) represents the lowest quantity of a substance that can be distinguished from the absence of that substance, and it is usually defined as 3×standard deviation (SD). There are many ways to specify the LOD. LOD in units of refractive index units (RIU) is the most commonly used to evaluate the sensor's performance, because all sensors are sensitive to a RI change in a bulk solution, and hence using this method can provide a rough standard to compare the performance for different biosensors[4].

Another important term related to photodetectors is Signal-to-noise ratio (SNR). It represents the ratio of a desired signal power to the noise power. It is often expressed in decibels. If the SNR is greater than 0 dB that means the signal power is more than the noise power.

For the device to be used in sensing mechanism we need to improve the LOD of the device by increasing its sensitivity. Furthermore, we need a high SNR of the photodetectors that will be used to measure the change in photocurrent in response to analyte binding on a LEAC sensor. Using the modesolver we can optimize the parameters of the device to improve the SNR. The amount of photodetector coupling should be enough to have high SNR, otherwise the measured signal will be overwhelmed by noise and incorrect results will be measured by photodetectors.

In this chapter we have used modesolver to test the ability of using the optical waveguide made by Jain et al.[1] in sensing mechanisms. Also, we have included predictions for an optical waveguide parameters using Matlab modesolver to be able to use it in sensing applications i.e. as a LEAC biosensor.

6.2 Can we use Jain et al.'s waveguide as a LEAC sensor?

In this section I will simulate for xerogel-oxide planar optical waveguide designed by Jain et al., where he used core thicknesses of (0.78 and 0.94) um, and lower cladding thickness of values ≥ 1 um. Modesolver simulation results for fundamental TE mode of LEAC waveguides assuming it is used for sensing in different upper cladding environments is shown in **Fig. 6.1**. The lateral lines indicate the position of the upper cladding, lower cladding, and silicon, respectively. The thin core is not visible in the image, but is located just above the line separating the upper and lower cladding regions. A description of each waveguide is provided in Table 6.1.

As shown in the table, I used lower cladding with thicknesses greater than 1 which is in the range of what Jain et al.[1] used in his experiment, in his experiments he used (0.94 and 0.78) um core, but I used 0.36 um core which is in the range of his core thicknesses, that because I couldn't get coupling to photodetectors and high sensitivity using exact same values that he used.

The table includes the photodetector coupling loss, the % coupling on the upper cladding and the sensitivity in (%/RIU).

Furthermore, I am showing the results of surface scattering loss using the scattering models that we described in chapter 3, assuming a roughness of 2 nm at the interface between the core and lower cladding and the volume scattering loss assuming the diameter of pore=17 nm although Jain et al.[1] assumed negligible scattering loss in his work.

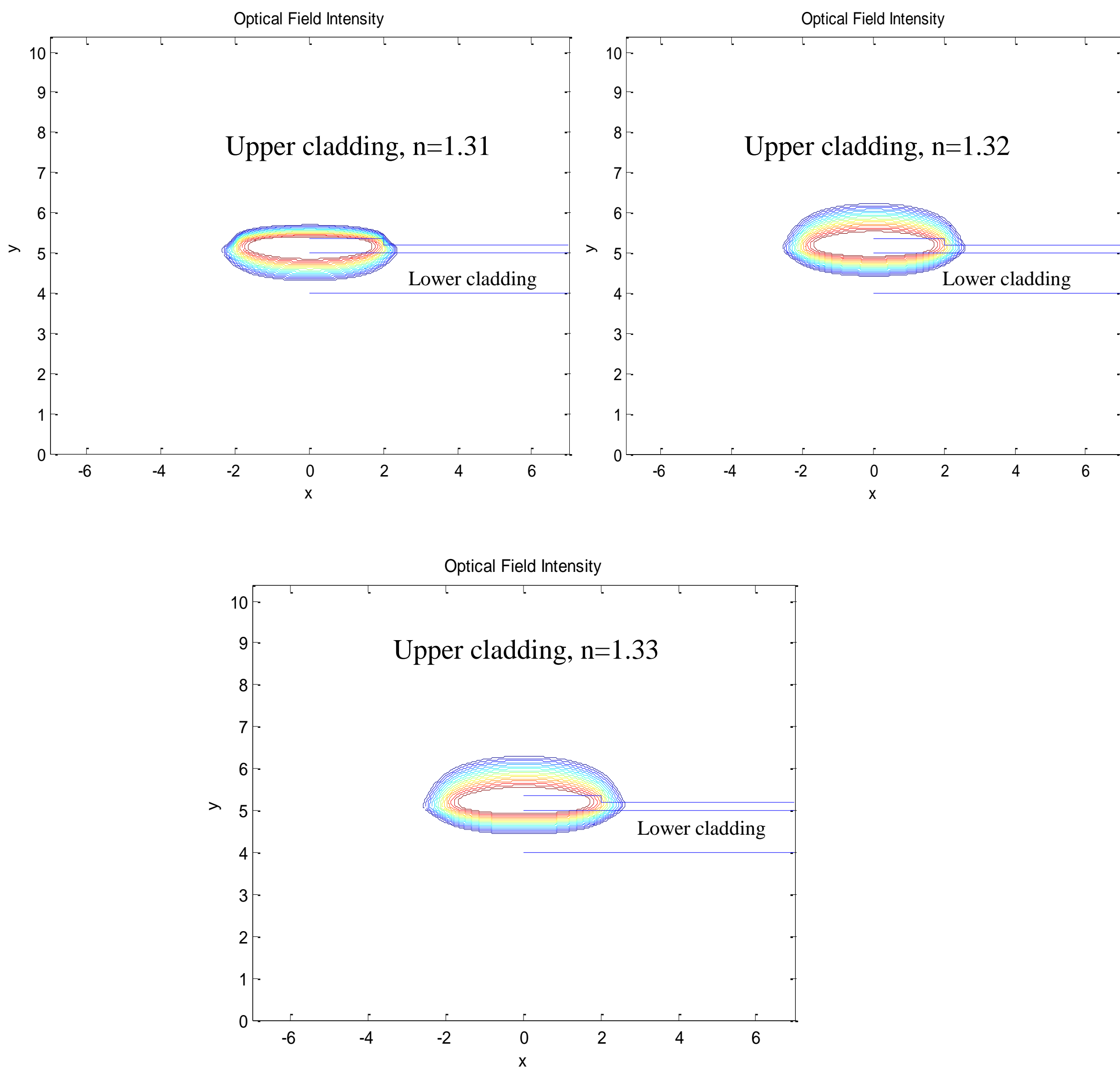

Figure 6.1: Modesolver simulation results for fundamental TE mode of **Oxide-xerogel** LEAC waveguides used for sensing in different upper cladding environments.

Table 6.1: The simulation results of the waveguide designed by Jain et al. [1]

Upper cladding index	**1.31**	**1.32**	**1.33**
Waveguide width(micron)	4	4	4
Core material	SiO_2	SiO_2	SiO_2
Core thickness	0.36	0.36	0.36
Core index	1.45	1.45	1.45
Lower cladding thickness	1	1.25	1.7
Lower cladding material	Silica xerogel	Silica xerogel	Silica xerogel
Lower cladding index	1.26	1.26	1.26
Lambda (nm)	650	650	650
n_{eff}	1.373	1.374	1.377
Photo detector Coupling loss(dB/cm)	0.29	0.021	0.018
%Optical power in upper cladding	11.29	11.047	10.765
Sensitivity(%/RIU)	1053.3	1382.9	1560.3
Surface scattering loss (dB/cm) @ σ=2 nm	5.896	5.584	5.241
Volume scattering loss(dB/cm) @ pore diameter=17 nm	5.056	5.056	5.056
Modal loss in (dB/cm)	6.75	6.14	5.776

The question was whether we can use Jain et al.'s porous silica waveguide as a LEAC sensor or not. The answer to this question depends on the results of photodetector coupling loss and sensitivities. For the waveguide to work as a LEAC sensor we need high sensitivity and high SNR for the buried photodetectors. As shown in Table 6.1, the sensitivity increases by increasing

the lower cladding thickness and the photodetector coupling loss decreases at the same time, which makes sense for me, because we know it is a tradeoff between the sensitivity and the photodetector coupling loss, but comparing with previous works on LEAC chips these values of sensitivity are not considered very large. For example, the maximum sensitivity in Table 6.1 is 1560.283%/RIU which is small comparing with the max sensitivity achieved in Erickson's dissertation [2] which was 8880 %/RIU.

Furthermore, values of coupling loss are very small, so there is very little optical power coupled into the optical detector and the small signal becomes overwhelmed by a combination of background scattered light and photodetector noise.

In addition, Jain et al.[1] in his work ignored the scattering loss which doesn't make sense to me, because I assume the scattering loss of porous silica waveguide is higher than the normal dielectrics waveguide so we can't ignore it, and the simulation results show high surface and volume scattering loss which will make the situation worse. Therefore, if we didn't make any changes to Jain et al.'s waveguide, we will not get a good sensor. So I can conclude that Jain et al.'s waveguide can't be used as a good LEAC sensor because of low sensitivities and low SNR. But, if we modify its parameters we can improve its performance as a LEAC sensor.

6.3 Predictions of a LEAC sensor using porous silica

To use the porous silica waveguide designed by Jain et al. [1] as a LEAC sensor we need to modify its parameters until we can get high sensitivity and high SNR.

6.3.1 The first prediction assuming porosity of 40%

In this part, the waveguide's layer thicknesses were chosen by modeling to improve the properties of porous silica waveguide, and obtain a high performance LEAC chip that can be used in sensing application. Therefore, I used a thinner core to improve the sensitivity of the

device, and at the same time I changed the lower cladding thickness until I obtained acceptable values of the photodetector coupling loss, and that is important to increase the SNR. I assumed 40% porosity which is the same as the porosity used in Jain et al. [1]

The local evanescent field shift effect is illustrated in **Fig. 6.2**, which are modesolver simulation results for fundamental TE mode of LEAC waveguides assuming it is used for sensing in different upper cladding environments. The lateral lines indicate the position of the upper cladding, lower cladding, and silicon, respectively. The thin core is not visible in the image, but is located just above the line separating the upper and lower cladding regions. Notice that the field is shifted upward and that there is minimal interaction of the evanescent field with the underlying Si when the upper cladding has an index of n=1.33; however there is significant interaction when n=1.32. As such, photodetector coupling is significantly higher for n=1.31. For sensing applications, analyte binding or partitioning into the upper cladding sensing region causes an increase in refractive index, and therefore a decrease in the measured photocurrent.

A description of each waveguide is provided in Table.6.2. The table includes the photodetector coupling loss, the % coupling on the upper cladding and the sensitivity in (%/RIU). Furthermore, I am showing the results of surface scattering loss using my model assuming a roughness of 2 nm and the volume scattering loss assuming the diameter of pore=17 nm.

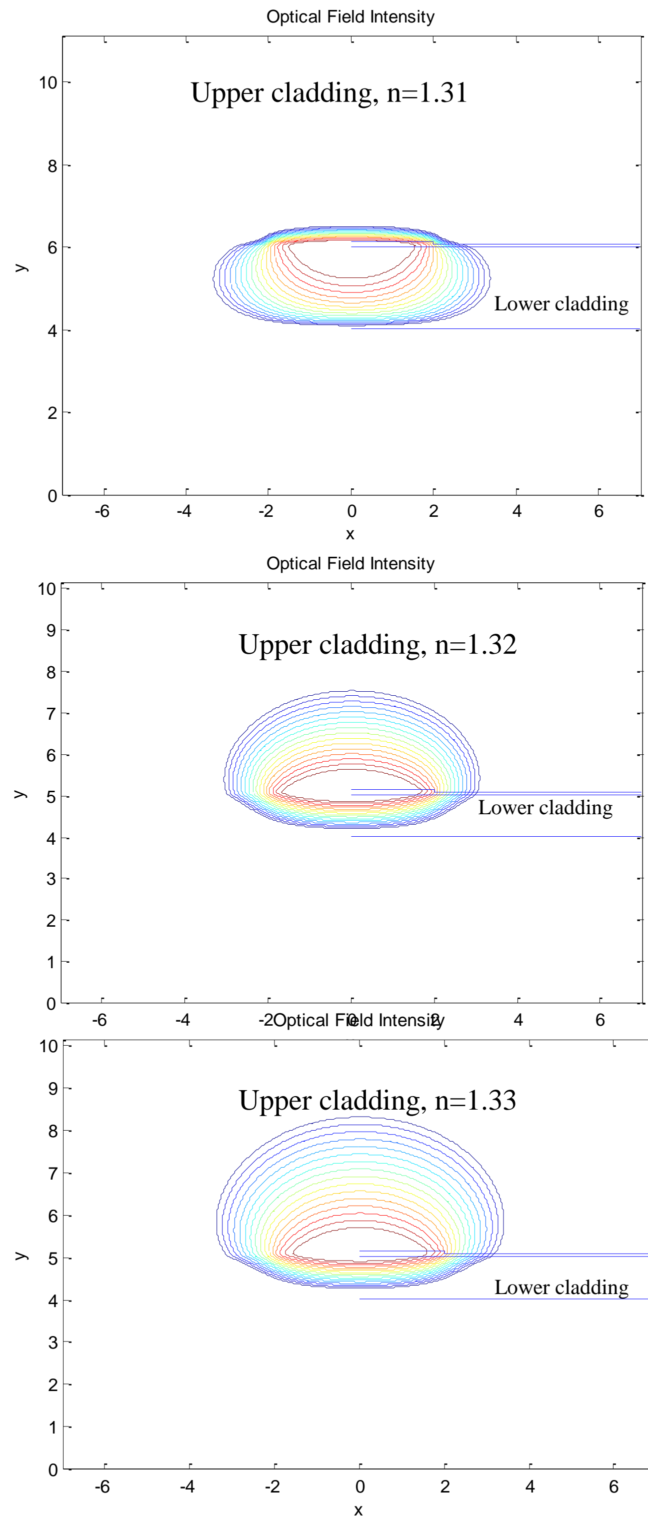

Figure 6.2: Modesolver simulation results for fundamental TE Mode of **Oxide-xerogel** LEAC waveguides used for sensing in different upper cladding environments using my prediction.

Table 6.2: The simulation results of the waveguide using the dimensions I predicted assuming a porosity of 40%

Upper cladding	**1.31**	**1.32**	**1.33**
Waveguide width(micron)	4	4	4
Core material	SiO_2	SiO_2	SiO_2
Core thickness	0.14	0.14	0.14
Core index	1.45	1.45	1.45
Lower cladding thickness	1	1.25	1.7
Lower cladding material	Silica xerogel	Silica xerogel	Silica xerogel
Lower cladding index	1.26	1.26	1.26
Lambda (nm)	650	650	650
n_{eff}	1.3163	1.3229	1.3304
Photo detector Coupling loss(dB/cm)	10.3	4.6	2.5
%Coupling on upper cladding	34.9	29.8	26.3
Sensitivity(%/RIU)	2724	6958	6984
Surface scattering loss (dB/cm) @ σ=2 nm	8.94	8.95	2.72
Volume scattering loss(material loss)(dB/cm) @ pore diameter=17 nm	5.058	5.058	5.058
Modal loss	19.9	14.9	6.4

6.3.2 The second prediction assuming a porosity of 63%

In the second prediction I assumed that we can also modify the porosity of porous silica to obtain new refractive index values for the waveguide's lower cladding. In this prediction I assumed a porosity of 63% for the porous silica lower cladding to get new value of refractive index of 1.17 for the lower cladding. **Fig.6.3** shows three modal solutions for rib waveguides simulated assuming a low-k dielectric xerogel as lower cladding. All of the waveguides have the same dimensions.

The solutions were made to compare the results of using air as upper cladding with other materials that are used for sensing mechanism, 1.32 upper cladding sensing, and 1.33 upper cladding sensing. The fraction of the field present in the upper cladding sensing region is found to be much higher for the 1.33 upper cladding sensing waveguide than the 1.32 upper cladding sensing waveguides. Also, the fraction of the field is much higher than the field present when 1.31 upper cladding, consistent with the evanescent field shift effect.

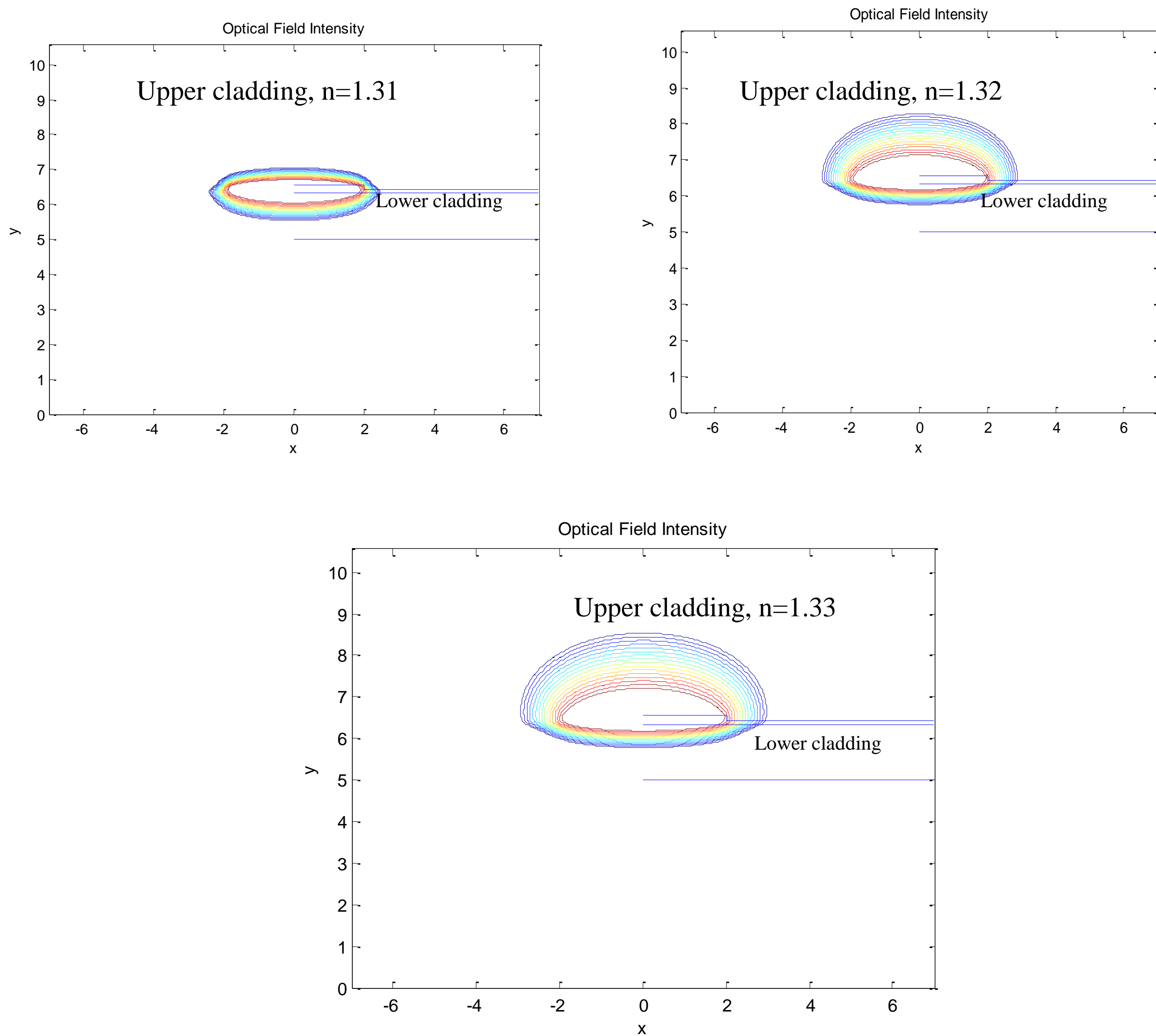

Figure 6.3: Modesolver simulation results for fundamental TE Mode of **Oxide-xerogel LEAC** waveguides used for sensing in different upper cladding environments.

A description of each waveguide is provided in Table 6.3. The table includes the photodetector coupling loss, the % coupling on the upper cladding and the sensitivity in (%/RIU). Furthermore, I am showing the results of surface scattering loss using my model assuming a roughness of 2 nm and the volume scattering loss assuming the diameter of pore=17 nm.

Table 6.3: The simulation results of the waveguide using the dimensions I predicted assuming a porosity of 63%

Upper cladding	**1.31**	**1.32**	**1.33**
Waveguide width(micron)	4	4	4
Core material	SiO_2	SiO_2	SiO_2
Core thickness	0.24	0.24	0.24
Core index	1.45	1.45	1.45
Lower cladding thickness	1.3	1.3	1.3
Lower cladding material	Silica xerogel	Silica xerogel	Silica xerogel
Lower cladding index	1.17	1.17	1.17
n_{eff}	1.302303	1.338654	1.343375
Lambda (nm)	650	650	650
Photodetector Coupling loss(dB/cm)	10.7	4.1	3.6
%Coupling on upper cladding	30.6	35.18	35.3
Sensitivity(%/RIU)	6120	7036	7060
Surface scattering loss (dB/cm) @ σ=2nm	3.7	3.7	3.7
Volume scattering loss(material) (dB/cm) @ pore diameter=17 nm	4.36	4.36	4.36
Total Modal loss(dB/cm)	16.3	9.2	8.6

6.3.3 Modal loss

In previous sections we focused on calculating the material loss in optical waveguides. This loss includes the light intensity in all layers, core, lower cladding, and upper cladding. Since we are interested in using the optical waveguide as an optical sensor, it is important to know the modal loss which is the only loss that we can measure.

To find the modal loss, we assumed a negligible material loss in the core and the upper cladding and it is dominated by volume scattering in lower cladding. To find the modal loss, we need to find the confinement factor as we discussed in chapter 2. The confinement factor as we discussed in chapter 2 can be described using (Eq.2.29).

We used (Eq.2.34) to find the modal loss where

Modal loss= $\alpha_{\text{material_lower cladding}} * \Gamma_{lowercladding} + \alpha_s + \alpha_{\text{absorption}}$

Material loss= material loss in the core + material loss in lower cladding +material loss in the upper cladding.

Hence, we assume negligible material losses in the core and the upper cladding, so we only consider material loss in the lower cladding.

Where $\Gamma_{lowercladding}$ is the lower cladding confinement and we found it using (Eq.2.17)

Lower cladding confinement is $= \dfrac{n_{lowercladd}}{n_{lowercladd} + n_{uppercladd}} (1 - \Gamma)$

I added the equations to the modesolver to find the modal loss of an optical waveguide. The value of the modal loss depends on the waveguide refractive indices, the core thickness, and the cladding thickness. Furthermore, as the modal loss depends on the material loss which represents volume scattering in lower cladding in our case. Also it highly depends on the amount of surface scattering and the photodetectors coupling loss. The value of the modal loss might

have impact on the sensitivity of the device and the photodetector coupling. Therefore, for the device to work as a good sensor we need to make sure that we have acceptable values of modal loss in lower cladding.

Fig.6.4 represents a plot of sensitivity, modal loss, and photodetector coupling vs. lower cladding thickness for a 0.14 μm core optical waveguide. The simulated RIU change is Δn=0.005, from n=1.310 to n=1.315. As shown in this figure, sensitivity increases with lower cladding thickness. However, notice that as sensitivity increases, the magnitudes of photo detector coupling and modal loss decay exponentially with lower cladding thickness. The sensitivity increases linearly with core-detector distance (lower cladding thickness).

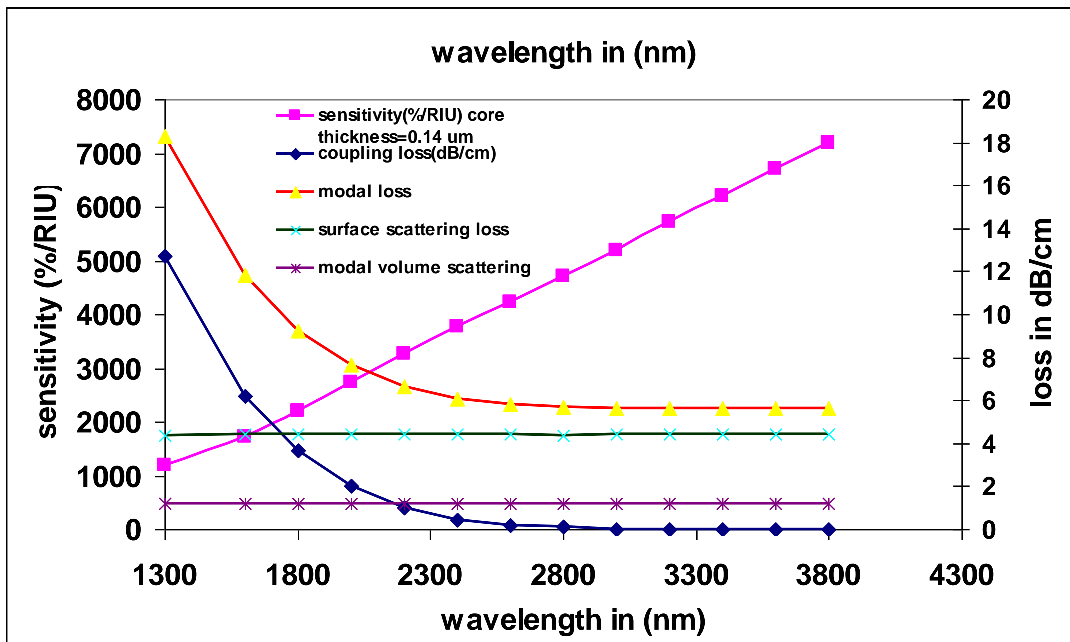

Figure 6.4: Plot of sensitivity, photo detector coupling, modal volume scattering, surface scattering and total modal loss for core thickness=0.14 um

6.3.4 Concluding remarks

Comparing with previous works on LEAC sensors, the results in tables (6.2 and 6.3) show the possibility for using porous silica optical waveguides as LEAC sensors. The results show a good difference in sensitivity and photo detector coupling loss comparing with the values

obtained in table.6.1 in section 6.1 using Jain et al.'s design's parameters and dimensions. In table 6.1, the maximum sensitivity is 1560.3%/RIU, where in Tables (6.2 and 6.3) the maximum sensitivities are 6984 and 7060 respectively. However, the maximum sensitivity that for example Erickson et al.[2] could get in his dissertation was 8080 %/RIU.

Using the simulation results we can prove that the device sensitivity is highly dependent on the lower cladding thickness, waveguide core height, core index and the magnitude of absorbed scattered power. Thus, in order to maximize the sensitivity of a porous silica waveguide and target a specified photo detector coupling magnitude, we need to precisely choose the waveguide's parameters and at the same time make sure that we are still achieving a single mode condition. Furthermore, the evanescent coupling for single mode waveguides was found to exhibit an inverse exponential dependence on lower cladding thickness as shown in **Fig.6.5**

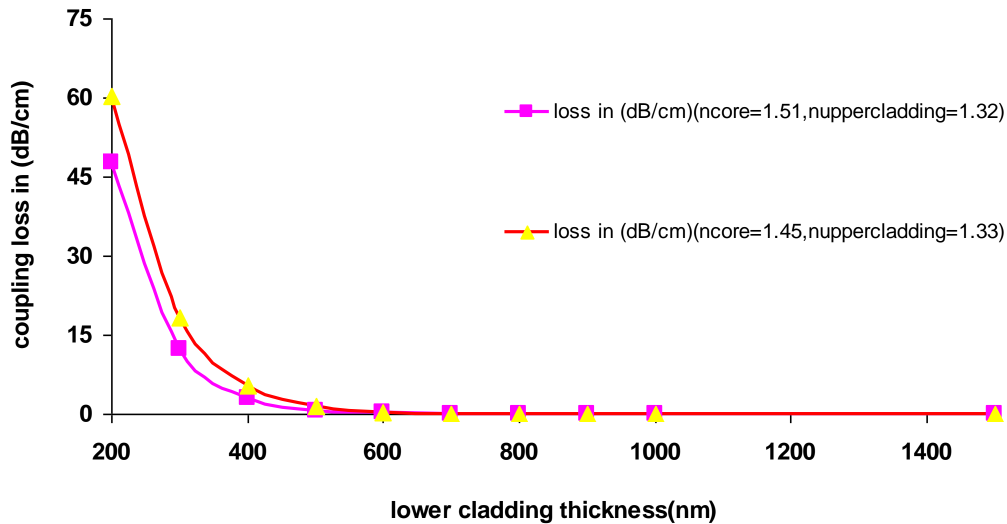

Figure 6.5: Photo detector coupling loss in dB/cm as a function of lower cladding thickness in nm for different values of core and upper cladding indices.

Furthermore, as we discussed in chapter 4, modesolver results indicate that it is not necessarily for the waveguide core thickness to be designed to be at cutoff to achieve high

sensitivity. In my prediction I used a thin lower cladding with the thickness of the core above the cut off value. Therefore, the optimum core thickness depends on the lower cladding thickness. For increasing lower cladding values, the waveguide should be designed to be at cutoff.

However, for thinner lower cladding values, the waveguide should be designed to be slightly above cutoff. **Fig. 6.6** demonstrates that device sensitivity is also dependent on a core thickness, the figure shows that for lower values of lower cladding thickness, the sensitivity increases by increasing the core thickness and for higher values of lower cladding thickness the sensitivity decreases by increasing the core thickness and this was also demonstrated for LEAC chips using normal dielectrics by Erickson et al.[2]

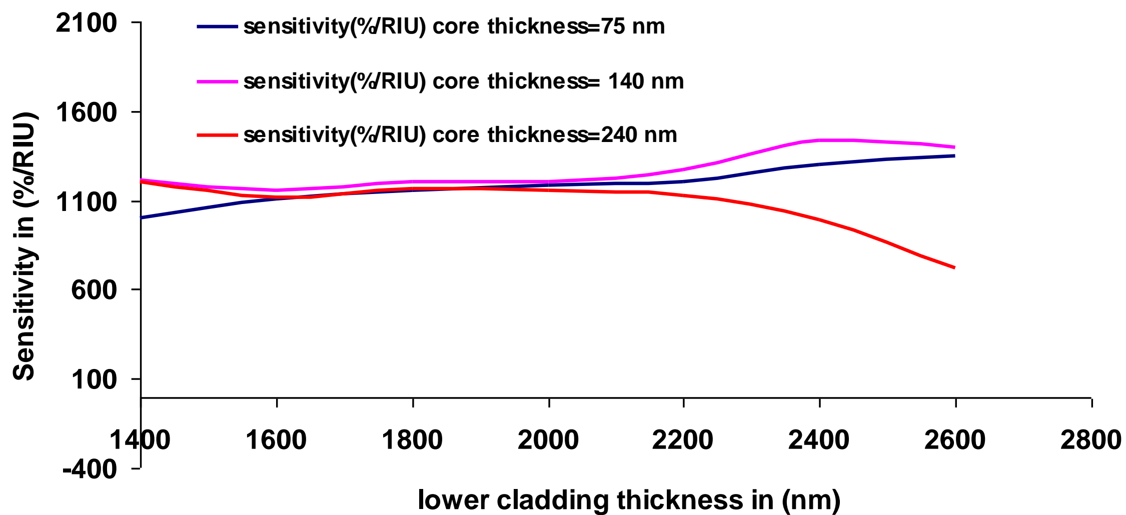

Figure 6.6: Plot of sensitivity as a function of lower cladding thickness for core thicknesses of (75, 140 and 240) nm

In addition, we should consider the effect of scattering loss on the operation of the device. The scattering loss affects the device sensitivity and the optimal lower cladding thickness. At high values of scattering, a large photocurrent offset overwhelms evanescent signal and the sensitivity goes to zero. Suppose α_0 and α_f be the coefficients of evanescent power coupling

before and after a Δn=0.005 RIU increase. The modulation when scattering s is taken into account *Ms* is then given by, $M_s = 1 - \frac{(1-e^{-\alpha_0 l}) + (1-e^{-s_{tot} l})}{(1-e^{-\alpha_f l}) + (1-e^{-s_{tot} l})}$ (Eq. 6.1)

$s_{tot} = \alpha_s + \alpha_{vscat} * \Gamma_{lower\text{-}cladding}$.

Note that as s_{tot} increases the modulation decreases, then the sensitivity will also decrease. Erickson et al.[2] stated that, "Scattering affects the device sensitivity on two fronts. First, it reduces the amount of power in the guided mode, thereby leading to increased amplifier noise due to the higher required gain and increased proportional shot noise. Secondly, a high scattering background confounds measurement of the evanescently coupled signal, thereby reducing device sensitivity". Fig. 6.7 is a plot that shows sensitivity as a function of the magnitude of absorbed scattered light in dB/cm. The plot reveals that sensitivity is ultimately limited by scattering and that the optimal lower cladding thickness depends on the intrinsic scattering properties of the waveguide.

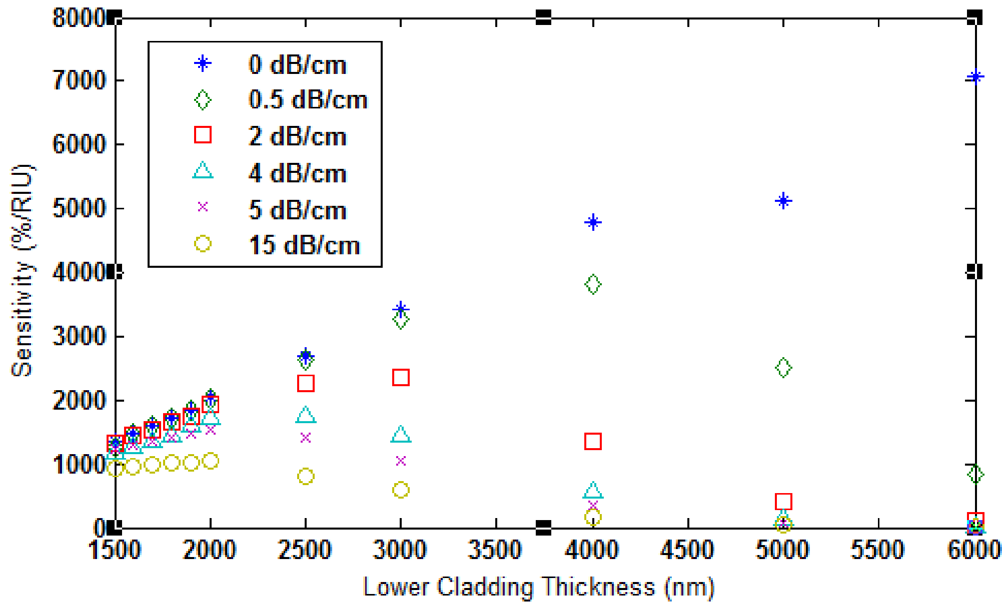

Figure 6.7: Effect of scattered power on sensitivity and optimal lower cladding thickness, where the core thickness is 0.14 μm, the core index is 1.45, and the porosity is 40%

The figure shows that at high values of scattering the sensitivity goes to zero and the optimal lower cladding thickness has lower values. Optical waveguides with porous silica cladding have high volume and surface scattering losses. Thus, to design a LEAC sensor using porous silica lower cladding we have to pay attention to the preparation methods to reduce scattering loss to ensure high sensitivity and high SNR.

Finally, we applied surface and volume scattering loss models on porous silica waveguides and LEAC sensors with different indices and dimensions. We noticed that for porous silica waveguides in the visible spectrum, losses were mainly due to volume scattering whereas in the near infrared spectrum, losses were principally due to surface scattering. But, in LEAC sensors with porous silica claddings losses were dominated by surface scattering in all regions. **Fig. 6.8** shows the results of modal volume scattering and surface scattering losses for porous silica waveguides and LEAC sensors with different indices and dimensions.

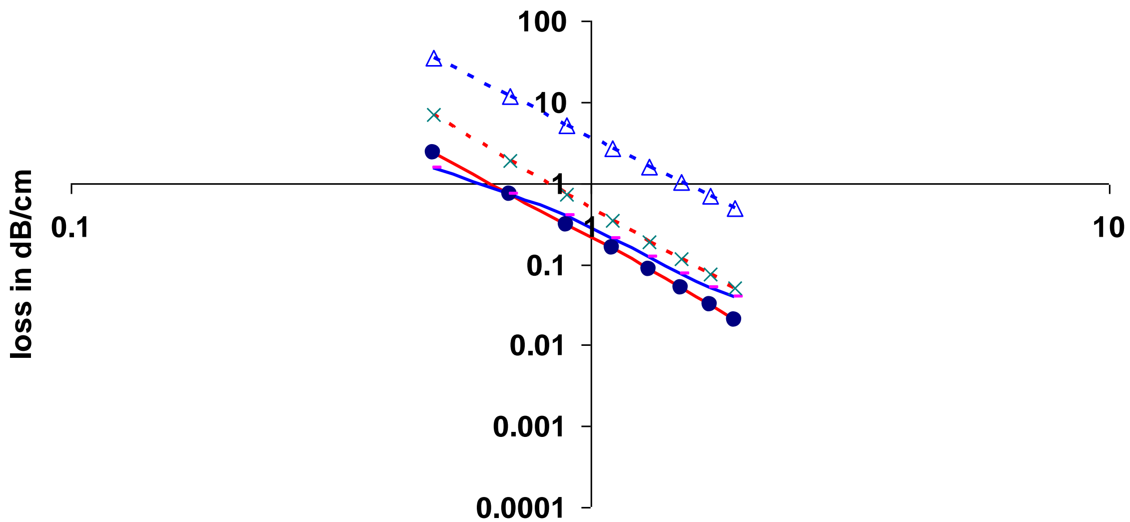

Figure 6.8: The porosity is 30%, n_{core}=1.51, dashed lines represents the data for 0.07 μm core thickness, solid lines represents the data for 2 μm core thickness.. Red lines: modal volume scattering loss, blue lines: surface scattering loss(both axis are in log-scale)

References

[1] A. Jain , S. Rogojevic, S. Ponoth , N. Agarwal , I. Matthew , W.N. Gill , P. Persans , M.Tomozawa , J.L. Plawsky , E. Simonyi ,"Porous silica materials as low-k dielectrics for electronic and optical interconnects", Elsevier Science, Thin Solid Films 398 – 399 (2001) 513–522

[2] Timothy Erickson, "Design optimization and fabrication of an integrated optoelectronic sensing chip for applications in real-time biosensing and groundwater contaminant detection", Ph.D. dissertation, Dept. Electrical and Computer. Eng. , Colorado State University Fort Collins, Colorado Summer 2014.

[3]Tim A. Erickson, , and Kevin L. Lear, "Optimization of the Local Evanescent Array-Coupled Optoelectronic Sensing Chip for Enhanced, Portable, Real-Time Sensing", IEEE Sensors Journal, MAY 2013.

[4] Rongjin Yan, "A CMOS compatible optical biosensing system based on local evanescent field shift mechanism", Ph.D. dissertation Dept. Electrical and Computer. Eng. , Colorado State University Fort Collins, Colorado Fall 2011.

Chapter 7: Conclusions and Future Work

This chapter summarizes the achievements of the research work of this thesis. Conclusions and suggestions for future work are given based on thesis achievements.

7.1 Achievements

The overall objective of this MS research work is to study the design of optical waveguides using low-k dielectrics, and to use accurate mathematical models to calculate the scattering losses of the waveguide. Full-Vector Finite Difference Modesolver method has been applied to achieve a better understanding of the working mechanism of the optical waveguide. The achievements include:

1) Simulating of optical waveguides made by Erickson et al. using Matlab mode solver and comparing my simulated results with his simulated results.

2) A table for the last update of low-k dielectrics was included; I made this table depending on my reading for many low-k dielectrics references.

3) Preparation methods of porous silica were reviewed.

4) Simulating porous silica waveguides made by Jain et al. and Pirasteh et al. using matlab modesolver and comparing the simulated results with the experimental results.

5) A mathematical model for surface scattering loss calculations was used and added to the Matlab mode solver.

6) A mathematical model for volume scattering loss calculations was used and added to the Matlab mode solver.

7.1.1 Theoretical study of LEAC sensors

Optical waveguide has been modeled using Full-Vector Finite Difference Modesolver written in MATLAB. Some of the most important parameters were studied and optimized. For

example, the relationship between the geometric dimensions of the waveguide in the LEAC sensor and the refractive indices of the waveguide layers has been studied to ensure a single mode waveguide in the LEAC sensor. Furthermore, the relationship between the waveguide dimensions and attenuation has been simulated for waveguides made by high k-dielectrics and porous silica waveguides.

7.1.2 Measurement of optical losses in optical waveguides

The methods that are commonly used to measure the losses in optical waveguides have been studied such as the cut-back method, the Fabry-Perot method, and the measurement of scattering light from the surface of porous silica waveguide.

7.1.3 Preparation methods of porous silica

The methods that are mainly used to prepare porous silica have been studied and the main models that are used to find the refractive index of porous silica have been considered.

7.1.4 Optical waveguides loss calculations

The models that are used to calculate the optical losses have been studied. Two models have been used and added to the modesolver code. The first model is to calculate the surface scattering loss while the second model is to calculate the volume scattering loss.

7.2 Conclusions

We have simulated porous silica optical waveguides made by Jain et al. and Pirasteh et al. with negligible absorption losses and low scattering losses.

Porous silica is used as a low-k dielectric lower cladding due to its advantages over high-k dielectric silica to increase the optical confinement and allow simultaneous manufacturing of photonics and electronics on same chip.

Therefore, paying attention to the preparation method of porous silica we can get a high performance porous silica optical waveguides which can be used in communication systems.

The use of Matlab modesolver gives good information about the main parameters of the waveguide and the effect of these parameters on its operation. We can solve for the waveguide's leaky modes and decide the waveguide dimensions that help to design low-loss optical waveguides.

Furthermore, by using mathematical models for the waveguide scattering loss we can get good approach to the main factors that affect the waveguide's operation and use the results to design optical waveguide with better agreement between the experimental and theoretical results. Finally, we can design LEAC sensors using optical waveguides with porous silica lower claddings by paying a careful attention to the preparation method of porous silica to reduce the scattering loss and optimize the parameters of the device to insure high sensitivity and high SNR.

7.3 Future work suggestions

For a very large-scale integrated (VLSI) photonic scheme, optical waveguides designs with thin claddings and small bending radii are desired. A thin cladding would allow small inter-waveguide spacing for a given amount of crosstalk. Thus, this describes the need for a waveguide with a high refractive index between the core and cladding. By paying a careful attention to porous silica waveguide fabrication process it can be used for high density on-chip optical waveguides to replace the electrical interconnects and this will also allows integrating so many components on the same chip.

Metal Oxide Semiconductor Implementation Service (MOSIS) system provides multi-project wafers (MPWs) and related services that drive IC innovation. At the beginning of my research work I was going to design a LEAC chip using MOSIS technologies. But because of the

lack of the information that MOSIS provides for general users I didn't have enough information about the materials that MOSIS technologies use in their designs. After studying the low-k dielectrics and the optical waveguide designed using low-k dielectrics I realized that most of MOSIS technologies use low-k dielectrics in most of their designs. After characterizing a porous silica waveguide and simulating it using modesolver we can determine the main parameters and dimensions that help to design a practical waveguide and then we can use MOSIS system to design porous silica waveguide that can be used in ICs and/or communication systems.

Furthermore, after optimizing and characterizing the porous silica waveguide we are planning to use it in designing a LEAC sensor with buried detectors array that can be used in biosensing applications. The sensor that we are interested to design has the same principle as the LEAC chips that were designed before, but we just want to use porous silica in lower cladding and try to improve the properties of the waveguide to get better LOD, good sensitivity, and high SNR for the photodetectors array

Appendix A: Fabrication Process Flow of porous silica waveguides with porous silica made by electrochemical etching

Formation mechanism of porous silicon

I added this appendix to have a clear understanding of one of the most commonly used method of fabricating porous silica, which is called electrochemical etching. I am adding the exact same information from **Ref.[18].** The only thing I changed is the references numbers that he used in his observation; I just changed them to add them as references to this appendix.

As Xing Weir et al. [18] observed, "The porous silicon is fabricated by electrochemical etching of silicon in a hydrofluoric acid based electrolyte. It is the most commonly used method of fabricating PSi and is usually conducted in the dark to prevent photogenerated currents from contributing to the formation process [1, 2]. The exact formation process of PSi is still under debate. A number of theories have been proposed on the formation mechanisms and morphologies of PSi. In the early 1990s, Lehmann and Gösele proposed the quantum wire effect to explain pore formation on p-type silicon [1]. **Fig.A.1** illustrates this chemical dissolution mechanism, which is recognized as the main mechanism during the PSi formation [4]".

"In the Lehmann and Gösele theory, the silicon/HF solution interface behaves like a Schottky contact [8]. **Fig.2** (a) shows the band diagram of the p-type Si/PSi/HF electrolyte solution interface under current flow. Holes transfer occurs at the bottom of the valence band (VB) edge, which is physically at the PSi/Si interface (pore tips, **Fig.A.2** (b)) [7]. The pore walls are depleted of the holes necessary for the dissolution, which inhibits lateral etching of the pores and maintains pore directionality. In the p-type Si, the bandgap of PSi increases by quantum confinement effects [3]".

"The resulting characteristics of the PSi layer, including the average pore width, porosity, pore orientation, and layer thickness, depend upon the fabrication conditions used, including the substrate doping and type, the hydrofluoric acid concentration, the anodization current density and anodization time [1, 4, and 8]. PSi can have pore sizes ranging from a few nanometers to several microns, as primarily dictated by the silicon substrate doping and space charge region that forms during the etching process [9]. In this work, PSi of ~ (3-20) nm-radius pore size is used [15, 16, 17, and 18]. For a specific hydrofluoric acid concentration, the porosity, which determines the refractive index of the PSi layer, is proportional to the current density [10].

Varying the current density is a convenient way to form PSi layers with different refractive indices. Consecutive PSi layers can also be fabricated [11, 12]. Changing the current density does not affect the layer previously formed because silicon dissolution occurs preferentially at the silicon-electrolyte interface. Additionally, the thickness of each layer can be precisely controlled by the etching time for a given applied current density."

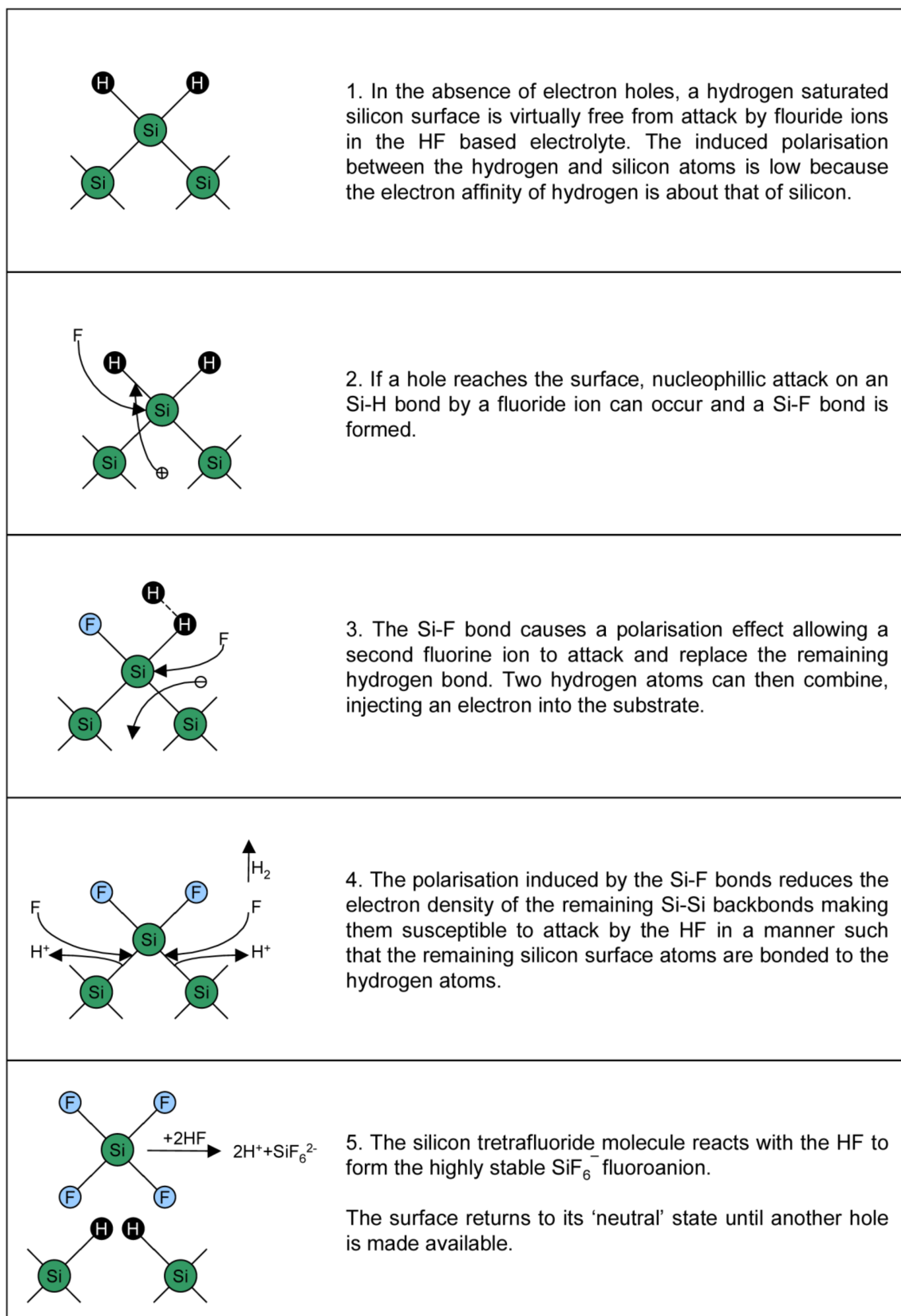

Figure A.1: Mechanism of PSi formation on p-type silicon. **Reproduced from [13]**

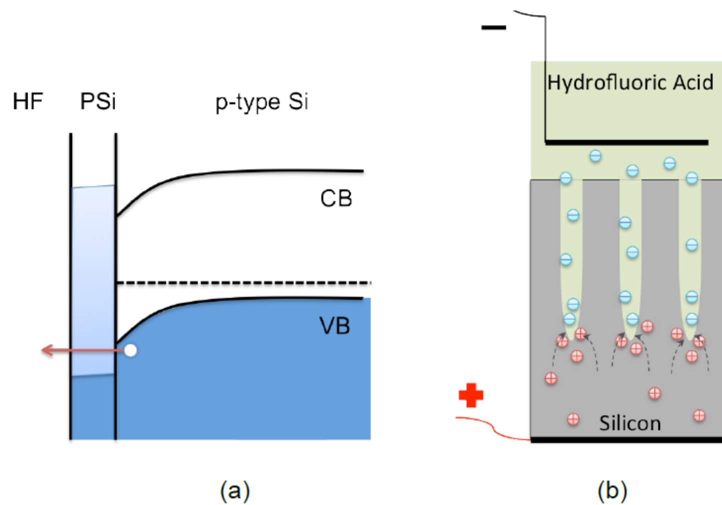

Figure A.2: (a) Band diagram of the p-Si/PSi/HF solution interface under current flow. (b) Schematic of the PSi etching cell. **Reproduced from [7]**

PSi waveguide fabrication

PSi has the advantage of a large internal surface area(>100m²/cm³), which makes it an attractive host material in biosensing applications and leads to improved capabilities for detecting small molecules[18]. As Xing Weir et al. [18] observed, "Based on the electrochemical etching method introduced before a PSi waveguide structure is fabricated (**Figure A.3**) using the etching cell shown in **Fig.A.2 (b)** [19]. The PSi waveguide is fabricated by electrochemical etching of p+ (0.01Ω-cm) silicon wafers in a 15% ethanoic hydrofluoric acid electrolyte, which is composed of 175 mL 99% ethanol and 75 mL 49% aqueous HF. The waveguide consists of two thin PSi films: a top, low porosity (high refractive index) layer etched at 5 mA/cm^2 for 62 seconds and a bottom, high porosity (low refractive index) layer etched at 48 mA/cm^2 for 53 seconds. After anodization, the waveguides are soaked in 1.5 mM KOH for 30 minutes to widen the pores. The nominal thicknesses of the PSi waveguide layers, as measured

by scanning electron microscope (SEM), are as follows: 325 ± 20 nm top PSi layer and 1500 ± 20 nm bottom layer".

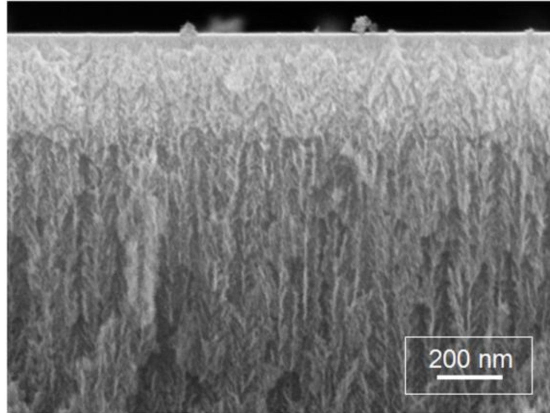

Figure A.3: Cross-section SEM image of two-layer porous silicon waveguides. The brighter regions are the nanoscale silicon matrix and the dark regions are void spaces.**Reproduced from [18]**

Oxidation

"In order to let biomolecules interact greatly with the strongly confined field in the PSi waveguide region, biomolecules must be immobilized within the pores. Several methods for immobilizing different kinds of biomolecules onto a silicon dioxide surface are available [20, 21]. Therefore, PSi waveguides need to be firstly oxidized in order to utilize these techniques. There is an optimal thickness of oxide to grow on the pore walls. Insufficient oxide will lead to incomplete attachment of biomolecules. Over-oxidation will compromise the refractive index contrast of the waveguide, which subsequently reduces the electric field confinement in the waveguide film layer and reduces the sensitivity of detecting biomolecules in that layer. Oxidation can dramatically reduce refractive index of a PSi layer (nSi = 3.4784 at 1550nm, $nSiO_2$ = 1.45 at 1550nm) [22]. Hence, the minimum amount of oxidation that allows bimolecular attachment needs to be determined in order to achieve the best sensing performance".

"There are two major elements that can affect the oxidation rate: temperature and time. For bulk silicon, it is typical to heat the sample at 800ºC for tens to hundreds of minutes to create a 10-20 nm thin gate oxides for submicron devices [23]. For PSi waveguide sensors, it is not necessary to grow a thick insulating oxide layer. Only a thin SiO_2 film is needed for bimolecular attachment. Due to its distinct structure and morphology, PSi oxidizes at different rates compared to bulk silicon. Therefore, a series of oxidation testing experiments were conducted for PSi under different temperature and time conditions. For simplicity, single-layer PSi samples were used to test the oxidation conditions".

"Single-layer PSi samples are fabricated by electrochemical etching of boron doped p+ silicon with a 0.01 Ω.cm resistivity. The electrolyte is 15% hydrofluoric (HF) acid. The PSi layer is formed by applying 48 mA/cm^2 for 100 seconds. Then 100 μL of 1.5 mM KOH solution is dropped on the PSi to open the pores. After incubating for 30 min in KOH, washing the sample with ethanol, and drying with nitrogen, the sample is ready for oxidation. The thickness of the PSi layer is approximately 3 μm, and the porosity is about 88%".

References

[1] P. C. Searson and J. M. Macaulay, "The fabrication of porous silicon structures," Nanotechnology 3, 188-191 (1992).

[2] K. H. Jung, S. Shih, and D. L. Kwong, "Developments in Luminescent Porous Si," J. Electrochem. Soc. 140, 3046-3064 (1993).

[3] V. Lehmann and U. Gosele, "Porous Silicon Formation - a Quantum Wire Effect," Appl. Phys. Lett. 58, 856-858 (1991).

[4] R. L. Smith and S. D. Collins, "Porous Silicon Formation Mechanisms," J.Appl. Phys. 71, R1-R22 (1992).

[5] X. G. Zhang, "Morphology and formation mechanisms of porous silicon," J.Electrochem. Soc. 151, C69-C80 (2004).

[6] H. Gerischer, "The Impact of Semiconductors on the Concepts of Electrochemistry," Electrochim. Acta 35, 1677-1699 (1990).

[7] P. Allongue, in *Properties of Porous Silicon*, L. T. Canham, ed. (IEE INSPEC, London, UK, 1997).

[8] R. Herino, G. Bomchil, K. Barla, and C. Bertrand, "Porosity and pore size distribution of porous silicon layers," J. Electrochem. Soc. 134, 1994-2000 (1987).

[9] V. Lehmann and John Wiley & Sons., "The electrochemistry of silicon instrumentation, science, materials and applications," (Wiley-VCH, Weinheim, 2002).

[10] J. E. Lugo, H. A. Lopez, S. Chan, and P. M. Fauchet, "Porous silicon multilayer structures: A photonic band gap analysis," J. Appl. Phys. 91, 4966-4972 (2002).

[11] M. G. Berger, C. Dieker, M. Thonissen, L. Vescan, H. Luth, H. Munder, W.Theiss, M. Wernke, and P. Grosse, "Porosity Superlattices - a New Class of Si Heterostructures," J. Phys. D: Appl. Phys. 27, 1333-1336 (1994).

[12] M. G. Berger, M. Thonissen, R. Arensfischer, H. Munder, H. Luth, M.Arntzen, and W. Theiss, Investigation and Design of Optical-Properties of Porosity Superlattices," Thin Solid Films 255, 313-316 (1995).

[13] H. F. Arrand, "Optical waveguides and components based on porous silicon," PhD thesis (University of Nottingham, 1997).

[14] A. W. Snyder and J. D. Love, *Optical waveguide theory* (Chapman and Hall, London; New York, 1983).

[15] A. Jain , S. Rogojevic, S. Ponoth , N. Agarwal , I. Matthew , W.N. Gill , P. Persans , M.Tomozawa , J.L. Plawsky , E. Simonyi ,"Porous silica materials as low-k dielectrics for electronic and optical interconnects", Elsevier Science, Thin Solid Films 398 – 399 (2001) 513–522

[16] I. Hoseinzadeh, R. S. Dariani . "Measurement of optical loss in oxidized multilayer planar porous silicon waveguides ", Optoelectronics and advanced materials-rapid communications vol.1, No. 9, September 2007, p. 471 - 476, Department of Physics, Alzahra University, Tehran, 19938, Iran

[17] E. J. Teo, A. A. Bettiol, P. Yang,2 M. B. H. Breese, B. Q. Xiong, G. Z. Mashanovich, W. R. Headley, and G. T. Reed, "Fabrication of low-loss silicon-on-oxidized-poroussilicon strip waveguide using focused proton-beam irradiation", / Vol. 34, No. 5 / OPTICS LETTERS, March 1, 2009

[18] Xing Wei, "Porous Silicon Waveguide Biosensor With a Grating Coupler",Ph.D dissertation. Dept.Electrical Engineering, Graduate School of Vanderbilt University, Nashville, Tennessee. May, 2012

[19] X. Wei, C. Kang, G. Rong, S. T. Retterer, and S. M. Weiss, "Porous silicon waveguide with integrated grating coupler for DNA sensing," Proc. SPIE 7167, 71670C (2009).

[20] T. Strother, W. Cai, X. S. Zhao, R. J. Hamers, and L. M. Smith, "Synthesis and characterization of DNA-modified silicon (111) surfaces," J. Am. Chem. Soc. 122, 1205-1209 (2000).

[21] M. C. Pirrung, "How to make a DNA chip," Angewandte Chemie-International Edition 41, 1277 (2002).

[22] E. D. Palik, Handbook of optical constants of solids, Academic Press handbook series (Academic Press, Orlando, 1985).

[23] N. M. Ravindra, J. Narayan, D. Fathy, J. K. Srivastava, and E. A. Irene, "Silicon oxidation and Si–SiO2 interface of thin oxides," J. Mater. Res. 2, 216-221 (1987).

Appendix B: Matlab modesolver code used to solve for the waveguide leaky modes, absorption loss, surface scattering loss, and volume scattering loss

To use this code the reader needs to follow the comments that I have added next to every line. There are parameters must be entered by the user such as the waveguide dimensions and indices, the wavelength, the pore size, the porosity, and the r.m.s roughness (sigma). Furthermore, it is very important to use very accurate guess, so the first step I used to do was to run the basic full vector code to find n_{eff} and use that as a guess for the main code.

I tried to add the instructions used to find n_{eff} to the main code used for solving the waveguide's leaky modes but I failed, because there was an overlap between the waveguide mesh functions with different parameters which are used in both codes and they are both required for the main operations so we can't delete any of them.

1- The basic full vector code.

```
% This example shows how to calculate and plot both the
% fundamental TE and TM Eigen modes of an example 3-layer ridge
% waveguide using the full-vector Eigen mode solver.

% Refractive indices:
% there are two cases for lower cladding

mynum1=input ('Enter a number:');
switch mynum1
    case 1 % this case is when lower cladding is normal dielectric

n1 = 1.26;          % Lower cladding
case 2    % this case is used when the lower cladding is porous material

nh=1.45;         %refractive index of host material ,it is Silica in our
case, but in case of normal dielectrics waveguide this is the refractive
index of lower cladding assuming npore=1

npore=1;         % the refractive index of embedded material(pore) which is
air in this case

porosity=0.3;    % the porosity can be changed depending on the design
,porosity=0 in normal dielectrics waveguide

n1=((1-porosity)*nh^(2/3)+npore^(2/3)*porosity)^1.5; % Yusra's thesis using
Looyenga's model for porous material's effective index
```

```
fprintf(1,'effective index of porous = %7.5f \n',n1);
end


n2 = 1.45;          % Core
n3 = 1;          % Upper cladding (air)

% Layer heights:
h1 =3;           % Lower cladding
h2 = 1;           % Core thickness
h3 = 5;           % Uper cladding

% Horizontal dimensions:
rh = 0.5;          % Ridge height
rw =2;           % Ridge half-width
side = 1.5;          % Space on side

% Grid size:
dx = 0.0125;        % grid size (horizontal)
dy = 0.0125;        % grid size (vertical)

lambda =0.546;      % vacuum wavelength
nmodes = 1;         % number of modes to compute

[x,y,xc,yc,nx,ny,eps,edges] = waveguidemesh([n1,n2,n3],[h1,h2,h3], ...
                                            rh,rw,side,dx,dy);

% First consider the fundamental TE mode:

[Hx,Hy,neff] = wgmodes(lambda,n2,nmodes,dx,dy,eps,'000A');

fprintf(1,'neff = %.6f\n',neff);

figure(1);
subplot(121);
contourmode(x,y,Hx);
title('Hx (TE mode)'); xlabel('x'); ylabel('y');
for v = edges, line(v{:}); end

subplot(122);
contourmode(x,y,Hy);
title('Hy (TE mode)'); xlabel('x'); ylabel('y');
for v = edges, line(v{:}); end

% Next consider the fundamental TM mode
% (same calculation, but with opposite symmetry)

[Hx,Hy,neff] = wgmodes(lambda,n2,nmodes,dx,dy,eps,'000S');
fprintf(1,'neff = %.6f\n',neff);

figure(2);
subplot(121);
contourmode(x,y,Hx);
title('Hx (TM mode)'); xlabel('x'); ylabel('y');
```

```
for v = edges, line(v{:}); end

subplot(122);
contourmode(x,y,Hy);
title('Hy (TM mode)'); xlabel('x'); ylabel('y');
for v = edges, line(v{:}); end
```

2- The main code used for solving the waveguide's leaky modes

```
% This code illustrates how to use perfectly matched layers
% at the edges of the computation window. The waveguide
% considered here is the same as in 'basic_semivector.m', with
% the exception that we have added a substrate layer that has
% the same refractive index of the core.  The modesolver
% computes a complex propagation constant that includes the
% propagation loss associated with radiation into the
% substrate.
%the code has good models to calculate volume scattering loss in porous
%silica waveguide, and surface scattering loss for both normal dielectrics
%and low-k dielectrics waveguide .
% Note that the perfectly-matched layer is constructed using
% the stretchmesh routine, with a complex stretching factor
% (i.e., complex coordinate stretching.)
% Refractive indices:




close all
clear all



ns = 3.84+.013*i ;    % substrate is silicon , this value should be changed
when we change the substrate3.84+.013*i
n2 = 1.45;            % Core
n3 = 1;          % Upper cladding
n1=1.45;         %refractive index of host material ,it is Silica in our
case, but in case of normal dielectrics waveguide this is the refractive
index of lower cladding assuming npore=1

npore=1;         % the refractive index of embedded material(pore) which is
air in this case

porosity=0.3;    % the porosity can be changed depending on the design
,porosity=0 in normal dielectrics waveguide

nporouseff=((1-porosity)*n1^(2/3)+npore^(2/3)*porosity)^1.5; % Yusra's thesis
using Looyenga's model for porous material's effective index


% Vertical dimensions:
hs = 4;            % Substrate in microns
h1 = 3;       % Lower cladding in microns2
```

```
h2 = 1;         % Core thickness in microns
h3 = 5;            % Upper cladding in microns1
rh = 0.5;          % Ridge height in microns0.015

% Horizonta3l dimensions:
rw=4;                %ridge width
rw = rw/2;            % Ridge half-width
side = 5;          % Space on side

% Grid size:
dx = 0.04;         % grid size (horizontal)dx = 0.04;
dy = 0.015;         % grid size (vertical)dy = 0.015;
delta_y=dy;
lambda =0.633;       % vacuum wavelength
nmodes = 1;          % number of modes to compute


k0=2*3.14/lambda;

d=0.0175;% diamater of the pore in porous material
drange=0:0.005:0.05; % I used this range to plot the volume scattering as a
function of the pore diameter

%sigu is the r.m.s. roughness (sigma) for the upper waveguide interface
%sigl is the r.m.s. roughness (sigma) for the lower waveguide interface

sigu=0.001:0.005:0.02;% I used this range just to get plot of scattering as
function of segu, we can change the range depenfing on the design

sigl=0.024;% I used this value separatly to get plot of scattering as a
function of lambda; we can change it depending on our design

fprintf (1,'generating index mesh...\n');


%  This function creates an index mesh for the finite-difference
% mode solver.  The function will accommodate a generalized three
% layer rib waveguide structure.  (Note: channel waveguides can
% also be treated by selecting the parameters appropriately.)


                                        %INPUT

% n - indices of refraction for layers in waveguide
% h - height of each layer in waveguide
% rh - height of waveguide feature
% rw - half-width of waveguide
% side - excess space to the right of waveguide
% dx - horizontal grid spacing
% dy - vertical grid spacing
%
% OUTPUT
%
% x,y - vectors specifying mesh coordinates
```

```
% xc,yc - vectors specifying grid-center coordinates
% nx,ny - size of index mesh
% eps - index mesh (n^2)
% edges - (optional) list of edge coordinates, to be used later
%   with the line() command to plot the waveguide edges
```

```
[x,y,xc,yc,nx,ny,eps,edges] =
waveguidemesh([ns,nporouseff,n2,n3],[hs,h1,h2,h3], ...
                                            rh,rw,side,dx,dy);
```

```
% Complex coordinate stretching:
%
% This function can be used to continuously stretch the grid
% spacing at the edges of the computation window for
% finite-difference calculations.  This is useful when you would
% like to increase the size of the computation window without
% increasing the total number of points in the computational
% domain.  The program implements four different expansion
% methods: uniform, linear, parabolic (the default) and
% geometric.  The first three methods also allow for complex
% coordinate stretching, which is useful for creating
% perfectly-matched non-reflective boundaries.

% INPUT:
%
% x,y - vectors that specify the vertices of the original
%   grid, which are usually linearly spaced.
% nlayers - vector that specifies how many layers of the grid
%   you would like to expand:
%   nlayers(1) = # of layers on the north boundary to stretch
%   nlayers(2) = # of layers on the south boundary to stretch
%   nlayers(3) = # of layers on the east boundary to stretch
%   nlayers(4) = # of layers on the west boundary to stretch
% factor - cumulative factor by which the layers are to be
%   expanded.  As with nlayers, this can be a 4-vector.

% OUTPUT:
%
% x,y - the vertices of the new stretched grid
% xc,yc (optional) - the center cell coordinates of the
%   stretched grid
% dx,dy (optional) - the grid spacing (dx = diff(x))
%
```

```
[x,y,xc,yc,dx,dy] = stretchmesh(x,y,[0,160,20,0],1+j*2);
```

```
% This function computes the two transverse magnetic field
% components of a dielectric waveguide, using the finite
% difference method.

% INPUT:
%
% lambda - optical wavelength
% guess - scalar shift to apply when calculating the eigenvalues.
%     this routine will return the eigenpairs which have an
%     effective index closest to this guess
% nmodes - the number of modes to calculate
% dx - horizontal grid spacing (vector or scalar)
% dy - vertical grid spacing (vector or scalar)
% eps - index mesh (isotropic materials)

% boundary - 4 letter string specifying boundary conditions to be
% applied at the edges of the computation window.
%   boundary(1) = North boundary condition
%   boundary(2) = South boundary condition
%   boundary(3) = East boundary condition
%   boundary(4) = West boundary condition

% OUTPUT:
%
% hx - three-dimensional vector containing Hx for each
%      calculated mode
% hy - three-dimensional vector containing Hy for each
%      calculated mode (e.g.: hy(:,k) = two dimensional Hy
%      matrix for the k-th mode
% neff - vector of modal effective indices

% NOTE:  when analyzing leaky modes, it is important that you
% provide a good guess, usually by solving the mode of an
% equivalent non-leaky structure first. use the basic full vector code to
% find accurate guess

guess= 1.430802;

[Hx,Hy,neff] = wgmodes(lambda,guess,nmodes,dx,dy,eps,'000A');

fprintf(1,'Real[nte] = %.6f\n',real(neff));
fprintf(1,'Imag[nte] = %.6e\n',imag(neff));
alpha = 4*pi*imag(neff)/lambda; % um^-1
absorption = 4.34*alpha*10000; %dB/cm @ lambda um

beta=k0*sqrt(real(neff)^2+imag(neff)^2);

%kyu:y-directed decay constant in the upper cladding
%kyl:y-directed decay constant in the lower cladding
%h2:core thickness in micron

kyu=sqrt(beta^2-k0^2*n3^2);
kyl=sqrt(beta^2-k0^2*nporouseff^2);
kyuinv=1/kyu;
kylinv=1/kyl;
```

```
decayfact=1/(h2+kyuinv+kylinv);

%segmafact=(4*3.14*n2*sqrt(segu^2+segl^2)/lambda)^2 but we assumed segu=segl;

sigmafact=(4*3.14*n2.*sqrt(2.*sigu.^2)./lambda).^2;% this one is to plot


surface scattering as a function of sigma

sigmafact1=(4*3.14*n2*sqrt(2*sigl^2)/lambda)^2;% this one is to find surface


scattering @ fixed lambda and fixed sigma
%sth is sin(propagaion angle)

sth=neff/n2;

surfacescatteringloss=0.5*4.3*10000.*sigmafact*decayfact*(1-sth^2)^1.5/sth;%

this one is to plot surface scattering as a function of sigma

surfacescatteringloss1=0.5*4.3*10000*sigmafact1*decayfact*(1-sth^2)^1.5/sth;%

this one will give surface scattering at sigl and lambda


mynum1=input('Enter a number:');
switch mynum1
    case -7 % volume scattering loss for normal dielectrics waveguide=0
        volumescatteringloss1=0;

    case -6 % volume scattering loss for porous silica waveguide


volumescatteringloss1=porosity*172*1000*3.14^4*((nporouseff^2-
1)/(nporouseff^2+2))^2*d^3/lambda^4;% volume scattering at lambda and d

end


fprintf(1,'surfac scattering loss @lambda nm = %7.5f
dB/cm\n',surfacescatteringloss);
fprintf(1,'surfac scattering loss @lambda nm and sigml = %7.5f
dB/cm\n',surfacescatteringloss1);
fprintf(1,'effective index of porous = %7.5f \n',nporouseff);
fprintf(1,'Absorption loss = %7.5f dB/cm\n',absorption);
fprintf(1,'volumescattering loss @lambda nm = %7.5f
dB/cm\n',volumescatteringloss1);


Hx = Hx/max(Hy(:));
Hy = Hy/max(Hy(:));
```

```
figure(1);

I=Hy.*conj(Hy);
K=flipud(I);
I=[K;I];
I=I';
I=flipud(I);
I=I/sum(sum(I));
imagesc(I)

I=I*10000;
p=-7:dx:7.04;
q=[fliplr(y)];
figure(2)
contourmode(p,q,(I'));
title('Optical Field Intensity'); xlabel('x'); ylabel('y');
for v = edges, line(v{:}); end
y1=(hs+h1+h2)/delta_y;
y2=(hs+h1+h2+h3)/delta_y;
uc_field_pct=sum(sum(I(1:(y2-y1),:)))./sum(sum(I))*100;

% the following is to find the cladding confinement
V=2*3.14*h2*sqrt(n2^2-nporouseff^2)/lambda;  %normalized thickness
gamafact=k0*sqrt(neff^2-nporouseff^2);
conf=(1+(2*gamafact*h2/V^2))/(1+(2/(gamafact*h2)));% the confinement factor
at lambda in um
claddconf=(1-conf)*(nporouseff/(nporouseff+n3));%the cladding confinement
factor @ lambda in um

fprintf(1,'conf = %7.5f \n',conf);
fprintf(1,'cladding conf = %7.5f \n',claddconf);

totalscattering=surfacescatteringloss1+volumescatteringloss1;

fprintf(1,'total scattering loss  @ lambda = %7.5f dB/cm\n',totalscattering);

modallosslowercladd=volumescatteringloss1*claddconf+surfacescatteringloss1+ab
sorption; %the cladding modal loss  @ lambda in um

fprintf(1,'modal loss  @ lambda =  and sigl and d value %7.5f
dB/cm\n',modallosslowercladd);

% plot surface scattering as a function of sigma @ lambda

figure(3);
plot(sigu,surfacescatteringloss);

% plot of total surface scattering as a function of lambda assuming
sigl=constant
figure(4);
lambda1=0.5:0.2:1.9;% we defined new lambda just for getting different plots
in the same run
k1=2*3.14./lambda1;
```

```
beta1=k1.*sqrt(real(neff)^2+imag(neff)^2);
kyu=sqrt(beta1.^2-k1.^2.*n3^2);
kyl=sqrt(beta1.^2-k1.^2.*nporouseff^2);
kyuinv=1./kyu;
kylinv=1./kyl;
decayfact=1./(h2+kyuinv+kylinv);
%sigmafact=(4*3.14*n2*sqrt(segu^2+segl^2)/lambda)^2;
sigmafact2=(4*3.14*n2.*sqrt(2*sigl^2)./lambda1).^2;
sth=neff/n2;
surfacescatteringloss2=0.5*4.3*10000.*sigmafact2.*decayfact.*(1-
sth^2)^1.5/sth;
fprintf(1,'surface scattering = %7.5f dB/cm\n',surfacescatteringloss2);
plot(lambda1,surfacescatteringloss2);

% having two models for volume scattering one in case of spherical pores and
% the other in case of cylinrical pores, case 1 plot of volume scattering
% for spherical pores as function of lambda , case 2 plot of volume
scattering
% for cylindrical pores as function of lambda



mynum=input('Enter a number:');
switch mynum
    case -3 % volume scattering loss for normal dielectrics waveguide=0
        volumescatteringloss=0;

    case -2 % volume scattering loss for porous silica waveguide

figure(5)
number1 = input('Enter a number:');
switch number1

    case 1

volumescatteringloss=porosity*172*1000*3.14^4*((nporouseff^2-
1)/(nporouseff^2+2))^2*d^3./lambda1.^4;
fprintf(1,'volume scattering = %7.5f dB/cm\n',volumescatteringloss);
plot(lambda1,volumescatteringloss);
    case 2
        porehight=0.1;


volumescatteringloss=porosity*2.866*10000*3.14^4*d^4./(lambda1.^4*porehight);
        plot(lambda1,volumescatteringloss);

end
end

% plot the total loss as function of wavlength

figure(6)
alpha2 = 4*pi*imag(neff)./lambda1;  % um^-1
absorption2 = 4.34*alpha2*10000; %dB/cm
totalscatteringloss2=surfacescatteringloss2+volumescatteringloss;
```

```
fprintf(1,'total loss = %7.5f dB/cm\n',totalscatteringloss2);
plot(lambda1,totalscatteringloss2,'color','g');
hold on;
plot(lambda1,volumescatteringloss,'color','b');
hold on;

plot(lambda1,surfacescatteringloss2,'color','r');
hold on
plot(lambda1,absorption2,'color','y');


%the plot of modal loss in cladding as  a function of  wavelength
figure(7)
V2=2*3.14*h2*sqrt(n2^2-nporouseff^2)./lambda1;  %normalized thickness
conf2=(1+(2*gamafact*h2./V2.^2))/(1+(2/(gamafact*h2)));% i defined this V2 to
find the values a s a function of wavelength
claddconf2=(1-conf2).*(nporouseff/(nporouseff+n3));
fprintf(1,'cladding conf = %7.5f \n',claddconf2);
modallossincladding=claddconf2.*volumescatteringloss+surfacescatteringloss2+a
bsorption2;
fprintf(1,'modal loss in cladding = %7.5f dB/cm\n',modallossincladding);
plot(lambda1,modallossincladding);




%case 1 plot of volume scattering  for spherical pores as function of pore
size , case 2 plot of volume scattering
% for cylindrical pores as function of pore size

number2 = input('Enter a number:');
switch number2

    case -5
        volumescatteringloss2=0;  % voulme scattering loss in normal
dielectric waveguide
    case-4



figure(8)
number = input('Enter a number:');
switch number
     case -1
volumescatteringloss2=porosity*17.2*10000*3.14^4*((nporouseff^2-
1)/(nporouseff^2+2))^2.*drange.^3./lambda^4;
fprintf(1,'volume scattering = %7.5f dB/cm\n',volumescatteringloss2);
plot(drange,volumescatteringloss2);
    case 0
        poreheight=0.1;


volumescatteringloss2=porosity*2.866*10000*3.14^4.*drange.^4./(lambda^4*poreh
eight);
        plot (drange,volumescatteringloss2);
```

```
end
end
```

3- The Matlab code that I used to study the effect of scattering on sensitivity and optimal lower cladding thickness.

In the following code, I just simulated for every lower cladding thickness and modal scattering loss. Then, I recorded the data for different sensitivities and different values of lower cladding thickness and scattering, and I made them in groups to make specific plot for each value of scattering.

```
close all
clear all

 % x represents lower cladding thickness

x=[6000
5000
4000
3000
2500
2000
1900
1800
1700
1600
1500];

S represents sensitivity modulation/RIU

S=[70.63551402
51.2625538
47.84172662
34.08071749
26.82060391
20.42940794
18.47368421
17.25738397
15.92592593
14.71919084
13.62403505];

S4=[0.207901817
1.391015409
5.493921869
14.53154876
17.49710313
```

```
17.09308655
15.95454545
14.31835206
13.4648318
12.63076165
11.82151973
];

S2=[0.917186109
3.991773394
13.40339764
23.52941176
22.77526395
19.18142944
17.55
16.55870445
15.40716612
14.33756806
13.34559575];

S5=[0.185004091
0.842258911
3.455058265
10.51175657
14.20507996
15.41482572
14.625
14.25087108
13.63112392
12.9903688
12.33704893];

S15=[0.092600917
0.4404441
1.592245794
6.01422731
8.160908509
10.37682302
10.10344828
10.13649852
9.91435768
9.62497372
9.2722251];
S05=[8.37398374
25.16205068
38.06214227
32.61802575
26.35253054
20.29734971
18.37696335
17.18487395
15.87248322
14.6801168
12.59566937];

loss1=[3.0107
```

```
3.0697
3.3892
5.23
8.63
18.37
22
26.7
32.7
40.57
50.93
];

here I multiplied S by 100 to make it as (%modulation/RIU)

S2=S2*100;
S=S*100;
S4=S4*100;
S5=S5*100;
S15=S15*100;
S05=S05*100;
%m1 and loss1 are for 3 dbscat loss
figure(1)
[AX,H1,H2] = plotyy(x,S2,x,loss1,'plot');

set(get(AX(1),'Ylabel'),'String','Sensitivity (%/RIU)')
set(get(AX(2),'Ylabel'),'String','Photodetector Coupling (dB/cm)')

xlabel('Lower Cladding Thickness (nm)')
title('LC Thickness vs. Sensitivity and Coupling (3 dB/cm scatter)')
set(H1,'LineStyle','s')
set(H2,'LineStyle','d')
legend('Sensitivity','Coupling Loss');


set(gca,'YTick',[0 400 800 1200 1600 2000])
set(AX(2),'YTick',[0 10 20 30 40 50 60])

figure(4)
plot(x,S,'*',x,S05,'d',x,S2,'s',x,S4,'^',x,S5,'x',x,S15,'o')
xlabel('Lower Cladding Thickness (nm)')
ylabel('Sensitivity (%/RIU)');
title('Effect of Absorbed Scattered Power on Optimal LC Thickness');
legend('0 dB/cm','0.5 dB/cm','2 dB/cm','4 dB/cm','5 dB/cm','15 dB/cm');
```

End